eXPRESS Polymer Letters Vol.5, No.3 (2011) 208
Available online at www.expresspolymlett.com
DOI: 10.3144/expresspolymlett.2011.19

'Reinforced' knowledge: 14th European Conference on Composite Materials

*T. Czigány**

Department of Polymer Engineering, Faculty of Mechanical Engineering, Budapest University of Technology and Economics, Műegyetem rkp. 3., H-1111 Budapest, Hungary

This issue of ***eXPRESS Polymer Letters*** contains selected papers presented at the 14th European Conference on Composite Materials (ECCM) held in Budapest, 7–10 June 2010. This conference is a regular forum for scientist, specialists and industrial experts dedicated to polymers/metals/ceramic materials, to their technology, design, simulation, testing and application aspects. This conference series was founded after realizing the interest of scientist and technologists, not only from Europe but from all over the World, in getting general and specific knowledge about the most recent advancements of the cutting edge composite materials topics. The first conference was organized in France (Bordeaux) in 1985 and the next 15th conference will be held in Venice, Italy between 24–28 June, 2012 Besides looking forward, the 25th anniversary of the conference provided an opportunity for retrospection. This review was given by the first day's plenary lecture speaker, Prof. G.S. Springer (USA), doyen of composite science and technology. Material science and technology has gone through vast development in the last decades. Modern composites are essential in all fields of life, including building and transportation industry, information technology, energy sector and medical applications. In this context, the current and future composite materials, technologies and application fields were presented during the second days' plenary lectures: Prof. I. Verpoest (B) gave a talk on nano and biocomposites, Prof. O.T. Thomsen's (DK) lecture addressed wind turbine composite rotor blades, while Dr. C. Weimer's (D) presentation focused on future processing techniques for cost-effective high performance composites in helicopter manufacturing. During the conference 395 oral lectures and 195 posters were presented by experts from 60 countries in 6 parallel sessions. The conference provided a platform for presentation and discussion of the latest results and offered an opportunity for young scientists to learn and to present their work. The conference brought together the researchers from academia and industry, served as an open forum for the exchange of knowledge, and helped to establish worldwide scientific cooperation between 700 participants.

From left to right:
Prof. M.Q. Zhang, Prof. G.C. Psarras, Prof. T. Czigány, Prof. P.M. Frontini, Prof. J. Karger-Kocsis, Prof. G. Marosi, Prof. A. Pegoretti, Prof. A. Bismarck, Prof. R.A. Shanks

This issue presents a selection of the most recent results of the above-mentioned research areas within the field of reinforced polymeric materials. This venue gave a possibility to the International Advisory Board of ***eXPRESS Polymer Letters*** to meet each other (see Figure) and discuss future works for the journal.

*Corresponding author, e-mail: czigany@eik.bme.hu

eXPRESS Polymer Letters Vol.5, No.3 (2011) 209–217
Available online at www.expresspolymlett.com
DOI: 10.3144/expresspolymlett.2011.20

Potential emissions savings of lightweight composite aircraft components evaluated through life cycle assessment

L. Scelsi[1], *M. Bonner*[1], *A. Hodzic*[1*], *C. Soutis*[1], *C. Wilson*[1], *R. Scaife*[2], *K. Ridgway*[2]

[1]Aerospace Engineering, Department of Mechanical Engineering, The University of Sheffield, S1 3JD, UK
[2]Advanced Manufacturing Research Centre with Boeing, The University of Sheffield, S60 5TZ, UK

Received 22 July 2010; accepted in revised form 26 October 2010

Abstract. A cradle-to-grave life cycle assessment (LCA) of structural aircraft materials has been utilised to assess and compare the total emissions produced during manufacturing, use and disposal of aerospace materials and their selected components. First, a comparison of aluminium, GLARE and carbon fibre reinforced polymer (CFRP) plates was performed to investigate the potential of lightweight composites in reducing aviation emissions. Subsequently, a case study is presented on a tubular component for which more accurate manufacturing data were directly available. A structural steel tube was replaced with a composite tubular component. The analysis has shown that once the composite material is used as a component in the aircraft, there is a cumulative saving of aircraft fuel and emissions, in particular from CFRP structures. The environmental analysis included the long-term use predictions for CFRPs, involving detailed raw materials production, use and operation, and disposal scenarios.

Keywords: *polymer composites, life cycle assessment, aviation emissions, carbon fibre reinforced polymers (CFRP)*

1. Introduction

Aviation emissions have come under scrutiny in recent years due to the rapid growth in air transport, which has been increasing at an annual rate of about 5% throughout the last two decades [1].

The effect of aviation emissions, which consist mainly of carbon dioxide (71%), water vapour (28%) and nitrogen oxides [2], on the atmosphere is the focus of intense research efforts [3, 4]. It is widely recognised that emission at high altitudes are more environmentally damaging than those at ground level, due to increased interaction with gases in the atmosphere. A parameter used to quantify the effect of aviation emission is the Radiative Forcing (RF) Index, which is a measure of the impact of an agent on the energy balance of the earth's atmosphere. A positive RF indicates a global warming effect. Aircraft operation involves the emission of (a) directly radiatively active substances (e.g. CO_2 or water vapor); (b) chemical species that produce or destroy radiatively active substances (e.g. NO_x, which modifies ozone concentration); and (c) substances that trigger the generation of aerosol particles or lead to changes in natural clouds (e.g. contrails). These emissions and cloud effects modify the chemical and particle microphysical properties of the upper atmosphere, resulting in changes in RF of the earth's climate system, which can potentially lead to climate change impacts and ultimately result in damage and welfare/ecosystem loss [5]. Thus, it is important to analyse the life cycle of aircraft systems and structures in as much detail as possible, in order to understand the long-term impact on the human environment and the earth's ecosystem. Some of these effects – such as the cirrus cloud enhancement due

*Corresponding author, e-mail: a.hodzic@sheffield.ac.uk

to contrails – are still poorly understood, and they are therefore not considered in current environmental models. However, their impact could be substantial and it is therefore necessary to constantly update LCA models, as new or more reliable information becomes available [6, 7].

In the civil aviation, implementation of composites and hybrid materials is driven largely by the high cost of aviation fuel and the introduction of legislation setting limits on the emission of greenhouse gases during operation [8]. According to European directive EC 101/2008, from 2012 the aviation sector will be included into the EU ETS emission trading scheme and aircraft operators with flights landing or departing from an EU airport will be required to buy allowances equal to the CO_2 emissions for each flight [9, 10]. It is widely recognised that the fuel consumption of an aircraft is strongly affected by its total weight and that the fuel used during aircraft operation can be significantly reduced by increasing the proportion of lightweight composites in its structure [11]. On the other hand, disposal of composite parts at their end-of-life is often more problematic than in the case of metals. Composites are not only more costly and energy intensive to produce than metals, but also notoriously difficult to recycle. Whilst the End of life Vehicles (ELVs) Directive 2000/53/EC places a significant burden on the automotive vehicle manufacturers, with recycling and recovery targets of respectively 85% and 95% by 2015, no such legislation applies to the civil aerospace industry. However, there is growing concern in the industry that a similar directive may be introduced [12].

It is therefore clear that the overall environmental benefits of replacing metals with composites are not directly evident, and a full cradle-to-grave life cycle assessment needs to be performed in order to rank different aerospace materials in terms of their environmental impact, as stated by the 'product stewardship principles for the aerospace sector' proposed by the Advisory Council for Aeronautics Research in Europe [12]. This paper aims to establish whether the increase in efficiency gained by using lightweight composite materials is significant enough to justify the additional emissions produced during the manufacturing and disposal stages compared with those of aluminium, and further to investigate after how many hours of flying time do composites and GLARE become the more environmentally friendly choice. In the aerospace industry, LCAs are being performed to assess various ways of reducing the environmental impact such as new materials, alternative fuels, improved aerodynamic design etc. In particular, the present debate is on the use of composite materials for primary airframe structures instead of the more conventional heavier aluminium. An initial study from Beck *et al.* [13] provided insights into the different levels of hazardous emissions arising from the manufacturing of Al, CFRP and GLARE hybrid laminates in aerospace industry. However, due to confidentiality reasons and to the difficulty in obtaining data from industry, such study was limited to examining flat plates of equal size made of different materials rather than actual aircraft components. Moreover, no other similar investigations are currently available in the literature.

The present work extend Beck's study by first examining flat plates of Al, GLARE and CFRP taking into account the typical weight savings of these materials, and subsequently presents a more detailed analysis on an actual component , whereby a structural steel tube was replaced with a tubular CFRP component. Although in the case of metals the specific energy [MJ/kg] needed to manufacture a component is fairly independent of its shape, size and shaping technology (typically, for aluminium the energy required for shaping the component is very low compared to the energy used to produce the material itself), in the case of composites the curing and shaping processes are simultaneous, and the specific energy requirement for the component is substantially influenced by processing conditions, such as curing temperature and time, type of autoclave used, degree of packing of the autoclave and so on. Those processing conditions can in turn be related to the geometry and dimension of the part, but also to many other factors, which are more specific to the manufacturing site. Therefore, in order to compare the LCA performance of composites and metals in aerospace, it was necessary to examine real size components.

Moreover, due to the complexity of aerospace component design and materials selection, a universal criterion for comparing composites and metal components is not available. As an example, even if the generally recognised design criterion for structural

parts in the aircraft wing is stiffness, uncertainties about composite materials behaviour (for instance related to anisotropy, damage tolerance and fatigue resistance) often lead design engineers to adopt more conservative safety factors than those used for metallic parts. It can therefore be concluded that the only accurate way to assess both the manufacturing energy and the weight savings of a composite component with respect to its metallic counterpart is to gather industrial data on both components designed to fulfil the same function.

Despite the very specific nature of the LCA analysis for components of such a complex design, examining a critical number of case studies, such as the one presented in this paper, can generate the critical amount of data necessary for understanding and quantifying the potential of the use of composites in emissions savings in the aviation industry.

2. LCA software and methodology

SimaPro 7.1 software was used in combination with Ecoinvent database to carry out LCA for aerospace materials (Pré Consultants, NL). The Ecoinvent data v2.0 contains international industrial life cycle inventory data on energy supply, resource extraction, material supply, chemicals, metals, agriculture, waste management services, and transport services. Eco-indicator 99 (E) V2.05 Europe EI 99 E/E was used as a chosen method [7, 14]. Such method allows aggregation of different impact categories into a single score value. This is an important aspect, because the success of LCA as a widespread industrial decision tool in the aerospace sector is strongly dependent on the simplicity in interpreting the results of the analysis. ISO 14042 standard (recently replaced by BS EN ISO 14040:2006 [14]) built in SimaPro software) prevents public disclosure of LCA results aggregated into single-score indicators when comparing environmental performance of commercial products. This is mainly due to the subjective nature of the weighting factors used in the calculations. Therefore the method presented in this study should not be used in a commercial context that requires subjective evaluation.

LCA contains inventory analysis and automatically calculates emissions from raw materials production. For the electricity supply, a typical UK energy mix was considered in the calculations (41% natural gas, 33% coal, 20% nuclear and smaller proportions from other energy sources). Neither environmental impacts associated with the manufacturing of tools, transport and buildings, nor environmental impacts of the labour force required to manufacture the parts are included in the analyses. These aspects have been excluded due to their minor contribution to the goal of the study.

3. LCA of panels used in aircrafts

An initial LCA was performed to compare the environmental impact of an aerospace panel when made respectively from aluminium alloy 2024, carbon fibre reinforced epoxy resin (CFRP), and GLARE (glass fibre/Al laminate used by Airbus in A380). These three structural materials have been chosen for comparison due to their relevance, especially aluminium alloy and CFRP. The impact of the manufacture and disposal stages of these materials were analysed with particular interest in the airborne emissions that affect climate change and also the quantity of fossil fuel usage. Further, the in-use phase was taken into account to assess which material is more environmentally friendly over the entire life cycle. A break-even plot was created to assess the amount of flying distance required for the CFRP and GLARE to become the environmentally preferential choice to Al-2024.

The base for comparison between the three materials was their estimated weight in currently designed aircraft structures. From the literature it was found that typical weight savings when using CFRP and GLARE are 20% and 10% respectively [15]. Therefore, since Al-2024 panel model weighted 10 kg, the CFRP and GLARE panels were assumed to be 8 and 9 kg respectively. This choice of criterion for comparison was found to be more relevant to the real-life compared to using panels' dimensions or volumes.

3.1. Manufacturing and disposal of the panels

Each panel was obtained from Al-2024 ingots by hot rolling in a four-high rolling mill and the final machining to the required size. The shaping of the Al-2024 ingot into a panel required about 5% of the energy needed to produce the ingot [16]. It was assumed that the Al-2024 is 100% recyclable and that the energy saved by recycling as opposed to producing another alloy from scratch is counted as positive emissions. A typical composition of CFRP

used in this work was 35% epoxy resin and 65% carbon fibre by weight [1]. The composite panel was manually laid-up and then cured in an autoclave with a power rating of 26.4 kW for 6 hours. A typical curing cycle for a 10 mm thick panel would involve heating at around 0.5°C/min for 2 hours, high temperature curing for 2 hours and cooling at 0.5°C/min for 2 hours. It was estimated that the power used by the heating system during the heating stage would not exceed 60% of the power rating during the heating stage and this proportion would reduce to 20% during the rest of the cure cycle. Considering the additional power consumption due to fan (1.5 kW), compressed air and electronics (1 kW), the total amount of electricity for the autoclaving process has been determined to be around 68 kWh.

GLARE (GLAss-REinforced" Fibre Metal Laminate) is a laminated material consisting of thin (0.13 mm) layers of aluminium sheet (typically more than 70% in volume) and unidirectional glass fibre layers embedded in an adhesive system. The layers are laid up and subsequently autoclaved. Due to its relatively limited use in the industry, interest in recycling of the Al layers in the hybrid system has been limited. Moreover, thermal recycling of GLARE might not be environmentally sound, being a very energy intensive process [17]. The Ecoinvent database contains data on the emissions related to the production of GLARE sheets. It was assumed that no substantial emission would arise from manufacturing of the flat panel of the required dimension starting from these sheets. The disposal scenario for both CFRP and GLARE is landfill, as there is no commercial recycling route available at this stage.

Figure 1 shows the global environmental impact using the single score index from Eco-indicator 99 (E). For improved clarity, only impact categories with significant contribution to the overall score are represented. LCA is by nature a comparative analysis, therefore standard Ecoindicator values can be regarded as dimensionless figures. The scale is chosen in such a way that 1 Pt is representative for one thousandth of the yearly environmental load of an average European inhabitant [14].

It can be seen from this graph that the Al-2024 panel is by far the most environmentally friendly choice during the manufacturing stages, the main

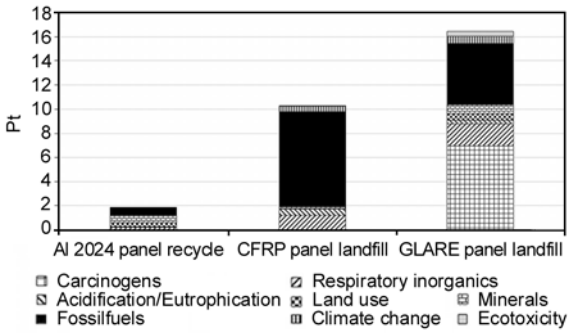

Figure 1. Single score impact results for manufacturing and disposal of Al 2024, CFRP and GLARE panels. Al 2024 is assumed to be recycled at the end of life. CFRP and GLARE are landfilled.

reason being that aluminium is 100% recyclable. Recycling aluminium requires much less energy than extracting it from its ore and this energy saving is counted as positive emissions. In practice, current material standards for aerospace components do not allow re-using recycled aluminium into new aircraft parts. However, for the purpose of this analysis it was assumed that the recycled aluminum presents almost equal properties to the virgin one and could be reused for high value applications, such as components for trucks, tractors, trailers, railroad cars and buses. The GLARE panel produced the highest environmental impact during this stage of the life cycle with the CFRP producing lower emissions in comparison.

3.2. In-use

The objective of this part of the study was to estimate the potential savings of composites over the entire life cycle of the component.

According to the widely-used 'Base of Aircraft Data' (BADA) models [18], fuel consumption for aircraft depends crucially on thrust (Equations (1) and (2)):

$$\text{Nominal fuel flow [kg/s]} = \eta \cdot T \tag{1}$$

$$\eta\ [\text{kg/(min·kN)}] = C_{f1}\left(1 + \frac{V_{TAS}}{C_{f2}}\right) \tag{2}$$

where T is the thrust, η the thrust specific fuel consumption, C_{f1} and C_{f2} thrust specific fuel consumption coefficients, which are dependent on aircraft model, but not on aircraft mass. If, as a first approximation, the thrust-to-weight ratio (*i.e.* the efficiency factor for total aircraft propulsion) and the

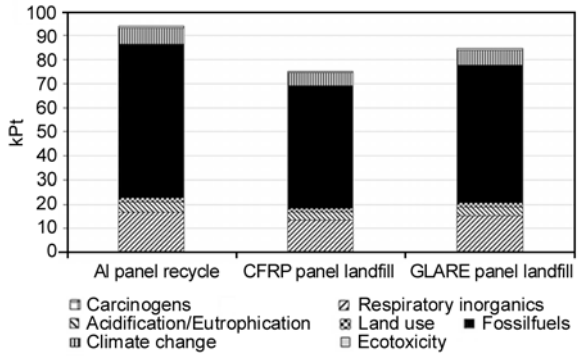

Figure 2. Single score impact results for the entire lifecycle of Al 2024, CFRP and GLARE panels installed on a civil aircraft (freight)

cruise speed are assumed to be mantained constant when replacing metals with composites in a specific aircraft type, fuel consumption can be assumed to be proportional to the total weight of the aircraft.

All panels were assumed to be designed for installation on a civil aircraft with a life time of 30 years and a daily range of 14 000 km [19]. The total distance covered by the aircraft during its lifetime was therefore estimated to be around 150 million km. The panels can be considered as a load that has to be carried by the aircraft during each flight. The functional unit for the transport of the panels, expressed in [t·km], was calculated for each panel and implemented into a LCA transport model for freight transport.

Figure 2 is a single score impact graph showing the total environmental impact that the panels produce over their entire life cycle.

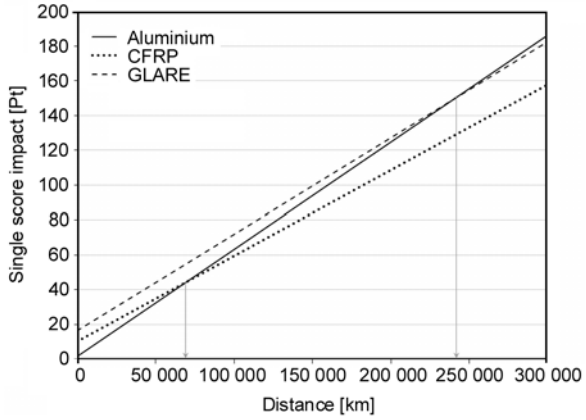

Figure 3. Break even scenarios for single score environmental impact of CFRP and Aluminium plates and GLARE and Aluminium plates. The break-even distance for CFRP is considerably lower than for GLARE. Method: Eco-indicator 99 (E) V2.05 / Europe EI 99 E/E.

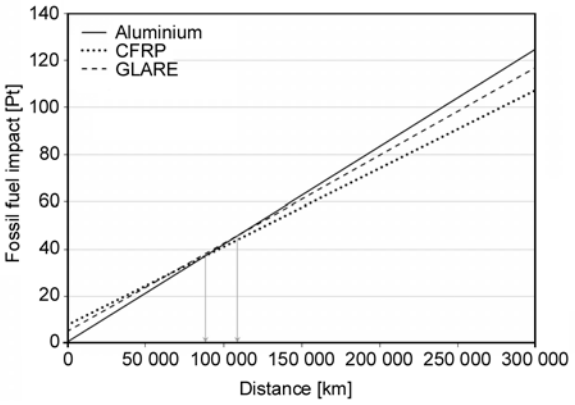

Figure 4. Break even scenarios for fossil fuel depletion impact of CFRP and Aluminium plates and GLARE and Aluminium plates. Method: Eco-indicator 99 (E) V2.05 / Europe EI 99 E/E

From Figure 2 it can be seen that over an entire life cycle the Al-2024 is more environmentally harmful than CFRP and GLARE. It can also be seen that the fossil fuel use impact category dominates the total impact for the three panels. Break-even graphs can also be created, which show the amount of distance that is travelled by the aircraft before the lighter materials become environmentally preferential. Figure 3 shows the break-even plot for single score impact.

From Figure 3 it can be seen that the break-even point for CFRP is approximately 70 000 km and for GLARE panel it is about 240 000 km. Break-even plots have also been created with regards to the fossil fuel impact category (Figure 4).

Figures 4 and 5 illustrate that emissions related to climate change are paid back with the fastest turnover, followed by the fossil fuel consumption. These break-even distances can be translated in to times using the speed of the aircraft, which for freight conditions is 750 km/h at typical cruise speed. Table 1 shows the break-even distances and times with respect to single score, climate change and fossil fuel consumption.

Table 1. Comparison of break-even times for various impact categories for CFRP and GLARE as replacement for Aluminium 2024 plates

	CFRP		GLARE	
	Distance [km]	**Time [hours]**	**Distance [km]**	**Time [hours]**
Single Score	70 000	93	240 000	320
Fossil Fuel	85 000	113	105 000	140
Climate Change	45 000	60	120 000	160

4. Case study: LCA of a tubular component

Having shown the potential benefits of composite materials implemented into aircraft structures, a case study is presented here, following the same methodology and using data for a real component obtained directly from the manufacturer. Unfortunately, due to the strict confidentiality policies in the aviation tier sector , the use of the component cannot be revealed. Despite representing only a few percent of the total weight of an aircraft, steel is still present in aircraft structures and some specific parts made of steel can be replaced with CFRP.

4.1. Components and manufacturing methods

The component analysed in this LCA study is a currently utilised commercial application manufactured at Advanced Manufacturing Research Centre with Boeing, Sheffield, UK. The tubular component had approximate length of 660 mm, inner diameter of 670 mm, and wall thickness of 10 mm. The composite contained approximately 75% hoop fibre, and the resin system was standard epoxy MTM49-3 with the density of 1.78 g/cm^3. Standard Robot Arm power required to manufacture the component using Automatic Fibre Placement (AFP) was 25 kW over 230 minutes. Autoclave manufacturing method used for curing of the component required 20 kW over 240 minutes. The equivalent steel tube used in LCA model had the same dimensions with different wall thickness, 5 mm. The manufacturing of the steel tube consisted of seam welded rolled steel sheet.

4.2. LCA results

For the purpose of the LCA assessment in this particular application, it was of particular importance to compare the initial materials production emissions with the component used in service. Higher initial score for CFRP structure was expected due to the recyclable nature of steel, with the emissions being immediately offset by LCA model. In order to provide data for life-cost analysis of the component, it was important to calculate the break-even points in transport which would effectively provide an estimate of the effectiveness of CFRP in this particular case. Figure 5 shows the cumulative damage to climate involving the single score of emissions and hazardous substances arising from CFRP tube manufacturing and disposal. The analysis of various disposal scenarios did not show any significant variations and thus the incineration was selected to be the representative disposal scenario in this study. According to the LCA model used, incineration had approximately the same impact as landfilling because the emissions from incineration were considered to displace an equivalent amount of coal in a power-station, and, on the other hand, landfilling of composite materials was considered free of any toxic leachate due to the chemical stability of these materials and the efficient landfill system in the UK. It may be concluded that fossil fuel burning from the raw materials processing and component manufacturing contributes the highest level of emissions; considering that, in mass scale production each

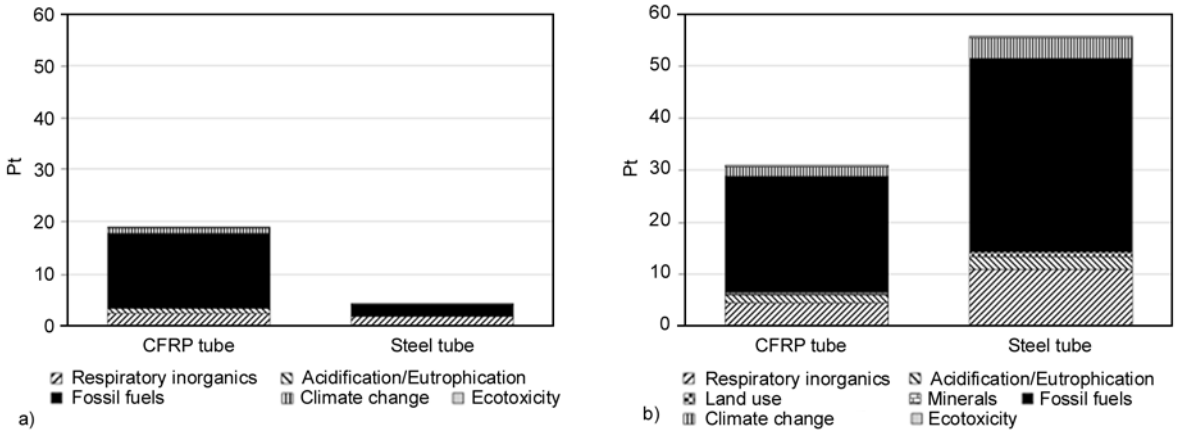

Figure 5. Single impact score calculated for a) CFRP and steel tubes in raw materials production, manufacturing and disposal, and b) after 10 000 km in air transport, showing significant emissions savings due to the implementation of lightweight CFRP structure. Only impact categories with significant contributions to the overall score are represented.

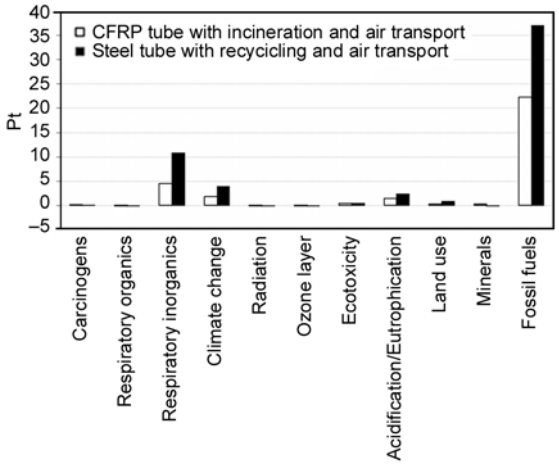

Figure 6. Weighting impact score calculated for CFRP and steel tubes in raw materials production, manufacturing and disposal, and after 10 000 km in air transport. The absolute breakdown of the impact factors shows the most important contributions to pollution and RF index.

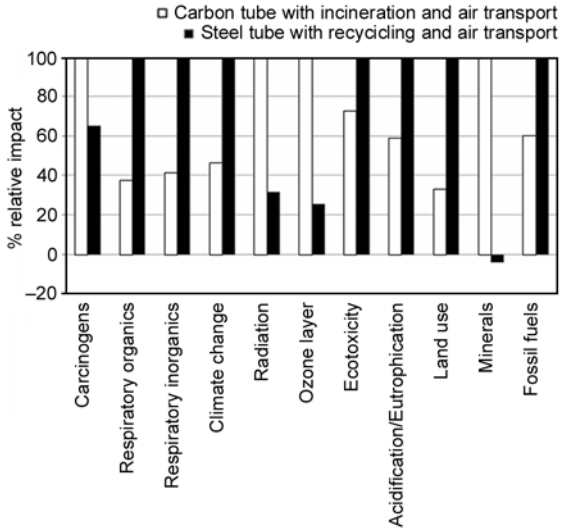

Figure 7. Normalised scores calculated for CFRP and steel tubes in raw materials production, manufacturing and disposal, and after 10 000 km in air transport. Each higher score value is raised to 100% and the lower shown relative in comparison.

parameter will undergo multiplication and thus become more significant. The single impact score improves dramatically for CFRP compared to its predecessor steel component once utilised in the air transport. However, the total impact score still needs to be further assessed in order to evaluate its actual effect onto the environment.

Clearly, the most important factor in this instance is the fossil fuels parameter which takes into account raw production, processing and burning of fossil fuels in the emissions score. Respiratory inorganics and climate change follow as byproducts of all parameters included in the four stages of LCA. Although other parameters are insignificant compared to those three (Figure 6), their values will rise with further operational life of the components and their contribution to the pollution of the ecosystem may still prove to be significant. However, the results show that the implementation of CFRP will significantly improve the overall impact in each LCA parameter over the time in use. In order to observe their relative impacts, the normalisation of the results is shown in Figure 7. Although CFRP shows a significant overall improvement in the emissions score after only one international flight, longer time in operation is required to achieve benefits in the presence of carcinogens, radiation, ozone layer depletion and minerals.

The CFRP and steel tube models were also subjected to three different transport scenarios in order to deteremine the emissions savings once the component is utilised in fuel-saving operation and service. The component was analysed in (i) air transport, cargo aircraft, (ii) road transport, lorry (7.5 t < weight < 16 t) and (iii) marine transport, ocean cargo transporter. The purpose of this analysis was to identify the break-even scenario for each transport type, in order to assess i) the efficiency of the component and ii) the efficiency of the transport scenarios, which are important elements of operational life-cycle assessment.

The results are presented in Table 2 and indicate the high level of implemented CFRP component's environmental efficiency in air transport compared to the other transport scenarios. Based on the average cruise speed for transport aircraft (750 km/h), motorway driven lorry speed (80 km/h) and ocean cargo carrier (40 km/h), the above values for break even distances [km] can be translated into break even times [h] for each type of the transport analysed in this LCA model. Thus, although the marine

Table 2. Comparison of various transport scenarios and their break-even times for steel and CFRP tubes using a single score Ecoindicator 99

Transport scenario	Break-even distance [km]	Break-even time [h]
Air transport	3 600	4.8
Road transport	13 600	170.0
Marine transport	373 000	9325.0

transport appears to be the most effective in terms of emissions savings, weight saving exemplified in the replacement of the steel tube with CFRP tube of the same dimensions will yield the most dramatic emissions saving in air transport.

5. Conclusions

A life cycle assessment (LCA) of CFRP, GLARE and Aluminium 2024 plates used as aircraft panels was performed to determine potential emissions savings of lightweight composites over the life of the component. It was shown that, despite being more energy intensive to manufacture and more difficult to dispose of, CFRP and GLARE can lead to substantial decrease in the overall environmental impact when used in aerospace due to the high fuel consumption during air transport. The break-even distances above which CFRP and GLARE start showing a net reduction of environmental damage compared to Aluminium 2024 were respectively 70 000 and 240 000 km.

Subsequently, a case study was presented on LCA of a CFRP component, which replaced a steel tube, and analysed in several different applications. Real manufacturing data were used and showed in this case a more dramatic reduction in the overall environmental impact by using the composite component. In this case, the break even for replacing a steel component with CFRP was achieved after 3 600 km, corresponding to approximately 5 h of air transport. Lightweight composite structures and hybrid composites produce dramatic positive effect on the total emissions savings when used in the aviation transport. Fossil fuel consumption and the subsequent CO_2 emissions are most significantly reduced. Other aspects such as carcinogens and ozone layer depletion require more hours in service to show benefits from the implementation of lightweight structures. Other transport scenarios have shown also to benefit from the implementation of lightweight structures, however they require more hours in operation to realise such environmental benefits, due to their already lower effective emissions compared to the air transport. The areas to further investigate would be the environmental effect of different disposal scenarios of composites in the environment, and their optimised, automatic manufacturing methods.

Acknowledgements

The authors wish to acknowledge Omega T2 for their financial support of this project.

References

[1] Macintosh A., Wallace L.: International aviation emissions to 2025: Can emissions be stabilised without restricting demand? Energy Policy, **37**, 264–273 (2009). DOI: 10.1016/j.enpol.2008.08.029

[2] Penner J. E., Lister D. H., Griggs D. J., Dokken D. J., McFarland M.: Aviation and the global atmosphere. Cambridge University Press, Cambridge (1999).

[3] Lee D. S., Pitari G., Grewe V., Gierens K., Penner J. E., Petzold A., Prather M. J., Schumann U., Bais A., Berntsen T., Iachetti D., Lim L. L., Sausen R.: Transport impacts on atmosphere and climate: Aviation. Atmospheric Environment, **44**, 4678–4734 (2010). DOI: 10.1016/j.atmosenv.2009.06.005

[4] Burkhardt U., Kärcher B., Schumann U.: Global modeling of the contrail and contrail cirrus climate impact. Bulletin of the American Meteorological Society, **91**, 479–484 (2010). DOI: 10.1175/2009BAMS2656.1

[5] Lee D. S., Fahey D. W., Forster P. M., Newton P. J., Wit R. C. N., Lim L. L., Owen B., Sausen R.: Aviation and global climate change in the 21st century. Atmospheric Environment, **43**, 3520–3537 (2009). DOI: 10.1016/j.atmosenv.2009.04.024

[6] Takeda K., Takeda A. L., Bryant J., Clegg A. C.: Systematic review of the impact of emissions from aviation on current and future climate. The Aeronautical Journal, **112**, 493–522 (2008).

[7] Dreyer L. C., Niemann A. L., Hauschild M. Z.: Comparison of three different LCIA methods: EDIP97, CML2001 and Eco-indicator 99. Does it matter which one you choose? The International Journal of Life Cycle Assessment, **8**, 191–200 (2003). DOI: 10.1007/BF02978471

[8] Soutis C.: Fibre reinforced composites in aircraft construction. Progress in Aerospace Sciences, **41**, 143–151 (2005). DOI: 10.1016/j.paerosci.2005.02.004

[9] Aeronautics and transport: Beyond vision 2020 (towards 2050). Advisory Council for Aeronautics Research in Europe, Brussels (2010).

[10] Aviation Legal Eye – Spring 2010. Stephenson Harwood, London (2010).

[11] Campbell F. C.: Manufacturing technology for aerospace structural materials. Elsevier, Amsterdam (2006).

[12] The aircraft at end of life sector: A preliminary study. Engineering and Physical Sciences Research Council, Swindon (2007).

[13] Beck A. J., Hodzic A., Soutis C., Wilson C. W.: Lifecycle assessment to optimise aerospace composites. in 'The 10th International Conference on Deformation and Fracture of Composites, Sheffield, UK' p.19 (2009).
[14] Eco-indicator 99 manual for designers: A damage oriented method for life cycle impact assessment. Ministry of Housing, Spatial Planning and the Environment, Hague (2000).
[15] Campbell F. C.: Manufacturing processes for advanced composites. Elsevier, Amserdam (2004).
[16] Leroy C.: Provision of LCI data in the European aluminium industry: Methods and examples. The International Journal of Life Cycle Assessment, **14**, S10–S44 (2009).
DOI: 10.1007/s11367-009-0068-6
[17] Vlot A., Gunnik J. W.: Fibre metal laminates: An introduction. Kluwer, Dodrecht (2001).
[18] Nuic A.: User manual for the base of aircraft data (BADA). Revision 3.6. EUROCONTROL Experimental Centre, Bretigny-sur-Orge (2004).
[19] Peel C. J., Gregson P. J.: Design requirements for aerospace structural material. in 'High performance materials in aerospace' (ed.: Flower H. M.) Chapman and Hall, London, 1–48 (1995).

eXPRESS Polymer Letters Vol.5, No.3 (2011) 218–227
Available online at www.expresspolymlett.com
DOI: 10.3144/expresspolymlett.2011.21

Effect of nanofillers on the properties of a state of the art epoxy gelcoat

P. Karapappas, P. Tsotra[*]*, K. Scobbie*

Huntsman Advanced Materials, Klybeckstrasse 200, Basel 4057, Switzerland

Received 29 July 2010; accepted in revised form 2 November 2010

Abstract. In this work, the effect of the inclusion of electrically conductive and non-conductive nanofillers in a state of the art epoxy gelcoat was studied. The conductive fillers used were multi-wall carbon nanotubes and exfoliated nanographite. The non-conductive ones were nanoclay and nano-titanium dioxide. The content of the nanofillers was 0.65% per weight and their inclusion took place using high shear mixing devices. The conductive fillers showed an increase in tensile and fracture properties, as well as in the thermal properties whereas the non-conductive fillers did not show any improvement on the fracture properties. The glass transition temperature was practically unaffected by the presence of the nanofillers while conversly, the coefficient of thermal expansion was decreased for all the nanofillers for temperatures above the glass transition temperature. Finally, weatherometer tests showed that the nanofillers contribute into less weight losses in comparison with the reference epoxy gelcoat.

Keywords: *nanocomposites, nanofillers, gelcoats, weatherometer, mechanical properties*

1. Introduction

There have been numerous studies that have demonstrated that, the use of conductive nanofillers like carbon nanotubes (CNTs), carbon nanofibres (CNFs) or nanographite can improve the mechanical properties of epoxy resins and their composites [1–5]. Also the electrical conductivity of polymers containing organic nanofillers can be further improved [6–10] since only a small fraction of nanotubes or nanographite is needed to form the percolation conductive network. The optimal dispersion of the nanofillers in the resin is a key factor for achieving the aforementioned properties. Moreover it has been established that, the CNTs can be used as sensors monitoring strain, applied loading, or even sense damage induced, etc. [11–14]. The thermal stability of polymers has also been enhanced with the inclusion of nanographite because of the 'barrier effect' which is strongly related to its shape and structure [15–16]. However the effect of the above mentioned fillers is not always the same on the glass transition temperature and is a phenomenon depending on various factors like the morphology and structure of the nanofillers, its chemical treatment, purity, functionalisation, etc [17]. Also, some of the more recent studies, used nanoclays for the reinforcement of carbon fabrics achieving important mechanical enhancements along with flame retardant abilities, i.e. reduce the peak heat release rate [18–23]. Titanium dioxide has also been used as a thermal barrier on composite application increasing the oxidation and degradation temperature of carbon fibres etc. Treating TiO_2 with amino-silane coupling has increased the impact and tensile properties of polystyrene. Finally, the pyrolysis behaviour of PVA composites has been enhanced with the addition of nano-TiO_2 [24–26]. Nevertheless, no research has been done so far on

[*]Corresponding author, e-mail: panayota_tsotra@huntsman.com

the effect of nanofillers on the properties of gelcoats. The current work focuses on how the properties of a state of the art epoxy gelcoat, can be enhanced with the addition of different nanofillers.

A gelcoat is a material used to provide a high quality finish on the visible surface of a fibre-reinforced composite material. The most common gelcoats are based on epoxy or unsaturated polyester resin chemistry. Gelcoats are modified resins which are applied to moulds in the liquid state. They are cured to form crosslinked polymers and are subsequently backed up with composite polymer matrices, often mixtures of polyester resin and fibreglass or epoxy resin with glass, kevlar and/or carbon fibres. The manufactured component, when sufficiently cured and removed from the mould, presents the gelcoated surface. This is usually pigmented to provide a coloured, glossy surface which improves the aesthetic appearance of the component. Gelcoats are designed to be durable, providing resistance to ultraviolet degradation and hydrolysis. Specialised gelcoats can be used to manufacture the moulds which in turn are used to manufacture components. These require very high levels of durability to overcome the mechanical and thermal stresses encountered during the curing and demoulding processes.

In the current work an effort was made to enhance the mechanical and thermal properties of the RenGel™ 5200 gelcoat of Huntsman Advanced Materials GmbH, Switzerland with the use of nanofillers. Fillers in any size have for many years had a high significance in the plastics industry. Nanofillers are basically understood to be additives in solid form where on dimension is in nanoscale and, differ from the polymer matrix in terms of their composition and structure. They generally comprise inorganic materials or organic materials. Inactive fillers or extenders raise the quantity and lower the prices, whereas active fillers bring about targeted improvements in certain mechanical or physical properties. The activity of active fillers may have a variety of causes, such as the formation of a chemical bond or filling of a certain volume and disruption of the conformational position of a polymer matrix, and also the immobilization of adjacent molecule groups and possible orientation of the polymer material.

2. Experimental

As reference material the RenGel™ SW 5200 epoxy gelcoat of Huntsman Advanced Materials GmbH, Basel, Switzerland was used and was cured with Ren® HY 5212 Fast. The formulation of the gelcoat is based on Araldite® MY 0510, a trifunctional glycidylamine epoxy resin. The nanofillers that they were used to produce four different nano-enhanced gelcoats were the following: (i) MWCNTs Baytubes® C150P by Bayer™, Monheim, Germany with 95% purity, diameter between 13–16 nm, length >1 μm and, density 1.4–1.6 g/cm^3, (ii) the exfoliated nanographite platelets were by XG Sciences, Michigan, USA with trade name xGnP® Exfoliated Graphite Nanoplatelets. The platelets had 97% purity, thickness 5–10 nm and, density 1.9–2.2 g/cm^3, (iii) Cloisite® 30B by Rockwood Additives, Austin, USA was chosen as the nanoclay filler. This particular montmorillonite clay filler has purity over 98%, length between 2–13 μm, thickness in nano and, density 1.98 g/cm^3 and finally, (iv) nano-titanium dioxide in rutile form and 99% pure was used by MK Nano, Ontario, Canada with diameter of 50 nm and density of 4.23 g/cm^3. All the nanofillers were used in 'as received' form i.e. no surface modification or functionalisation took place.

The way that the nanofillers were introduced into the gelcoat was via their inclusion in the plain resin itself, forming thus a masterbatch. Then, the produced masterbatch was used as part of the formulation of the gelcoat. The dispersion of the nanofillers at 2% p.wt into the epoxy resin took place by using a high shear device. High shear devices include mixers, dissolvers, 3 roll-mills, etc and introduce high shear forces via rotating parts and sometimes turbulent flow, so as to break the agglomerates of the nanofillers and distribute the fillers uniformly in the resin.

In this work, for the inclusion of all the nanofillers a 3 roll-mill of 'S' series by Exakt®, Norderstedt, Germany was used. A three roll mill (also known as calender) is a machine tool that uses the shear force created by three horizontally positioned rolls rotating at opposite directions and different speeds relative to each other to mix, refine, disperse, or homog-

enize viscous materials fed into it. The three adjacent rolls of a three roll mill rotate at progressively higher speeds. This milling cycle can be repeated several times to maximize dispersion. The gaps between the rolls can be mechanically or hydraulically adjusted and maintained. Typically, the gap distance is far greater than the particle size. In some operations, they are gradually decreased to achieve the desired level of dispersion. Also in the most advanced versions the rolls can be set so as to produce constant shear forces and they can also be heated or cooled independently so as to adjust the mixture's viscosity accordingly. The mixture of resin with the nanofillers was passed twice from the 3 roll-mill with the gap between the rolls to be set at 5 microns and the tip speed was set at 1.25 m/sec, in the second pass the gap was reduced at 2 μm and the tip speed further increased at around 1.69 m/sec. At this point, it must be noted that the gap of 2 μm was set manually while preparing the masterbatch. With the Exakt® 120S used there is no way to control and maintain the gap constant throughout the mixing operation. For the preparation of the gelcoat a planetary mixer was used by EM, Italy. Contrary to conventional planetary mixers, the two blade configurations sweep the wall of the can clockwise and rotate in opposite directions at about three times the speed of travel. The shear blades displace the material from the walls of the can and by their overlapping action the center carry the particles towards the agitator shafts, therefore producing a large field of shear forces. By this means even highly viscous and cohesive material can be efficiently mixed. The masterbatch was introduced to the mixer and then the other fillers were added, one at a time. The duration of the mixing process was around 5 hours, the discs employed were impellers of 70 mm diameter with rotational speed around 200 rpm and, the temperature was set at 80°C. The mixing ratio of the gelcoat with the liquid hardener was 100:22 per weight and the curing schedule was the following: 24 hours room temperature + 12 hours at 40°C + 2 hours at 80°C + 2 hours at 100°C + 2 hours at 120°C + 2 hours at 140°C + 2 hours at 160°C + 2 hours at 180°C + 12 hours at 200°C and slowly cooled down to room temperature. The resulting final mixture was cast in closed metallic moulds of different thicknesses so as to produce specimens for various tests.

In order to investigate and evaluate the effect of the nanofillers on the properties of the epoxy gelcoat several tests were performed. These tests include viscosity measurements at room temperature using a Brookfield rheometer by Brookfield, Boston, USA and the ASTM D2393 standard. The tensile coupons were prepared according ISO 527, the fracture coupons according to ISO 13586 and the torsion DMA according to ISO 6721. Moreover, the DC electrical volume conductivity measurements perfromed by a digital Keithley Electrometer 2000 by Keithley Instruments Inc, Cleveland, USA according to the IEC 60093 standard and, the thermal conductivity was measured by the C-Therm TCi, instrument of Setaram, Caluire, France. The coefficient of linear thermal expansion was measured by the means of a TMA by Mettler Toledo, Zurich, Switzerland and according to the ISO standard 11359-2. Finally the weatherometer test took place by following the SAE J1885 standard for 300 hours using a Ci3000+ Xenon Weather-Ometer® by Atlas, Chicago, USA.

3. Results and discussion

The first chart (Figure 1) is a comparison of the rheological properties of the gelcoats with the different nanofillers against the reference gelcoat at room temperature. The volume fraction for the nanofillers was approximately 0.43, 0.31, 0.33 and 0.15% for the CNTs, the exfoliated nanonographite, the nanoclay and the titanium dioxide respectively. It can be seen that for shear rates of around 10 Hz and above, all the gelcoats have in practice the same viscosity. However at lower shear rates the high aspect ratio of the CNTs and the layered structure of the nanoclay increased the viscosity of the refer-

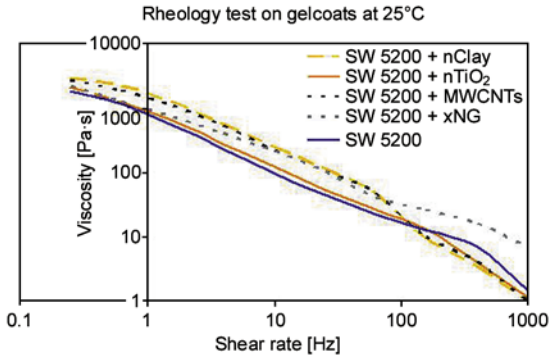

Figure 1. Log-log plot of the rheology properties of the epoxy gelcoats

ence gelcoat around 30–40%. The above effect is strongly connected with the structure, morphology, density, volume fraction and the aspect ratio of the fillers. Therefore the carbon nanotubes by having a larger aspect ratio (thinner and longer) and higher volume fraction than the exfoliated nanographite have a bigger impact on the resin's viscosity. Moreover, the nanoclay layers have a high aspect ratio and each one is approximately 1 nm thick, with their diameter varying from 30 nm to several microns or larger having thus a bigger impact on the resin's viscosity than the titanium dioxide. Titanium dioxide has also lower volume fraction than the nanoclay used in this study. Besides, the reference gelcoat and the nano-doped ones are thixotropic and therefore no re-agglomeration on segregation was observed after storing them at room temperature for more than 90 days. The high polarity of the matrix is responsible for the thixotropy of the resulting gelcoats.

At this point it should be noted that given that the reference epoxy gelcoat is a commercially available system, the SEM pictures taken to evaluate the dispersion of the nanofillers cannot be disclosed since they could also reveal the type of the other microfillers used for its formulation. The SEM micrographs revealed that all nanofillers had a good dispersion and that a quite homogeneous mixture was manufactured. By stating 'good dispersion' the authors suggest that some small agglomerations were present but all the produced mixtures were directly comparable.

In the following Table 1 the results summary from the tensile tests are given, while Figure 2 shows representative stress-strain curves for the epoxy gelcoats. The beneficiary effect of all the nanofillers on the tensile properties is obvious. For all the cases the Elastic modulus, along with the maximum stress and strain at failure were significantly increased. The increase of the maximum stress values was in the range of 35–65% and for the maximum strain at failure was between 26–97%. The

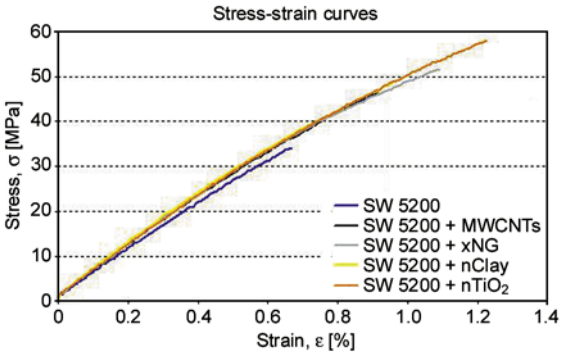

Figure 2. Stress-strain curves of the epoxy gelocoats

high aspect ratio of the CNTs, the high surface area (high interfacial area between nanofiller and polymer) and their excellent mechanical properties: elastic modulus of around 0.8 TPa, tensile strength of around 150 GPa and elongation at break larger than 10%, contributed to the increase of the tensile properties of the epoxy gelcoats [27–30]. While the layered exfoliated structure and the platelet shape of the nanographite is responsible for the enhanced tensile properties [31–34]. The reinforcing mechanisms of ceramic fillers like the titanium dioxide and the montmorillonite clay that were used in the present study have been attributed to their large surface area and surface reactivity of the inorganic phase, the corresponding restricted mobility of the polymer chains and to the increase in the effective particle volume fraction in the nanocomposite [35–37].

The fracture properties of the gelcoats can be seen in Figure 3. Once again the positive effect of the CNTs and the exfoliated nanographite is demonstrated. However in the contrary with the tensile properties, the ceramic fillers bring minor or no improvement at all. Specifically, in the case of the nanoclay, the fracture properties have decreased with respect to the reference system around 8.5%. The differences on the properties for the organic and inorganic fillers are assigned to the dissimilar aspect ratios. A lot of researchers have concluded that the reinforcing mechanisms of the clays are

Table 1. Tensile properties of the nanomodified gelcoats versus the reference gelcoat

Gelcoat reference	E		σ_{max}		ε	
	[GPa]	st.dev	[MPa]	st.dev	[%]	st.dev
Rengel SW 5200	5.299	0.024	34.98	2.85	0.670	0.025
Rengel SW 5200 + MWCNTs	5.654	0.039	47.68	5.86	0.850	0.041
Rengel SW 5200 + xnGraphite	5.823	0.064	54.00	3.42	1.160	0.026
Rengel SW 5200 + nClay	5.819	0.066	48.42	5.26	0.970	0.018
Rengel SW 5200 + $nTiO_2$	5.604	0.079	57.84	2.21	1.320	0.023

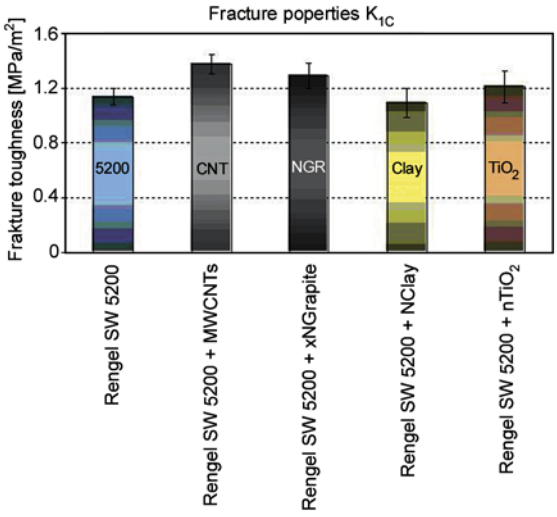

Figure 3. Fracture properties of the nanomodified gelcoats versus the reference gelcoat

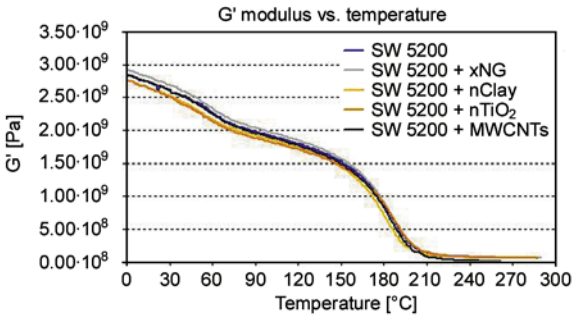

Figure 4. Prime modulus in torsion (G'), versus temperature for the epoxy gelcoats

crack arrest, crack pinning, crack bifurcation and shear deformation [38–40]. The inorganic fillers i.e. the nanoclay and the titanium dioxide have aspect ratios between 10–100. On the other hand the CNTs and the nanographite have aspect ratios greater than 500 (sometimes even 1000) and elongation at break greater than 10%. Their reinforcing mechanisms have been revised in the literature and claim that the significantly large aspect ratio of the fillers which allows them to act as nano-bridges between the notch edges. Extra energy is needed in order to pull them out from the matrix or break them and then initiate the crack propagation. This extra energy is then translated into improved fracture toughness properties [1, 4, 14, 27–30]. When directly comparing the two inorganic nanofillers, it is clear that the titanium dioxide particles are nanosized and therefore they can be more effective on reinforcing the fracture properties of the polymer than the clays which are nanosized only through thickness. Also, by comparing the tensile data of the previous section is clear that the inclusion of the nanoclay made the epoxy gelcoat more brittle than the gelcoat with titanium dioxide. A more brittle material is less fracture tolerant and hence the difference on the fracture properties between the two inorganic fillers.

The effect of the rigid nanofillers on the glass transition temperature and on the storage and loss torsion modulus is shown in Table 2. The glass transition temperature, T_g and the storage modulus G' remained practically unaffected by the presence of the fillers. Nevertheless, tanδ was decreased around 30% for all the nanofillers i.e. transforming the nanodoped epoxy gelcoats into a more 'elastic' material. Moreover, Figure 4 presents the G' modulus graph versus the tested temperature range where it can be seen that the effect of the nanofillers is not very significant.

In Figure 5. the DC volume conductivity measurements for the gelcoats are depicted. One may highlight that the inclusion of the conductive fillers i.e. CNTs and nanographite has further increased the

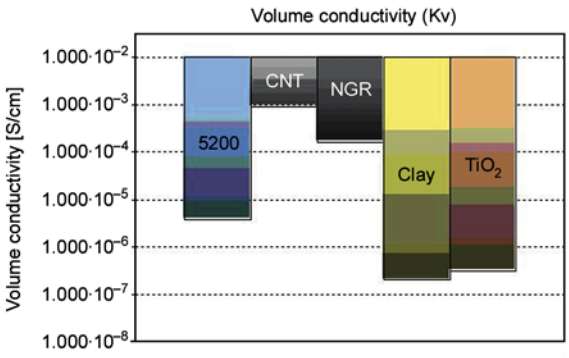

Figure 5. Volume conductivity properties of the nanomodified gelcoats versus the reference gelcoat

Table 2. DMA torsion properties of the nanomodified gelcoats versus the reference gelcoat

Gelcoat reference	T_g [°C]	G′ [Pa]	G″ [Pa]	tanδ
Rengel SW 5200	200.8	2.59·10^9	3.29·10^7	0.54979
Rengel SW 5200 + MWCNTs	201.7	2.68·10^9	3.53·10^7	0.36472
Rengel SW 5200 + xnGraphite	200.9	2.75·10^9	2.81·10^7	0.37041
Rengel SW 5200 + nClay	197.8	2.58·10^9	3.37·10^7	0.38239
Rengel SW 5200 + nTiO$_2$	204.6	2.57·10^9	1.82·10^7	0.37492

conductivity of the reference gelcoat between 2 and 1.5 orders of magnitude. Extensive researches on carbon nanotubes and their polymers have established that CNTs can be conductive, semi-conductive or even metallic depending on their structure and that only a small weigh fraction is needed to form a percolating network in a polymer or in a composite. The above is directly related to their graphene structure and their high aspect ratio and surface area which in turn is translated into electrical conductivity values of 10^6 to 10^7 S/m [6, 9–11]. Additionally, the exfoliated nanographite with its basal plane to be inert ($sp^2 + \pi$) and identical to the wall of a carbon nanotube it has analogous electrical properties bringing thus similar improvement on the electrical properties [5, 8, 16]. The other two nanofillers actually reduced the electrical conductivity of the gelcoat about 2 orders of magnitude. This was expected since their ceramic nature involves high internal electrical resistance making thus, the gelcoat less more electrically resistant. At this point it must be noted that all the electrical measurement performed for DC frequency and that AC measurements will be performed as part of the continuation of this research, along with other tests, since the hybrid role of TiO_2 has to be further investigated and evaluated [41]. Other tests that are currently being performed are abrasion resistance, water and salted water absorption and degradation.

The effect of all the nanofillers on the thermal properties of the state of the art epoxy gelcoat is shown in Table 3. All the nanofillers by being thermally conductive improved the thermal conductivity of the gelcoat in the range of 8 to 16%. Several research studies have claimed that the presence of nano-fillers like the CNTs, nanographite, nanoclay and titanium dioxide has been beneficial for the thermal stability of thermoplastics and thermosets. The reason for the abovementioned amelioration is not only the intrinsic properties of the fillers themselves i.e. CNTs have high melting point and thermal conductivity of at least 3000 W/(m·K), In systems like the ones under investigation, the thermal conductivity difference of the phases as well as the interfacial thermal resistance between them have a significant influence on the achieved thermal conductivity of the final nano-composite, besides the geometrical characteristics of the nano-fillers. The interfacial thermal resistance together with the resulting pathways define the phonon movement and as a result the thermal conductivity of the material. CNTs are able to create a critical path to diffuse thermal energy at this loading level. Based on an experimental study on thermally conductive composites filled with platelet-shaped boron nitride particles, it was suggested that fillers with platelet shape offer advantages over other spherical or cylindrical morphologies because they can overlap with a large contact area permitting much closer contact between adjacent platelets and reducing the thermal contact resistance [17, 34–39].

Table 3. Thermal conductivity properties of the nanomodified gelcoats versus the reference gelcoat

Gelcoat reference	Thermal conductivity [W/(m·K)]	st. dev
Rengel SW 5200	0.54	0.0007
Rengel SW 5200 + MWCNTs	0.60	0.0021
Rengel SW 5200 + xnGraphite	0.63	0.0018
Rengel SW 5200 + nClay	0.61	0.0014
Rengel SW 5200 + nTiO_2	0.58	0.0011

In addition, Table 4 depicts the data obtained for the coefficient of linear thermal expansion (CLTE) tests. The tests were performed at below and above the glass transition temperature, T_g, of the reference gelcoat i.e. 200°C. The effect at the CLTE value of all the nanofillers below T_g seems to be of no practical use. Nevertheless, the CLTE values for all the nano-enhanced epoxy gelcoats are reduced. In other words the nano-enhanced gelcoats will expand less than the reference material. Materials expand because an increase in temperature leads to greater thermal vibration of the atoms in a material, and hence to an increase in the average separation distance of adjacent atoms or polymer molecules in the

Table 4. Coefficient of linear thermal expansion values for above and below glass transiton temperature

Gelcoat reference	Below		Above	
	T_g [m/(m·°C)]	st.dev	T_g [m/(m·°C)]	st.dev
Rengel 5200	49.98	0.20	128.61	1.10
GC MY510 + MWCNTs	50.01	0.26	107.11	1.90
GC MY510 + xnGraphite	51.11	0.59	120.77	1.47
GC MY510 + nClay	49.60	0.60	112.00	0.91
GC MY510 + nTiO_2	50.22	0.42	125.26	1.50

case of thermosets. The size, the high surface area and the aspect ratio of the the fillers are responsible for the aforementioned improvement. The nanofillers occupy certain space among the polymer macromolecules making thus their vibration and their separation more difficult to occur.

Carbon based products ranging from coatings to wood and plastics form free radicals when exposed to ultra-violet (UV) radiations. These free radicals chemically react with oxygen to yield a photo oxidized product which modifies the product appearance and also its mechanical properties. The weatherometer (WOM) device uses a combination of carbon arc, UV radiation and water spray to simulate destructive weather conditions in an accelerated manner. Although precise equivalents are impossible to determine, a practical calculation is: 300 hours in the weatherometer equals one year real time. The data from WOM tests concern discolouration and colour fading of the samples and weight loss. In our study, the reference epoxy gelcoat was black and it remained black after the addition of the different nanofillers. As a consequence the discolouration/colour fading data were of no-practical value with the differences among the five types of specimens to be trivial. Therefore only the weight loss percentage data were of significance and are presented in the Figure 6. The weight loss for the nano-filled epoxy gelcoats is less than the reference gelcoat, meaning that the reference samples were more prone to environmental degradation. In other words, in a real life situation the nanodoped gelcoats should have an extended life-time in comparison with the RenGel™ SW 5200. Even though weatherometer results of nanodoped epoxies have not been previously published in the literature, there are however studies on the effect of nanofillers on the tribology, abrasion resistance and UV degradation properties of nano-enhanced resins. The presence of CNT can have a dramatic reinforcement effect on the nature of degradation by both high-energy radiations, where polymer-free radicals are mainly responsible for the proliferation of degradation. In addition, CNT networks can effectively disperse the radiation. The wear rate was reduced by a factor of 5.5 when the friction behaviour of MWCNTs epoxy polymer was studied [42–43]. As for the ceramic nanofillers, nano titanium dioxide in rutile form proved to be very effective on

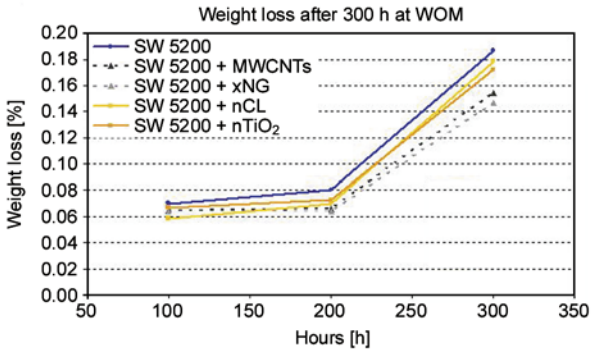

Figure 6. Weight loss data of weatherometer test of the nano-modified gelcoats versus the reference gelcoat

absorbing wavelengths below 350 nm and thus operating as a pacifier for isocyanate based acrylic coatings [44]. One may summarise that the use of nanofillers in the epoxy glecoat have proved their potential to enhance the resistance of the gelcoat in harsh environmental conditions.

4. Conclusions

In this work, the effect of the addition of four different commercially available nanofillers into a state of the art epoxy based gelcoat was studied. The nanofillers were introduced into the gelcoat in the form of a masterbatch which was prepared by using a high shear mixing device i.e. a 3-roll mill. The presence of the nanofillers brought a lot of improvements in the properties of the gelcoats. The aforementioned improvements include the tensile and fracture properties as well as, the electrical and thermal ones. The presence of the nanofillers also decreased the coefficient of linear thermal expnasion and made the nanodoped epoxy gelcoats more resistant to UV degradation. The addition of CNTs and the exfoliated nanographite lead to an all-around enhancement of properties, while the addition of nanoclay and nano-titanium dioxide was beneficial only for the tensile and thermal conductivity properties. However the inclusion of the nanofillers had no practical impact on glass transition temperature. One of the drawbacks of the introduction of the nanofillers into the resin was the increase of viscosity which can be an issue of processability of those materials when composite manufacturing is considered.

It must be highlighted that the aforesaid improvements in the case of the gelcoats are very important since the gelcoats are already heavily filled with various fillers (organic and inorganic) and they

have been optimised for all-around good performance and properties. The extra properties gained by the addition of the nanofillers therefore are essential.

Acknowledgements

All the aforementioned work has been financially supported by the LAYSA EU-Transport Project with contract number: FP7-AAT-2007-RTD-1. The authors would like to thank Applied Mechanics Laboratory of University of Patras, Greece for their help with the thermal conductivity tests.

References

[1] Karapappas P., Vavouliotis A., Tsotra P., Paipetis A., Kostopoulos V.: Enhanced fracture properties of carbon reinforced composites by the addition of multi-wall carbon nanotubes. Journal of Composite Materials, **43**, 977–985 (2009).
DOI: 10.1177/0021998308097735

[2] Kostopoulos V., Baltopoulos A., Karapappas P., Vavouliotis A., Paipetis A.: Impact and after-impact properties of carbon fibre reinforced composites enhanced with multi-wall carbon nanotubes. Composites Science and Technology, **70**, 553–563 (2010).
DOI: 10.1016/j.compscitech.2009.11.023

[3] Wichmann M. H. G., Sumfleth J., Gojny F. H., Quaresimin M., Fiedler B., Schulte K.: Glass-fibre-reinforced composites with enhanced mechanical and electrical properties – Benefits and limitations of a nanoparticle modified matrix. Engineering Fracture Mechanics, **73**, 2346–2359 (2006).
DOI: 10.1016/j.engfracmech.2006.05.015

[4] Wichmann M. H. G., Schulte K., Wagner H. D.: On nanocomposite toughness. Composites Science and Technology, **68**, 329–331 (2007).
DOI: 10.1016/j.compscitech.2007.06.027

[5] Kalaitzidou K., Fukushima H., Drzal L. T.: A new compounding method for exfoliated graphite–polypropylene nanocomposites with enhanced flexural properties and lower percolation threshold. Composites Science and Technology, **67**, 2045–2051 (2007).
DOI: 10.1016/j.compscitech.2006.11.014

[6] Martin C. A., Sandler J. K. W., Shaffer M. S. P., Schwarz M-K., Bauhofer W., Schulte K., Windle A. H.: Formation of percolating networks in multi-wall carbon nanotube–epoxy composites. Composites Science and Technology, **64**, 2309–2316 (2004).
DOI: 10.1016/j.compscitech.2004.01.025

[7] Thostenson E. T., Chou T-W.: Processing structure multi functional property relationship in carbon nanotube/epoxy composites. Carbon, **44**, 3022–3029 (2006).
DOI: 10.1016/j.carbon.2006.05.014

[8] Fukushima H., Drzal L. T., Rook B., Rich M. J.: Thermal conductivity of exfoliated graphite nanocomposites. Journal of Thermal Analysis and Calorimetry, **85**, 235–238 (2006).
DOI: 10.1007/s10973-005-7344-x

[9] Sandler J., Shaffer M. S. P., Prasse T., Bauhofer W., Schulte K., Windle A. H.: Development of a dispersion process for carbon nanotubes in an epoxy matrix and the resulting electrical properties. Polymer, **40**, 5967–5971 (1999).
DOI: 10.1016/S0032-3861(99)00166-4

[10] Sandler J. K. W., Kirk J. E., Kinloch I. A., Shaffer M. S. P., Windle A. H.: Ultra-low electrical percolation threshold in carbon-nanotube-epoxy composites. Polymer, **44**, 5893–5899 (2003).
DOI: 10.1016/S0032-3861(03)00539-1

[11] Dresselhaus M. S., Dresselhausand G., Avouris P. H.: Carbon nanotubes: Synthesis, structure, properties and applications. Springer, Berlin (2001).

[12] Fernberg, P., Nilsson G., Joffe R.: Piezoresistive performance of long-fiber composites with carbon nanotube doped matrix. Journal of Intelligent Material Systems and Structures, **20**, 1017–1023 (2009).
DOI: 10.1177/1045389X08097387

[13] Vavouliotis A., Karapappas P., Loutas T., Voyatzi T., Paipetis A., Kostopoulos V.: Multistage fatigue life monitoring on carbon fibre reinforced polymers enhanced with multiwall carbon nanotubes. Plastics, Rubber and Composites, **38**, 124–130 (2009).
DOI: 10.1179/174328909X387928

[14] Kostopoulos V., Vavouliotis A., Karapappas P., Tsotra P., Paipetis A.: Damage monitoring of carbon fiber reinforced laminates using resistance measurements. Improving sensitivity using carbon nanotube doped epoxy matrix system. Journal of Intelligent Material Systems and Structures, **20**, 1025–1034 (2009).
DOI: 10.1177/1045389X08099993

[15] Lachman N., Bartholome C., Miaudet P., Maugey M., Poulin P., Wagner H. D.: Raman response of carbon nanotube PVA fibers under strain. Journal of Physical Chemistry C, **113**, 4751–4754 (2009).
DOI: 10.1021/jp900355k

[16] Kim S., Do I., Drzal L. T.: Thermal stability and dynamic mechanical behavior of exfoliated graphite nanoplatelets-LLDPE nanocomposites. Polymer Composites, **31**, 755–761 (2009).
DOI: 10.1002/pc.20781

[17] Kim S., Drzal L. T.: High latent heat storage and high thermal conductive phase change materials using exfoliated graphite nanoplatelets. Solar Energy Materials and Solar Cells, **93**, 136–142 (2009).
DOI: 10.1016/j.solmat.2008.09.010

[18] Allaoui A., El Bounia N.: How carbon nanotubes affect the cure kinetics and glass transition temperature of their epoxy composites? – A review. Express Polymer Letters, **3**, 588–594 (2009).
DOI: 10.3144/expresspolymlett.2009.73

[19] Castenada S., Parra O., Ramirez E., Sanchez S.: Performance of nanoclay in a flame-retardant jacket compound. Wire Journal International, **42**, 70–79 (2009).

[20] Gilman J. W., Kashiwagi T., Lichtenhan J. D.: Nanocomposites: A revolutionary new flame retardant approach. SAMPE Journal, **33**, 40–51 (1997).

[21] Chozhan C. K., Alagar M., Sharmila R. J., Gnanasundaram P.: Thermo mechanical behaviour of unsaturated polyester toughened epoxy–clay hybrid nanocomposites. Journal of Polymer Research, **14**, 319–327 (2007).
DOI: 10.1007/s10965-007-9114-x

[22] Al-Khanbashi A., El-Gamal M., Moet A.: Reduced shrinkage polyester–montmorillonite nanocomposite. Journal of Applied Science, **98**, 767–773 (2005).
DOI: 10.1002/app.22157

[23] Bhat G., Raghavendra R. H., Kamath M. G., Deshpande B.: Nanoclay reinforced fibers and nonwovens. Journal of Engineered Fibers and Fabrics, **3**(**3**), 22–34 (2008).

[24] Boccaccini A. R., Karapappas P., Marijuan J. M., Kaya C.: TiO_2 coatings on silicon carbide and carbon fibre substrates by electrophoretic deposition. Journal of Materials Science, **39**, 851–859 (2004).
DOI: 10.1023/B:JMSC.0000012914.47793.3e

[25] Selvin T. P., Kuruvilla J., Sabu T.: Mechanical properties of titanium dioxide-filled polystyrene microcomposites. Materials Letters, **58**, 281–289 (2004).
DOI: 10.1016/S0167-577X(03)00470-1

[26] Rohan L., Holmes J. A., Campbell P., Karatchevtseva I.: Pyrolysis behaviour of titanium dioxide–poly(vinyl pyrrolidone) composite materials. Polymer Degradation and Stability, **94**, 1882—1889 (2009).
DOI: 10.1016/j.polymdegradstab.2009.03.026

[27] Fiedler B., Gojny F. H., Wichmann M. H. G., Nolte M. C. M., Schulte K.: Fundamental aspects of nano-reinforced composites. Composites Science and Technology, **66**, 3115–3125 (2006).
DOI: 10.1016/j.compscitech.2005.01.014

[28] Spitalsky Z., Tasis D., Papagelis K., Galiotis C.: Carbon nanotube–polymer composites: Chemistry, processing, mechanical and electrical properties. Progress in Polymer Science, **35**, 357–401 (2010).
DOI: 10.1016/j.progpolymsci.2009.09.003

[29] Tran C. D., Humphries W., Smith S. M., Huynh C., Lucas S.: Improving the tensile strength of carbon nanotube spun yarns using a modified spinning process. Carbon, **47**, 2662–2670 (2009).
DOI: 10.1016/j.carbon.2009.05.020

[30] Seyhan T. A., Tanoğlu M., Schulte K.: Tensile mechanical behavior and fracture toughness of MWCNT and DWCNT modified vinyl-ester/polyester hybrid nanocomposites produced by 3-roll milling. Materials Science and Engineering: A, **523**, 85–92 (2009).
DOI: 10.1016/j.msea.2009.05.035

[31] Gibson R. F.: A review of recent research on mechanics of multifunctional composite materials and structures. Composite Structures, **92**, 2793–2810 (2010).
DOI: 10.1016/j.compstruct.2010.05.003

[32] Tsai J-L., Tu J-F.: Characterizing mechanical properties of graphite using molecular dynamics simulation. Materials and Design, **31**, 194–199 (2010).
DOI: 10.1016/j.matdes.2009.06.032

[33] Yasmin A., Daniel I. M.: Mechanical and thermal properties of graphite platelet/epoxy composites. Polymer, **45**, 8211–8219 (2004).
DOI: 10.1016/j.polymer.2004.09.054

[34] Miller S. G., Bauer J. L., Maryanski M. J., Heimann P. J., Barlow J. P., Gosau J-M., Allred R. E.: Characterization of epoxy functionalized graphite nanoparticles and the physical properties of epoxy matrix nanocomposites. Composites Science and Technology, **70**, 1120–1125 (2010).
DOI: 10.1016/j.compscitech.2010.02.023

[35] Kornmann X., Lindberg H., Berglund L. A.: Synthesis of epoxy–clay nanocomposites. Influence of the nature of the curing agent on structure. Polymer, **42**, 4493–4499 (2001).
DOI: 10.1016/S0032-3861(00)00801-6

[36] Lan T., Kaviratna P. D., Pinnavaia T. J.: Epoxy self-polymerization in smectite clays. Journal of Physics and Chemistry of Solids, **57**, 1005–1010 (1996).
DOI: 10.1016/0022-3697(95)00388-6

[37] Auad M. L., Nutt S. R., Pettarin V., Frontini P. M.: Synthesis and properties of epoxy-phenolic clay nanocomposites. Express Polymer Letters, **1**, 629–639 (2007).
DOI: 10.3144/expresspolymlett.2007.86

[38] Becker O., Varley R., Simon G.: Morphology, thermal relaxations and mechanical properties of layered silicate nanocomposites based upon high-functionality epoxy resins. Polymer, **43**, 4365–4373 (2002).
DOI: 10.1016/S0032-3861(02)00269-0

[39] Ratna D., Manoj N. R., Varley R., Singh Raman R. K., Simon G. P.: Clay-reinforced epoxy nanocomposites. Polymer International, **52**, 1403–1407 (2003).
DOI: 10.1002/pi.1166

[40] Kostopoulos V., Karapappas P., Loutas T., Vavouliotis A., Paipetis A., Tsotra P.: Interlaminar fracture toughness of carbon fibre-reinforced polymer laminates with nano- and micro-fillers. Strain, in press (2011).
DOI: 10.1111/j.1475-1305.2008.00612.x

[41] Kontos G. A., Soulintzis A. L., Karahaliou P. K., Psarras G. C., Georga S. N., Krontiras C. A., Pisanias M. N.: Electrical relaxation dynamics in TiO_2 – polymer matrix composites. Express Polymer Letters, **1**, 781–789 (2007).
DOI: 10.3144/expresspolymlett.2007.108

[42] Najafi E., Shin K.: Radiation resistant polymer–carbon nanotube nanocomposite thin films. Colloids and Surfaces A: Physicochemical and Engineering Aspects, **257**, 333–337 (2005).
DOI: 10.1016/j.colsurfa.2004.10.076

[43] Zhang L. C., Zarudi I., Xiao K. Q.: Novel behaviour of friction and wear of epoxy composites reinforced by carbon nanotubes. Wear, **261**, 806–811 (2006).
DOI: 10.1016/j.wear.2006.01.033

[44] Allen N. S., Edge M., Ortega A., Liauw C. M., Stratton J., McIntyre R. B.: Behaviour of nanoparticle (ultrafine) titanium dioxide pigments and stabilisers on the photooxidative stability of water based acrylic and isocyanate based acrylic coatings. Polymer Degradation and Stability, **78**, 467–478 (2002).
DOI: 10.1016/S0141-3910(02)00189-1

eXPRESS Polymer Letters Vol.5, No.3 (2011) 228–237
Available online at www.expresspolymlett.com
DOI: 10.3144/expresspolymlett.2011.22

Fabrication and mechanical properties of self-reinforced poly(ethylene terephthalate) composites

J. C. Chen[1], *C. M. Wu*[2*], *F. C. Pu*[2], *C. H. Chiu*[2]

[1]Graduate Institute of Materials Science and Technology, Vanung University, Chungli, Taiwan, ROC
[2]Department of Fiber and Composite Materials, Feng-Chia University, 100, Wenhwa Rd., Taichung, Taiwan 40724, ROC

Received 26 August 2010; accepted in revised form 14 November 2010

Abstract. Self-reinforced poly(ethylene terephthalate) (PET) composites prepared by using a modified film-stacking technique were examined in this study. The starting materials included a high tenacity PET yarn (reinforcement) and a low melting temperature biodegradable polyester resin (matrix), both of which differ in their melting temperatures with a value of 56°C. This experiment produced composite sheets at three consolidation temperatures (T_c: 215, 225, and 235°C) at a constant holding time (t_h: 6.5 min), and three holding times (3, 6.5 and 10 min) at a constant consolidation temperature of 225°C. This study observed a significant improvement in the mechanical properties obtained in self-reinforced PET composites compared to the pure polyester resin. The results of tensile, flexural, and Izod impact tests proved that optimal conditions are low consolidation temperature and short holding time. The absorbed impact energy of the best self-reinforced PET composite material was 854.0 J/m, which is 63 times that of pure polyester resin.

Keywords: *mechanical properties, processing technologies, poly(ethylene terephthalate) (PET), self-reinforced PET composites, film-stacking*

1. Introduction

The negative environmental impact of the steadily increasing use of plastic and composite materials requires the development of new combinations of materials, possibly with improved properties, but with reduced environmental harm. Consequently, the development of recycling-friendly thermoplastic composites has become a top priority. In fact, there is a growing interest to either improve the methods for recycling and reusing existing composites, or develop new and intrinsically more suitable composites. Creating all-polymeric material, especially self-reinforced polymeric composite material is an excellent alternative to traditional fiber-reinforced composites because both the reinforcing and the continuous phases involve polymers belonging to the same family of polymers [1–3]. These polymers can be entirely melted down at the end of their product life for recycling.

The self-reinforced polymeric composite material possesses many advantages and features, such as thermoformability, high stiffness, high tensile strength, outstanding impact resistance at low density, and containing no glass [2–5]. Because the reinforcement and the matrix are compatible chemically; therefore, they usually have no interfacial problems. Fiber manufactured from a highly oriented form of the same polymer matrix provides adequate reinforcing strength, resulting in a self-reinforced polymeric composite material with improved specific stiffness and specific strength, especially from the aspect of dynamic toughness and elongation at break. Additionally, the waste/scrap materials can be recycled by melting which satisfies the demand for green material.

*Corresponding author, e-mail: cmwu@fcu.edu.tw

In 1975, Capiati and Porter [6] initially developed a polyethylene/polyethylene composite and introduced the concept of self-reinforced polymeric composites. Ward and coworkers [7–11] further developed this type of composite material using the 'hot compaction' technique. Following this study, opening literatures has reported numerous studies on the preparation of self-reinforced polypropylene (PP) [8, 11–17], polyethylene terephthalate (PET) [4, 9, 18–19], polymethyl methacrylate [20], liquid crystal copolymer [21–22], polylactic acid [23], and polyamide [24–26] composites. In particular, the self-reinforced PP composites are now available on the market under the trade name Curv®, Armordon®, and Pure® [5]. Numerous products, such as automotive components, luggage, sporting goods and protective materials already apply self-reinforced PP composites.

The main challenge when producing a self-reinforced polymeric composite material is combining the fiber and matrix into one composite. Various fabrication methods such as hot compaction, overheating, co-extrusion, film stacking, and traditional melting or powder impregnation can produce the self-reinforced composite materials [2–3]. In most cases, the hot compaction process produces the self-reinforced polymeric composites; however, now Curv® uses it for production. This process occurs via the partial melting of the fibers so that the molten outer surface of the fibers becomes the matrix after cooling. However, the processing window of hot compaction is small, typically about 5°C or below between the feasible consolidation temperature and the melting temperature of the fiber. In 2006, Alcock *et al.* [17] improved the hot compaction process using a combination of constraining and co-extrusion. The processing window for creating these self-reinforced PP composites can be enlarged to approximately 20–40°C creating excellent bonding between the co-extruded two types of PP tapes of different melting temperatures. Presently manufacturers fabricate Armordon® and Pure® by applying the co-extrusion technique.

Many studies have explored the film stacking method for manufacturing self-reinforced polymeric composites [15–16, 27–29]. After producing the reinforced textile structure, it is sandwiched between films, which should overtake the role of the matrix after melting and subsequent cooling. Therefore, the reinforcing and matrix-forming polymer layers and films alternately lie on each other before producing the hot pressed consolidated composites. The advantages of the film stacking method include a wide processing window, freedom of material selection, and no expensive pre-production. The film stacking self-reinforced PP composites were the first to utilize the textile reinforcing structure [30–31].

The major problem with the aforementioned methods above for manufacturing self-reinforced polymeric composite material is damaging the reinforcement, while melting the matrix polymer during the forming process. Excessive heating results in fiber relaxation and ultimately causes the fiber to lose molecular orientation, whereas, insufficient heating leads to a poor interfacial bonding between the fiber and the matrix. Some studies successfully used a small temperature-processing window to prepare self-reinforced polymeric composites but reduce the versatility of the processing route. Therefore, materials, that maximize the difference in melting temperatures between the matrix and reinforcement polymers, are vital for forming the material, while ensuring that the reinforcement fibers remain unaffected by the consolidation temperature. Using fibers produced from the same material, but with different drawing ratios, can enlarge the processing window. Bárány, Karger-Kocsis and coworkers [14–16, 32] reported another novel approach that used the film stacking method to prepare the self-reinforced PP composites by taking the polymorphism-related difference in the melting range between the β and α phases PP. Bárány and Karger-Kocsis could enlarge the processing window for creating these self-reinforced PP composites to 25°C. Alcock etc. [33] increased the size of the processing window of self-reinforced PP composites to 40°C by exploiting the random copolymer with a lower melting temperature. All of the previously mentioned efforts have contributed to the commercialization of self-reinforced PP composites. However, PP has relatively low mechanical properties, particularly at elevated temperatures. The potential applications of self-reinforced PP composite materials are currently limited; therefore, exploring combinations of new materials and extending the processing window is critical.

In 2004, Hine and Ward researched the hot compaction technique with woven poly(ethylene terephthlate) (PET) multifilaments [9]. The results showed that hydrolytic degradation occurred rapidly at the temperatures required for successful compaction. This led to the embrittlement of the resulting materials and increased the holding time. In 2005, Rojanapitayakorn *et al.* [18] studied the effect of various hot compaction temperatures on crystallinity, molecular orientation, and mechanical properties of self-reinforced PET (srPET) composites. Yao *et al.* [19] prepared srPET composites by compressing molding laminations of thin amorphous PET films and high crystallinity PET fabrics. The results revealed that an increase in the holding time creating a reduced interfacial adhesion and mechanical properties of srPET composites because the sample becomes brittle. The authors believed that thermal and hydrolytic degradation cause the embrittlement. Therefore, in order to minimize the degradation, the hot compaction process should be performed as rapidly as possible.

Bárány, Karger-Kocsis and coworkers [14–16, 34] studied the processing parameters of self-reinforced PP composites and concluded that the consolidation temperature is more suited to control the parameter than the holding time when the consolidation pressure is invariable. The increase in the consolidation temperature caused an increase in tensile properties, but a decrease in the impact energy. An increase in the holding time did not cause any large changes in the tensile properties, whereas the impact energy slightly improved. However, Alcock *et al.* [12] reported that the unidirectional self-reinforced PP composites prepared by co-extruded technique showed little deviation in the mechanical properties from temperature consolidation. Khondker *et al.* [25] studied the mechanical properties of aramid/nylon plain knitted composites fabricated by varying the holding time. They found that the tensile strength of the reinforcing aramid fiber decreased significantly with an increasing duration of heat exposure, whereas the tensile modulus of aramid fiber was insensitive to the length of heat exposure. Therefore, tensile modulus and strength of aramid/nylon composites increase and decrease, respectively, with a longer holding time. It is evident that the mechanical properties of self-reinforced polymeric composite materials are sensitive to both consolidation temperature and holding time, depending on the characters of the constituting materials and fabrication method.

Based on the aforementioned introduction, this study is aware of the fact that the exploration of new materials combinations and ascertaining the optimal processing conditions are most critical for self-reinforced polymeric composite materials. Poly(ethylene terephthalate) (PET), a commercially available oriented polymer, has the potential to show more favorable mechanical and temperature performance than the PP fiber or tape. However, studies of srPET composite materials are limited. Therefore, in this study, biodegradable polyester was uses as matrix material and woven fabric of PET oriented homopolymer was used as reinforcement for developing srPET composite materials. The optimal processing conditions such as consolidation temperature and holding time, for this srPET composite material were investigated.

2. Experimental

2.1. Materials

In this study, biodegradable polyester (Apexa® 4024, Dupont, Japan) in the form of pellets, were used as the matrix. The measured melting point of the biodegradable polyester determined by DSC is 198°C (Figure 1). The recommended processing temperature in the guideline of the biodegradable polyester resin is approximately 215°C. The viscosity was studied by capillary rheometry (Rheo-tester 1501, Göttfert, Germany) to understand the flow and impregnation behaviors of the matrix. Figure 2 displays the viscosity behaviors of the polyester

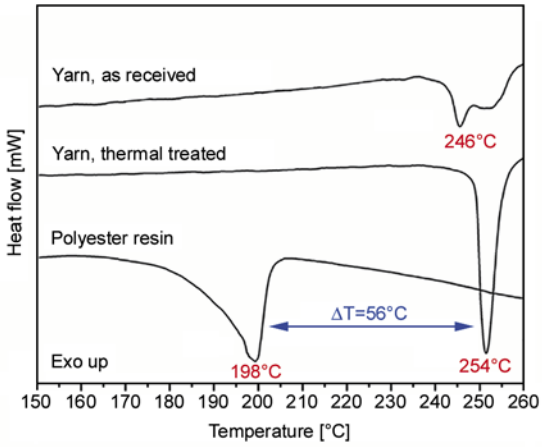

Figure 1. Thermograms of the polyester resin and the reinforcing PET yarn before and after thermal treated

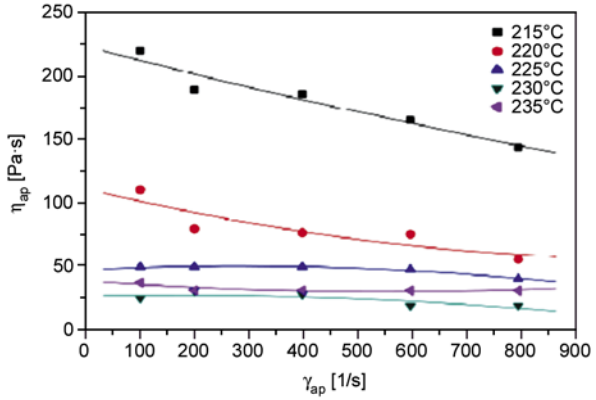

Figure 2. The viscosity behaviors of the polyester resin at testing temperatures of 215 to 235°C determined by capillary rheometry under various shear rates

resin at testing temperature of 215 to 235°C. The average viscosities measured at 215, 225 and 235°C are 180, 46 and 31 Pa·s. Such high viscosity in the polyester resin is about two orders higher than that of a conventional thermoset resin. The conventional thermosetting processing methods are thus not utilized for the polyester resin and some others must be developed.

This study used a PET plain-woven construction fabric as reinforcement. The PET yarn for high denier industrial (HDI) purpose (grade: dope dyed color yarn) was provided by Far Eastern New Century Corporation, Taiwan (www.fenc.com), consisting of 2000 denier multifilament bundles with tenacity of 7.8±0.3 g/denier and elongation of 14±2%. Every multifilament bundle consists of 182 filaments with filament diameter of 32 μm. The multifilament bundles were dope-dyed in black to imitate the appearance of carbon fabric. The PET plain-woven fabric has a fabric weight of 280 g/m^2. The warp and weft direction of the fabric (5 bundles/cm) balance reasonably well. Double melting points were obtained for the as received PET plain-woven fabric with initial melting at 246°C (Figure 1).

2.2. Sample preparation

This study presents a modified film stacking technique to produce high quality impregnated and void free srPET composites. To prevent PET fiber shrinkage and relaxation during the heat consolidating processing, the fabric was first subjected to a thermal setting for 30 min at 230°C. As shown in Figure 1, the single and sharp melting point for the thermal treated PET plain-woven fabric was obtained at 254°C. A melting temperature difference between reinforcing fiber and matrix was 56°C. At first, the matrix was prepared into a thin film form (thickness of 400 μm) using compression molding at 200°C for 3 min, at a pressure of 5 MPa. This was followed by quenching the matrix in water by covering it with Teflon films. The srPET composite lamina with average thickness of ~480 μm was prepared using the procedure: laid-up one layer of thermal treated PET fabric on PET thin film at 200°C for 1 min under a pressure of 5 MPa followed by quenching in water with the covering of Teflon films. The srPET laminates were prepared by stacking five layers of lamina at various T_c and holding times at a pressure of 10 MPa followed by slow cooling to room temperature and demolded. Three consolidation temperatures (T_c: 215, 225, and 235°C) with constant holding time (t_h: 6.5 min) and three holding times (3, 6.5 and 10 min) at constant consolidation temperature: 225°C were selected to determine the optimal processing conditions. Figure 3 shows a typical cross-section of the srPET specimen indicating a good impregnation. In this experiment, the fiber volume fractions of the srPET composites were approximately 46%.

2.3. Mechanical tests

In this study, a universal testing machine (AG-100kNX, Shimadzu, Japan) was used to perform the tensile and three-point bending flexural tests at room temperature according to ASTM D3039 and D790, respectively. Tensile specimens cut from the prepared srPET samples were 250×25×2 mm^3 in normal dimension and were clamped over an area of 50×25 mm^2 at each end leaving a gauge length of 150 mm. Aluminum tabs were glued onto the ends

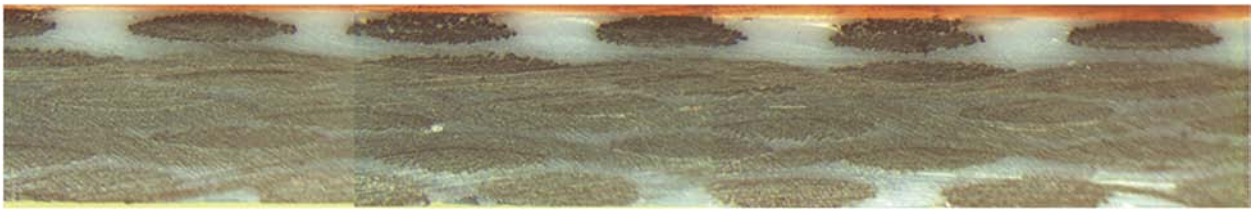

Figure 3. Light microscopic image of a srPET sample's cross section showing a good impregnation (T_c 225°C/t_h 6.5 min)

of specimen to aid gripping areas. The grip pressure was hydraulically controlled. The testing crosshead speeds were 5 mm/min for the tensile test. The axial displacement was measured by the machine according to the movement of the crosshead. Three-point bending test was conducted to evaluate the flexural properties of the srPET composites. Specimens in 100 mm long and 12 mm wide by 2 mm thick were cut from the srPET composite plates. A span length of 64 mm assured a span-to-depth ratio of 32, and a crosshead speed of 3.4 mm/min was adopted. The Izod impact test was performed at room temperature according to ASTM D256 on a pendulum impact tester (CPI, Atlas electric devices, USA) at impact energy of 5.4 J. The impact velocity used was 3.4 m/sec. The dimensions for the Izod impact specimen were 63.5×12.7×2 mm^3, and were provided with a 2.7±0.2 mm deep notch. The notches in the samples were opened by using a notch opener (QC-640, Cometech testing machines, Taiwan), and were all with a notch tip radius of 0.25 mm. All the mechanical properties reported represent the average value of five readings at least.

3. Results and discussion

3.1. Effects of consolidation temperature, T_c

Figure 4 shows the typical tensile stress-strain curves of the srPET composites at different consolidation temperatures with an identical holding time (6.5 min). The results revealed a brittle type direct failure curve for the pure polyester resin. However, the curves for all the srPET composites displayed significant yielding and post yield strain hardening, indicating the reinforcing effect and structural homogeneity for the srPET composites. The 235°C sample demonstrates a severely vibrating curve before the final catastrophic fracture. However, a relatively smooth curve was observed in the sample of 215°C. Please notice that the tensile elongation for the srPET samples of 215 and 225°C is approximately 14% which is the same as that of the PET yarn. That means the PET yarn bears most of external loads and exhibits its reinforcing effect with the aid of the protecting polyester matrix. However, premature fiber breakages were found in the srPET samples of 235°C. Due to the plain-woven interlaced structure, stress concentration occurred on the fiber bundles around the interlaced point and led to breakage of the fiber bundles. Two kinds of tensile damage exist: break-apart (Figure 5a) and split/delamination (Figure 5b), were noticed for the 215 and 235°C srPET samples, respectively. The failure modes of 215°C sample are matrix fracture, short-range delamination, and multifilament bundle breakage. As for the 235°C sample, many sub-critical failures occurred after the yield point and caused the repeated fluctuation in tensile stress. A close visual observation of the test specimens suggested that the matrix fracture and shear breakage of the multifilament bundle over the length of the specimen occurred during the failure process. When the bundle split or experienced breakage, the released fractured energy dissipated with large amounts of long-range delamination, resulting in stress vibration. The difference in tensile damages could be

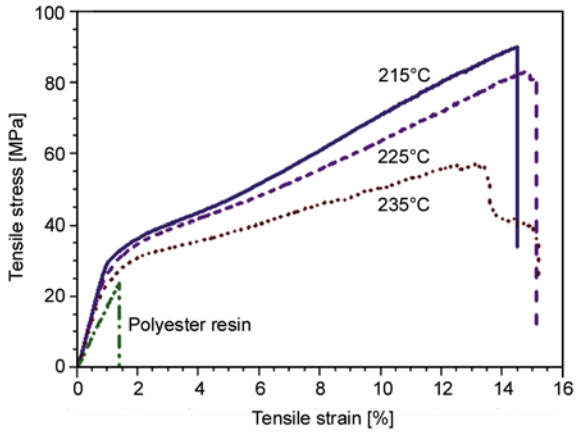

Figure 4. Typical tensile stress-strain curves of the srPET composites at different consolidation temperatures, T_c (t_h: 6.5 min)

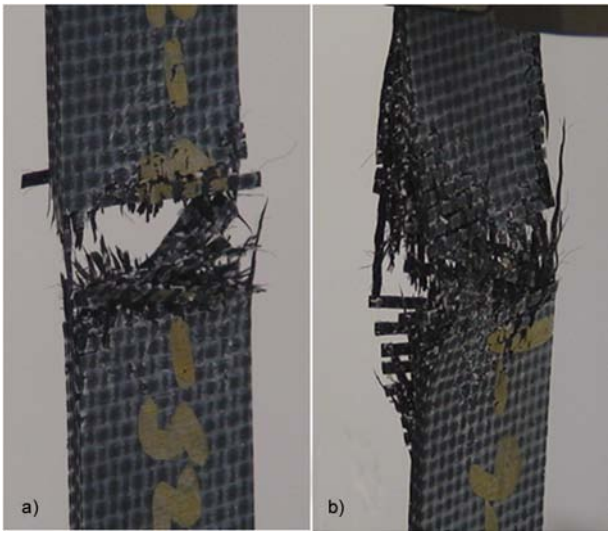

Figure 5. Typical tensile failure images for srPET composites. (a) break-apart damage for consolidation temperature, T_c 215°C srPET sample, (b) split/delamination damage for T_c 235°C SPC sample

attributed to the thermal degradation of the polyester matrix and poor interfacial adhesion at higher consolidation temperatures.

Please consider that the failure elongation for pure polyester resin is approximately 1.5%, which is near the yielding elongation for the srPET composites. This is clear evidence demonstrating the reinforcing effect of the srPET composites. The slope between the yielding to failure point (called the post-yield modulus) represents the reinforcing efficiency of the srPET composites. The post-yield modulus decreased with increasing the T_c and resulted in tensile strength debasement. This post-yield modulus and strength debasement was due to the thermal degradation of the polyester matrix and the resulting poor interfacial adhesion [8]. Therefore, Table 1 summarizes the four tensile properties: Young's modulus, tensile strength, yield strength and post-yield modulus. The srPET composites reveal a noteworthy improvement in mechanical properties compared to the polyester resin. All of the tensile properties of the srPET composites decrease when the T_c increases. The srPET composite consolidates at a low temperature of 215°C, exhibits the highest modulus of 3.32 GPa, and strength: 95.5 MPa, with 76 and 366% enhancement, respectively, when compared to the polyester resin. When the T_c elevated from 215 to 235°C, the modulus and yield strength decreased slightly from 3.32 GPa and 30.5 MPa to 3.01 GPa and 27.7 MPa, which relates to the loss of orientation of the reinforcing fibers and the degradation of the polyester matrix [35]. As for the tensile strength, it decreased from 90.9 to 60.9 MPa, which was due to the thermal degradation of the polyester resin and poor interfacial adhesion. This means that a higher T_c did not contribute to impregnation enhancement, but caused matrix thermal degradation and poor interfacial adhesion.

Table 2 summarizes the flexural and Izod impact properties of the srPET composites at different consolidation temperatures with an identical holding time (6.5 min). Similarly to the tensile results, the flexural modulus, and impact energy of the srPET composites decrease when the T_c increases. The flexural and impact properties of the srPET composites revealed a large improvement compared to those of the polyester resin. The pure polyester sample fractured at 5% flexural deflection, however, the srPET composites did not collapse within the crosshead limit. This reveals the prevention ability from crack propagation by the reinforcing woven fabric. This study did not find any visible failures in the bent srPET samples, which demonstrates its highly tough character. The srPET composite consolidates at a low temperature of 215°C and exhibits the highest flexural modulus: 3.81 GPa, and strength: 66.0 MPa, with 90 and 21% enhancement, respectively, when compared to the polyester resin. When the T_c elevates above 225°C, the flexural modulus slightly decreases to 3.49~3.63 GPa, which is still much higher than that of polyester matrix with value of 2.10 GPa. However, there is no difference in flexural strength between the srPET composites and the pure matrix material. This indicates a poor interfacial adhesion between the reinforcing fabric and matrix.

Table 2 shows the resulting notched Izod impact energy of the srPET composites, which exhibited extremely high impact absorption properties, when compared to the pure polyester resin. Unlike the impact fracture that occurred in the pure polyester sample, the srPET composites failed in a tough manner with tensile and compressive failures, and did not break apart (Figure 6). The figure revealed the prevention ability of the crack propagation by the reinforcing woven fabric. When the impactor encountered the srPET specimen, the fiber-bundle breakage occurred around the notched side first, while compressive force amassed around the other

Table 1. Tensile properties for the srPET composites produced at different consolidation temperatures

T_c [°C]/t_h [min]	Tensile modulus [GPa]	Tensile strength [MPa]	Yield strength [MPa]	Post-yield modulus [GPa]
PET*	1.87±0.06	20.5±7.1	NA	NA
215/6.5	3.32±0.06	90.9±0.6	30.5±0.6	0.49±0.02
225/6.5	3.23±0.03	85.0±3.2	28.8±2.8	0.47±0.03
235/6.5	3.01±0.13	60.9±3.2	27.7±2.3	0.32±0.02

*Pure polyester samples prepared at T_c: 200°C/t_h: 3 min

Table 2. Flexural and impact properties for the srPET composites produced at different consolidation temperatures

T_c [°C]/t_h [min]	Flexural modulus [GPa]	Flexural strength [MPa]	Impact energy [J/m]
PET*	2.01±0.10	54.6±2.7	13.5±1.6
215/6.5	3.81±0.07	66.0±0.6	715.6±82.0
225/6.5	3.63±0.08	55.8±0.8	685.9±9.1
235/6.5	3.49±0.04	55.1±0.2	493.3±78.4

*Pure polyester samples prepared at T_c: 200°C/t_h: 3 min

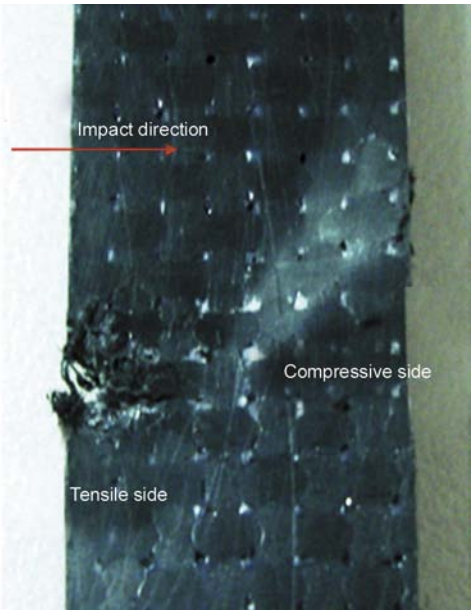

Figure 6. Photograph of the Izod impact tested srPET specimen

side of specimen. Due to the laminated nature and integrity of the woven fabric architecture, this study observed fiber bundle breakage near the notch area followed by extensive delamination along the interlaminate interface. Figure 7 shows a typical 45° compressive shearing failure occurring on the compressive side of the srPET samples that accompany the fiber breakage (kink and buckle), the matrix crush, and delaminations. The srPET composite consolidates at 215°C, elevates the impact energy from the value of 13.5 J/m for pure polyester resin to 715.6 J/m, with a 53-fold enhancement. Due to the loss orientation of reinforcing fibers and the degradation of the polyester matrix at high Tc, the impact energy decreased up to 31% when Tc increased. However, the impact energy for the 235°C sample is 493.3 J/m, which still has a 37-fold enhancement to the pure polyester resin.

3.2. Effects of holding time, t_h

Figure 8 shows the typical tensile stress-strain curves of the srPET composites at different holding times (3, 6.5, and 10 min) with T_c at 225°C. The break-apart damage (Figure 5a) was found for the 3 min sample, while the split/delamination damage as shown in Figure 5b was noticed for long holding time srPET samples: 6.5 and 10 min. It is noteworthy to check the effect of holding time on the initial modulus, post-yield modulus, and tensile strain. Little deviation of the initial modulus and post-yield modulus with holding time was evidence for samples consolidated at 225°C with comparable fiber orientation and interfacial adhesion. The tensile strain decreased with the increasing t_h. This premature failure for long holding time samples was attributed to the degradation and embrittlement of the polyester matrix [9, 19, 25]. Tensile properties: Young's modulus, tensile strength, yield strength and post-yield modulus were thus determined and summarized in Table 3. When the t_h prolonged from 3 to 10 min, the tensile strength decreased slightly

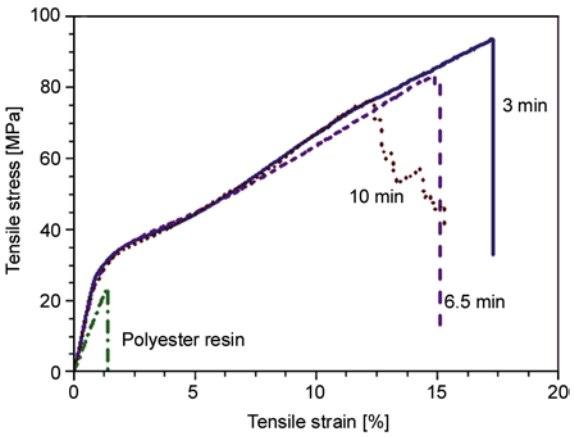

Figure 8. Typical tensile stress-strain curves of the srPET composites at different holding times, t_h (T_c: 225°C)

Figure 7. A typical 45° compressive shearing failure occurs in the compressive side of srPET composites accompany with fiber breakage, matrix crush, and delaminations

Table 3. Tensile properties for the srPET composites produced at different holding times

T_c [°C]/t_h [min]	Tensile modulus [GPa]	Tensile strength [MPa]	Yield strength [MPa]	Post-yield modulus [GPa]
PET*	1.87±0.06	20.5±7.1	NA	NA
225/3	3.30±0.08	95.5±2.7	31.1±1.5	0.42±0.04
225/6.5	3.23±0.03	85.0±3.2	28.8±2.8	0.47±0.03
225/10	3.24±0.10	77.4±2.4	29.0±2.8	0.47±0.02
215/3	3.29±0.07	119.1±5.6	31.3±1.8	0.47±0.01

*Pure polyester samples prepared at T_c: 200°C/t_h: 3 min

from 95.5 to 77.7 MPa, which relates to the degradation and embrittlement of the polyester matrix. This study shows that the best tensile strength had a value of up to 95.5 MPa when sampled at a 3 min holding time, which is a 4.7-fold enhancement over that of the pure polyester resin.

Table 4 summarizes the flexural and Izod impact properties of the srPET composites at different holding times with T_c at 225°C. A slight influence of the flexural properties with holding time was evidenced for samples consolidated at 225°C with comparable interfacial adhesion. The srPET sample with 3 min holding time, exhibited the highest flexural properties. The srPET sample with a holding time longer than 6.5 min at 225°C, exhibited the same flexural strength as pure matrix material. This caused a premature failure of the interphase due to the degradation and embrittlement of the polyester matrix.

The impact energy of the srPET composites decreased when the holding time increased, from 811.3 to 422.4 J/m at T_c 225: clear evidence that degradation and embrittlement of the polyester matrix took place at T_c above 225°C. The rapid process (t_h: 3 min) for srPET composite consolidated at 225°C elevated the impact energy from value of 13.5 (polyester matrix) to 811.3 J/m, with a 60-fold enhancement.

Table 4. Flexural and impact properties for the srPET composites produced at different holding times

T_c [°C]/t_h [min]	Flexural modulus [GPa]	Flexural strength [MPa]	Impact energy [J/m]
PET*	2.01±0.10	54.6±2.7	13.5±1.6
225/3	3.65±0.19	61.0±0.4	811.3±59.6
225/6.5	3.63±0.08	55.8±0.8	685.9±9.1
225/10	3.53±0.08	56.6±0.8	422.4±39.4
215/3	4.21±0.20	81.0±6.8	854.0±68.2

*Pure polyester samples prepared at T_c: 200°C/t_h: 3 min

To summarize the srPET composites study, the processing conditions proved to influence the mechanical properties of the srPET composites significantly, such as with consolidation temperature and holding time. This is due to the degradation and embrittlement of the polyester matrix. Optimal process conditions including a consolidation temperature of T_c: 215°C and a holding time of t_h: 3 min, were thus conceived. As revealed in Table 3, its tensile strength increases further from 95.5 to 119.1 MPa. In addition, the flexural modulus and strength improve further to 4.21 GPa and 81.0 MPa, respectively (Table 4). The impact energy for the optimal processed srPET sample elevated from value of 13.5 (polyester resin) to 854.0 J/m, with a 63-fold enhancement.

4. Conclusions

In this study srPET composites were prepared by utilizing the modified film stacking technique to laminate a thin polyester film and woven PET fabrics. Experimental results showed that the srPET composites display significant improvement in their tensile, flexural, and impact properties when compared to the non-reinforced polyester matrix. Due to the degradation and embrittlement of the polyester matrix, the mechanical properties strongly affected the consolidation temperature and holding time. The srPET composites with a low consolidation temperature at 215°C and a short holding time of 3 min displayed the best mechanical properties. The tensile strength, flexural modulus and strength were largely improved to 119.1 MPa, 4.21 GPa and 81.0 MPa. The absorbed impact energy of the best srPET composites was 854.0 J/m, which is 63 times that of pure polyester resin.

Acknowledgements

Part of this work is financially supported from the National Science Council of Taiwan, ROC, under contract number NSC 99-2632-E-035-001 -MY3.

References

[1] Pegoretti A.: Trends in composite materials: The challenge of single-polymer composites. Express Polymer Letters, **1**, 710 (2007).
DOI: 10.3144/expresspolymlett.2007.97

[2] Matabola K. P., DeVries A. R., Moolman F. S., Luyt A. S.: Single polymer composites: A review. Journal of Materials Science, **44**, 6213–6222 (2009). DOI: 10.1007/s10853-009-3792-1

[3] Kmetty Á., Bárány T., Karger-Kocsis J.: Self-reinforced polymeric materials: A review. Progress in Polymer Science, **35**, 1288–1310 (2010). DOI: 10.1016/j.progpolymsci.2010.07.002

[4] Fakirov S., Duhovic M., Maitrot P., Bhattacharyya D.: From PET nanofibrils to nanofibrillar single-polymer composites. Macromolecular Materials and Engineering, **295**, 515–518 (2010). DOI: 10.1002/mame.200900387

[5] Morgan L. M., Weager B. M., Hare C. M., Bishop G. R., Smith G. M.: Self reinforced polymer composites: Coming of age. in 'Proceeding of the 17th International Conference on Composite Materials, Edinburgh, UK' ID12:15 (2009).

[6] Capiati N. J., Porter R. S.: The concept of one polymer composites modelled with high density polyethylene. Journal of Materials Science, **10**, 1671–1677 (1975). DOI: 10.1007/BF00554928

[7] Hine P. J., Ward I. M., Maaty M. I. A., Olley R. H., Basset D. C.: The hot compaction of 2-dimensional woven melt spun high modulus polyethylene fibers. Journal of Materials Science, **35**, 5091–5099 (2000). DOI: 10.1023/A:1004835816735

[8] Hine P. J., Ward I. M., Jordan N. D., Olley R. H., Basset D. C.: The hot compaction behaviour of woven oriented polypropylene fibres and tapes. I. Mechanical properties. Polymer, **44**, 1117–1131 (2003). DOI: 10.1016/S0032-3861(02)00809-1

[9] Hine P. J., Ward I. M.: Hot compaction of woven poly(ethylene terephthalate) multifilaments. Journal of Applied Polymer Science, **91**, 2223–2233 (2004). DOI: 10.1002/app.13343

[10] Ward I. M., Hine P. J.: The science and technology of hot compaction. Polymer, **45**, 1413–1427 (2004). DOI: 10.1016/j.polymer.2003.11.050

[11] Hine P. J., Olley R. H., Ward I. M.: The use of interleaved films for optimising the production and properties of hot compacted, self reinforced polymer composites. Composites Science and Technology, **68**, 1413–1421 (2008). DOI: 10.1016/j.compscitech.2007.11.003

[12] Alcock B., Cabrera N. O., Barkoula N-M., Loos J., Peijs T.: The mechanical properties of unidirectional all-polypropylene composites. Composites Part A: Applied Science and Manufacturing, **37**, 716–726 (2006). DOI: 10.1016/j.compositesa.2005.07.002

[13] Khondker O. A., Yang X., Usui N., Hamada H.: Mechanical properties of textile-inserted PP/PP knitted composites using inject-compression molding. Composites Part A: Applied Science and Manufacturing, **37**, 2285–2299 (2006). DOI: 10.1016/j.compositesa.2005.12.032

[14] Abraham T., Banik K., Karger-Kocsis J.: All-PP composites (Pure®) with unidirectional and cross-ply layups: Dynamic mechanical thermal analysis. Express Polymer Letters, **1**, 519–526 (2007). DOI: 10.3144/expresspolymlett.2007.74

[15] Bárány T., Karger-Kocsis J., Czigány T.: Development and characterization of self-reinforced poly(propylene) composites: Carded mat reinforcement. Polymers for Advanced Technologies, **17**, 818–824 (2006). DOI: 10.1002/pat.813

[16] Izer A., Bárány T.: Effect of consolidation on the flexural creep behaviour of all-polypropylene composite. Express Polymer Letters, **4**, 210–216 (2010). DOI: 10.3144/expresspolymlett.2010.27

[17] Alcock B., Cabrera N. O., Barkoula N-M., Loos J., Peijs T.: The mechanical properties of unidirectional all-polypropylene composites. Composites Part A: Applied Science and Manufacturing, **37**, 716–726 (2006). DOI: 10.1016/j.compositesa.2005.07.002

[18] Rojanapitayakorn P., Mather P. T., Goldberg A. J., Weiss R. A.: Optical transparent self-reinforced poly (ethylene terephthalate) composites: Molecular orientation and mechanical properties. Polymer, **46**, 761–773 (2005). DOI: 10.1016/j.polymer.2004.11.032

[19] Yao D., Li R., Nagarajan P.: Single-polymer composites based on slowly crystallizing polymers. Polymer Engineering and Science, **46**, 1223–1230 (2006). DOI: 10.1002/pen.20583

[20] Wright D. D., Lautenschlager E. P., Gilbert J. L.: Bending and fracture toughness of woven self-reinforced composite poly(methyl methacrylate). Journal of Biomedical Materials Research, **36**, 441–453 (1997). DOI: 10.1002/(SICI)1097-4636(19970915)36:4<441::AID-JBM2>3.0.CO;2-E

[21] Pegoretti A., Zanolli A., Migliaresi C.: Flexural and interlaminar mechanical properties of unidirectional liquid crystalline single-polymer composites. Composites Science and Technology, **66**, 1953–1962 (2006). DOI: 10.1016/j.compscitech.2006.01.015

[22] Pegoretti A., Zanolli A., Migliaresi C.: Preparation and tensile mechanical properties of unidirectional liquid crystalline single-polymer composites. Composites Science and Technology, **66**, 1970–1979 (2006). DOI: 10.1016/j.compscitech.2006.01.012

[23] Li R., Yao D.: Preparation of single poly(lactic acid) composites. Journal of Applied Polymer Science, **107**, 2909–2916 (2008). DOI: 10.1002/app.27406

[24] Bhattacharyya D., Maitrot P., Fakirov S.: Polyamide 6 single polymer composites. Express Polymer Letters, **3**, 525–532 (2009). DOI: 10.3144/expresspolymlett.2009.65

[25] Khondker O. A., Fukui T., Inoda M., Nakai A., Hamada H.: Fabrication and mechanical properties of aramid/nylon plain knitted composites. Composites Part A: Applied Science and Manufacturing, **35**, 1195–1205 (2004).
DOI: 10.1016/j.compositesa.2004.03.004

[26] Hine P. J., Ward I. M.: Hot compaction of woven nylon 6,6 multifilaments. Journal of Applied Polymer Science, **101**, 991–997 (2006).
DOI: 10.1002/app.22771

[27] Teishev A., Incardona S., Migliaresi C., Marom G.: Polyethylene fibers-polyethylene matrix composites: Preparation and physical properties. Journal of Applied Polymer Science, **50**, 503–512 (1993).
DOI: 10.1002/app.1993.070500314

[28] Marais C., Feillard P.: Manufacturing and mechanical characterization of unidirectional polyethylene-fibre/polyethylene-matrix composites. Composites Science and Technology, **45**, 247–255 (1992).
DOI: 10.1016/0266-3538(92)90086-I

[29] Houshyar S., Shanks R. A., Hodzic A.: The effect of fiber concentration on mechanical and thermal properties of fiber-reinforced polypropylene composites. Journal of Applied Polymer Science, **96**, 2260–2272 (2005).
DOI: 10.1002/app.20874

[30] Houshyar S., Shanks R. A.: Tensile properties and creep response of polypropylene fibre composites with variation of fibre diameter. Polymer International, **53**, 1752–1759 (2004).
DOI: 10.1002/pi.1569

[31] Houshyar S., Shanks R. A., Hodzic A.: Influence of different woven geometry in poly(propylene) woven composites. Macromolecular Materials and Engineering, **290**, 45–52 (2005).
DOI: 10.1002/mame.200400158

[32] Bárány T., Izer A., Karger-Kocsis J.: Impact resistance of all-polypropylene composites composed of alpha and beta modifications. Polymer Testing, **28**, 176–182 (2009).
DOI: 10.1016/j.polymertesting.2008.11.011

[33] Alcock B., Cabrera N. O., Barkoula N-M., Spoelstra A. B., Loos J., Peijs T.: The mechanical properties of woven tape all-polypropylene composites. Composites Part A: Applied Science and Manufacturing, **38**, 147–161 (2007).
DOI: 10.1016/j.compositesa.2006.01.003

[34] Bárány T., Izer A., Czigány T.: On consolidation of self-reinforced polypropylene composites. Plastics, Rubber and Composites, **35**, 375–379 (2006).
DOI: 10.1179/174328906X128234

[35] Alcock B., Cabrera N. O., Barkoula N. M., Peijs T.: The effect of processing conditions on the mechanical properties and thermal stability of highly oriented PP tapes. European Polymer Journal, **45**, 2878–2894 (2009).
DOI: 10.1016/j.eurpolymj.2009.06.025

eXPRESS Polymer Letters Vol.5, No.3 (2011) 238–245
Available online at www.expresspolymlett.com
DOI: 10.3144/expresspolymlett.2011.23

Investigation on interlaminar shear strength properties of disc laser machined consolidated CF-PPS laminates

P. Jaeschke[1*], *M. Kern*[1], *U. Stute*[1], *H. Haferkamp*[1], *C. Peters*[2], *A. S. Herrmann*[2]

[1]Laser Zentrum Hannover e. V., Hollerithallee 8, 30419 Hannover, Germany
[2]Faserinstitut Bremen e.V., Am Biologischen Garten 2, 28359 Bremen, Germany

Received 17 September 2010; accepted in revised form 8 December 2010

Abstract. In consequence of an increased interest in using endless carbon fibre reinforced thermoplastic composites (TPC), automated and highly productive processing technologies for cutting and trimming steps of consolidated materials are sought. In this paper, the influence on the thermal effect caused by laser cutting with respect to static strength properties of TPC based on a polyphenylene sulfide (PPS) matrix is studied. For the cutting experiments, consolidated TPC laminates at varying thicknesses up to s = 3.1 mm and a disc laser emitting at a wavelength of λ = 1030 nm at a maximum output power of P_L = 2 kW are used. For the first time, the resulting magnitude of the heat affected zone (HAZ) at the cutting edge of the composite material is correlated with interlaminar shear strength tests. The results are compared to specimens prepared by milling and abrasive water jet cutting. Depending on the laminate thickness, the laser treated TPC samples show comparable properties to those of conventionally processed specimens. A reduced load bearing area, as a consequence of damaged fibre-matrix-adhesion due to laser impact, is identified as main factor for the reduction of interlaminar shear strengths for higher laminate thicknesses.

Keywords: *polymer composites, processing technologies, mechanical properties, laser processing*

1. Introduction

Endless carbon and glass fibre reinforced composite structures (CFRP, GFRP) are recognized as having the greatest lightweight construction potential of all materials. Hence, CFRP and GFRP are representing significant materials for all branches of the industry where large masses have to be moved or weight has to be saved. Besides the field of mobility, including the aircraft, the automotive, the marine and the railway sector, the need of components based on fibre reinforced composites is particularly increasing within the field of energy, e.g. wind turbines, heavy-duty pipeline elements for off-shore applications and electronics, as well as within the field of sports and leisure.

In particular CFRP is characterized by high stiffness and strength, excellent corrosion resistance as well as high static and dynamic loading. An outstanding property of CFRP can be found within the potential of significant weight reduction compared to metallic materials, e.g. up to 30% for aluminium. Thus, in order to contribute significantly to energy and CO_2 savings by use of intelligent light weight constructions within the mobility sector as well as to supply optimized manufacturing processes, the use of CFRP will play an increasing role.

Although thermoset polymers mainly based on epoxy resins are representing the predominant kind of CFRP matrix materials, reinforced composites on the basis of thermoplastic polymers (TPC) are of rising interest for a quick and reliable component formability manufacture process. The potential of TPC parts inside the forming process is the ability of *in-situ* consolidation in just one process step.

*Corresponding author, e-mail: p.jaeschke@lzh.de

Thermoplastics offer several benefits such as uncritical and unlimited storage time, a better impact tolerance compared to thermoset matrices, a good ultimate strain performance, reduced crack propagation, excellent chemical resistance and quick forming process ability. They are recyclable and customized laminates and matrices are available within a wide range. The most significant advantage over thermoset based composites is their weldability [1–5].

A today's barrier for a comprehensive dissemination of TPC structures is the lack of economic, quick and reliable component manufacture processes. To overcome this deficit, fully-automated process chains for the manufacturing and assembly of thermoplastic composites have to be developed in order to achieve production rates and cycle times (<1 min) required by automotive and aircraft industry as well as the civil engineering sector [6, 7]. Integrated process cells can be adapted to specific material requirements and to new process elements including laser based techniques for cutting applications [8–10].

Today, different cutting techniques like milling or water jet cutting are used, revealing respective advantages and disadvantages [11–14]. Laser cutting using high power laser sources offers many advantages, such as no tool wear, no water or moisture uptake and highest feed rates. However, the high temperatures reached within the cutting zone could damage the structural properties of the material.

In [15–17] the authors describe the interaction between the laser radiation at different wavelengths and several polymeric materials, comprising unreinforced plastics as well as short and long fibre reinforced composites. As reinforcements, carbon, aramid and glass fibres have been used. In these publications, the focus is mainly put on the investigation of the influence of the applied laser parameters on the resulting cut quality of the respective polymeric material. Therefore, e. g. kerf geometry, roughness, dimension of the burr and global extent of the heat influenced zone have been analyzed.

The aim of this paper is to analyze the influence of the laser impact on TPC laminates with respect to the cohesion from matrix to fibre inside the heat affected zone. In this context, interlaminar shear strength tests are performed. The results are compared to those of conventionally treated samples.

2. Experimental set-up

2.1. Material characterization

The endless carbon fibre reinforced plastic used within the frame of the investigations is a semicrystalline polyphenylene sulfide (PPS) thermoplastic composite based on high tenacity (HT) fibers. The laminates (consolidated Cetex® plates, provided by TenCate Advanced Composites bv, The Netherlands) consist of harness satin carbon weaves in 0°/90° fiber orientations $[0/90]_n$. The fiber volume content is V_G = 50% with a mass per unit area of Q_C = 285 g/m^2. The material offers outstanding toughness and excellent chemical and solvent resistance. It is inherently flame resistant with low smoke emission. The cutting experiments presented here were performed using four different laminate thicknesses which are summarized in Table 1. In Figure 1, the fabric structure of the TPC material as schematic drawing as well as a real surface in conjunction with cross sections is shown.

Table 1. Classification of TPC material

Laminate thickness	*s*	[mm]	0.93	1.24	2.17	3.10
Number of layer	*n*	[–]	3	4	7	10

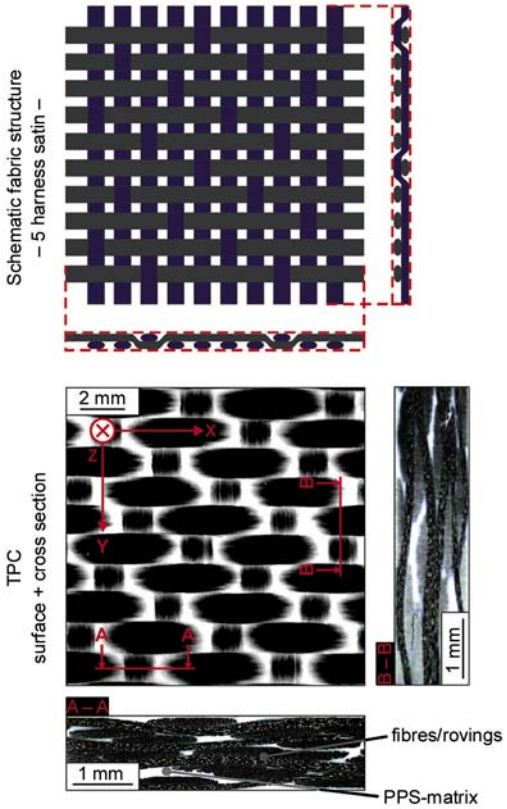

Figure 1. Fabric structure, surface and cross sections of thermoplastic composite laminate in 0°/90° plate lay-up

2.2. Laser source and cutting configuration

The cutting experiments were performed using a disc laser (HLD 3001.5, Trumpf Laser GmbH + Co. KG, Schramberg, Germany) emitting at a wavelength of λ = 1030 nm. The laser radiation is guided by an optical fibre with a diameter of d_{opt} = 150 µm to a laser working head, which focuses the laser beam inside the work piece. The adapted cutting head is based on main components provided by Rofin-Sinar Laser GmbH, Hamburg, Germany. Using a focusing lens with a focal length of f = 200 mm, a laser beam focus of d_f = 150 µm is generated. The laser provides an output power of P_L = 2 kW. As process gas, N_2 at a working pressure of p_{N_2} = 0.9 MPa was applied. The cutting process was realized by moving the TPC specimen relative to the laser working head using a linear axis (PS01-37×240, NTI AG – LinMot & MagSpring, Spreitenbach, Switzerland).

The choice of the applied laser parameter settings will certainly affect the cut quality achieved, and therefore will also affect the static strength of the TPC specimens. To exclude the influence of imperfect cutting parameters and to achieve comparable results to other cutting technologies, optimum parameters were found by parameter variation and then applying them to manufacture the test specimens. The cut quality was rated according to the following criteria: constant laser power independent on the laminate thickness, small kerf width and high optical quality (e.g., little charring). For each material thickness, the maximum feed rate allowing a reliable cutting result was determined, resulting in a specific energy per unit length E_s. The relation between E_s, the laser power P_L and the feed rate v_f is given in Equation (1):

$$E_s = \frac{P_L}{v_f} \tag{1}$$

After identification of the appropriate processing parameters the following dependency between the energy per unit length E_s as well as the number of layers n and the laminate thickness s, respectively, was found (Figure 2).

In Figure 2, a linear dependency between E_s and n becomes apparent. Therefore, an adapted increase of the applied energy in accordance with the laminate thickness is guaranteed.

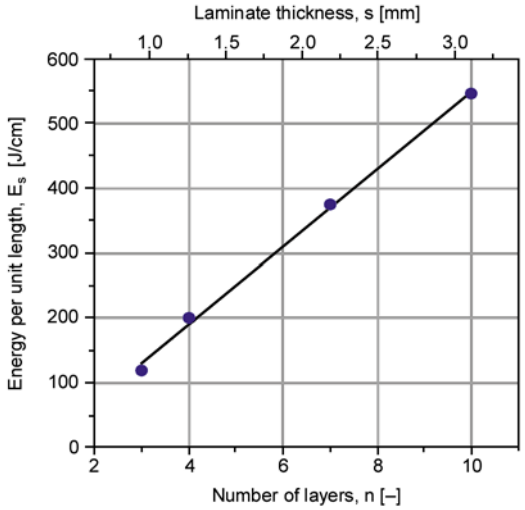

Figure 2. Applied energy per unit length of laser cutting experiments for different TPC laminate thicknesses

2.3. Material testing

Interlaminar shear strength tests according to DIN EN 2563 were performed. For reasons of comparison, reference specimens were prepared by milling as well as by abrasive water jet cutting. The milled specimens were manufactured using an FP4 Dialog 11 by DMG, Muenchen, Germany. The water jet equipment consists of a waterknife pump by Flow Europe GmbH, Bretten, Germany in conjunction with a cutting head of BHDT GmbH, Kapfenberg, Austria. Within the frame of the cutting process, garnet sand of Mesh 80 by GMA GARNET (Europe) GmbH, Hamburg, Germany was used.

The specified test method evaluates the quality of the fiber-matrix-adhesion. Therewith, the maximum shear stress of each individual specimen at the moment of the first failure is calculated. First failure occurs if the specimen fails in shear approximately in the neutral axis.

For each thickness of the TPC laminate, specimens at a length of l_0 = 20 mm and a width of b_0 = 10 mm were prepared. The length of the specimen is parallel to the warp direction of the fabrics. The rectangular specimen is positioned perpendicular and tested of flexure on two supports with a radius of r_t = 3 mm and a distance of l_t = 10 mm between them. The load is applied at the center of the specimen by means of a loading nose with a same radius r at a constant displacement rate of v_t = 1 mm/min until the moment of first failure. The corresponding bending strain is measured simultaneously.

The bending tests were performed using a universal test machine Zwick Z250 providing an accuracy of 1% of the load range in conjunction with a control software Test XPert 11.0, which records the load applied as a function of displacement of the loading nose. The tested specimens were inspected by preparation of optical micrographs in order to make sure that only interlaminar failure occurred, so fibre breakage has no influence on the bending results. In this case the interlaminar shear strength can be calculated according to DIN EN 2563.

Each test result was verified by testing seven identical specimens. All tests were performed at standard atmosphere with 23°C and 50% humidity. In order to visualize the cutting zone, optical micrographs were prepared.

3. Results and discussion

In the following, the quality of the laser cuts achieved is discussed and compared to the cut quality of conventional machining with a special emphasis on the extent of the thermal damage to the TPC. The results from the static interlaminar shear tests are given and correlated with the cut qualities identified.

3.1. Achievable cut quality

As expected, milling as well as abrasive water jet cutting produces cuts of high optical quality. No delamination or free fibre ends were observed. The laser cut samples clearly show an extended heat affected zone starting from the cutting kerf into the thermoplastic composite with changed material properties, visible by varying light reflections. In Figure 3, a cross section of a TPC disc laser cut generated using a laser output power of P_L = 2 kW for an n = 10 layer arrangement with a thickness of s = 3.1 mm is shown.

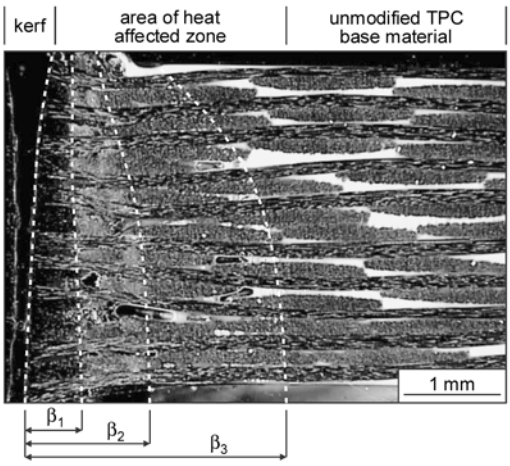

Figure 3. Optical micrograph (cross section) of laser cut TPC specimen for an n = 10 layer arrangement and characteristic regions within the heat affected zone identified

Different areas within the HAZ have been identified, in which the material damage occurs in a different manner. The induced temperature gradient, arising from the high thermal conductivity of the HT-fibres along the fibre axis (λ_c = 17 W/(m·K)) and starting at the cutting kerf towards the inner bulk material, influences the composition of the thermoplastic matrix system. Close to the cutting edge, damaged areas are detected between the single carbon fibre fabrics (interlaminar) as well as within the rovings themselves. In this zone, the PPS matrix is vaporized and the carbon fibres are charred (β_1). Adjacent to this area, it is supposed that mainly matrix damage occurs due to exceeding the decomposition temperature of T_V = 370°C for PPS (β_2). An in-situ determination of the process temperature within the composite has not been realized. With increasing distance to the cutting edge, pure interlaminar effects, i.e. structural modification within the PPS matrix depots between the carbon fibre rovings, become visible. Porosities are detected within the polymer matrix, whereas the carbon fibre fabric remains intact (β_3). The inclusion of pores within TPC laminate structures is well known from the thermoforming process of such materials, in case of applying insufficient molding pressures during the consolidation phase. In this context, the pores are generated due to mechanical inclusion of air after reaching the PPS melting temperature of T_m = 285°C. Therefore, it can be stated that the intersection between HAZ and unmodified bulk material is determined by re-solidification of the polymeric PPS matrix.

A quantitative analysis of the laser cut specimens revealed an increase of the HAZ with increasing material thickness at constant P_L. In Figure 4, the extensions of the different areas identified within the HAZ are presented for all 4 layer arrangements. For the evaluation of the respective HAZ area β_k, $k \in \{1, 2, 3\}$, the micrographs were separated into 3 horizontal sectors, which were measured independently of each other, providing a mean value for each material thickness.

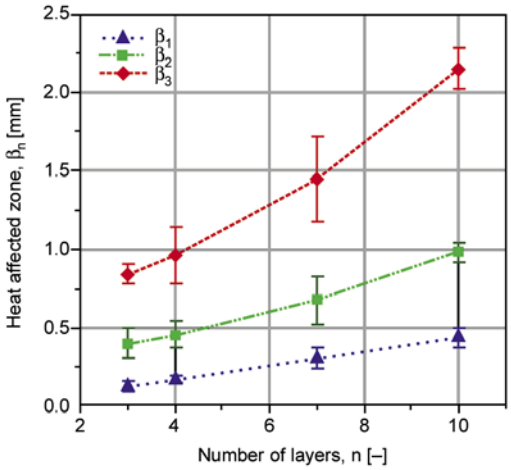

Figure 4. Different regions of the heat affected zone as a function of material thickness

3.2. Interlaminar shear strength tests

In order to investigate the influence of the resulting HAZ during laser cutting of TPC on the material properties, interlaminar shear stress measurements were performed. For all composite thicknesses, seven specimens were tested. As reference for the laser cut samples, additional specimens were prepared by milling as well as abrasive water jet cutting technique. The corresponding results of the interlaminar shear strength investigations are shown in Figure 5. The mean values and the respective standard deviations are indicated. For a better overview, within Figure 5 as well as within all following figures, the determined measuring values are spread around the respective center number of layer. All measurements were performed for n = 3, 4, 7 and 10 layers.

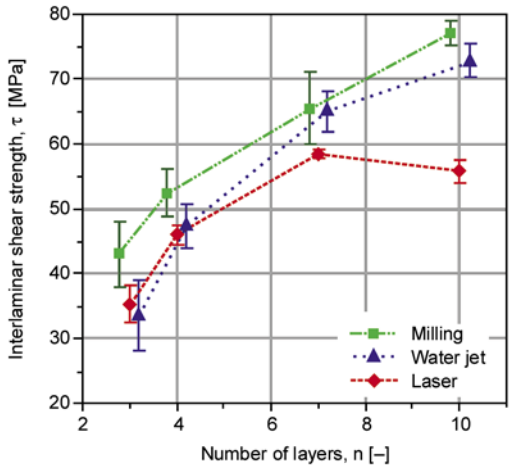

Figure 5. Interlaminar shear strength for different processing technologies as a function of laminate thickness

Overall, an increase of the interlaminar shear strength τ with increasing thickness of the TPC laminate becomes obvious. Since τ depends on the size of the load bearing area which is determined by the width and the thickness of a respective specimen, this measuring value is no material constant but mainly used for comparative investigations. In this case τ is used for a comparison of laser and conventionally treated specimens. The highest interlaminar shear strengths τ are observed for milled specimens. For laminate arrangements consisting of 3 and 4 layers, abrasive water jet and laser machined specimens reveal interlaminar shear strengths on a similar level. With increasing material thickness, the measured interlaminar shear strengths of laser cut specimens decreases in terms of the curve progression of the water jet treated samples.

In Figure 6, the corresponding bending strains ε for tested specimens generated with all 3 cutting techniques are shown. The values of milled as well as abrasive water jet machined specimens reveal a comparatively constant behaviour, independent on the material thickness. In contrast, for laser cut CF PPS, the bending strain significantly increases with increasing number of layers. A linear relation between ε and n becomes apparent. Overall, the laser processed specimens show higher bending elongations compared to conventionally treated samples.

In order to analyze the reduction of the interlaminar shear strength in case of laser treatment, the differences in τ with respect to milling and abrasive water jet machining are calculated. In Figure 7, these differences $\Delta\tau$ are plotted against the number of layers

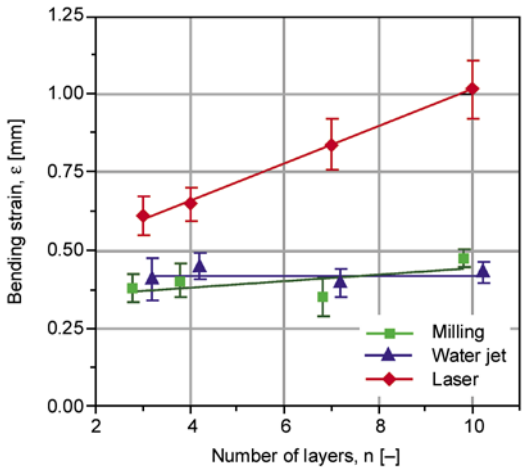

Figure 6. Bending strain for different processing technologies as a function of laminate thickness

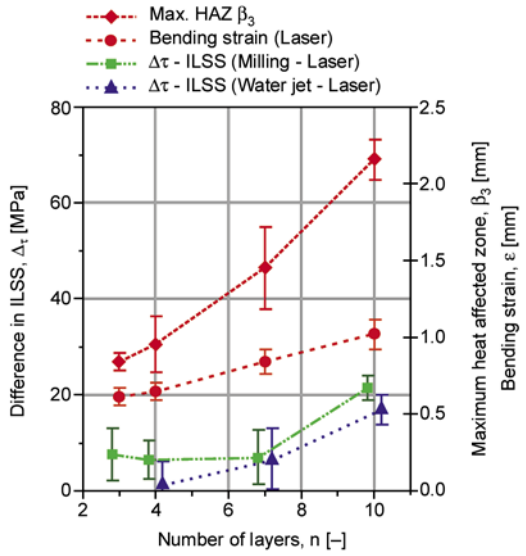

Figure 7. Bending strain and maximum extent of HAZ of laser processed specimens as well as differences in interlaminar shear strength between laser and conventionally treated CF PPS as a function of laminate thickness

n. Additionally, the bending strain ε as well as the maximum extent of the heat affected zone β_3 are added into the graph. Two main aspects can be drawn from the data. Firstly, with increasing extent of the heat affected zone, the measured bending strain increases as well. Secondly, the progression of the bending elongation of laser processed TPC specimens is directly mirrored in the difference curves of the interlaminar shear strengths $\Delta\tau$. Obviously, the larger the influence of the thermal cutting process on the material properties of the composite laminate, the lower the interlaminar shear strength and the higher the measured corresponding bending strain.

Taking into account the resulting heat affected zone due to laser impact, it is assumed that the HAZ partially reduces the load bearing area of the material as a consequence of missing or reduced fibre-matrix-adhesion at the edges of the specimens. As a result of this, the effective width of the laser cut specimens within the bending test is smaller compared to those of the conventionally machined samples. Correspondingly, the bending strain ε increases in case of laser cut TPC.

For bending tests, the interlaminar shear strength τ_0 can be derived from Equation (2), where F_{max} is the maximum bending force applied at the respective failure of the sample, s the thickness and b_0 the width of the test specimen.

$$\tau_0 = \frac{3 \cdot F_{max}}{4 \cdot s \cdot b_0} \tag{2}$$

Considering the formation of a heat influenced zone at the edges of the specimen in case of laser treatment, Equation (2) can be expressed as Equation (3):

$$\tau_{eff} = \frac{3 \cdot F_{max}}{4 \cdot s \cdot b_{eff}} \tag{3}$$

comprising an actual interlaminar shear strength τ_{eff} and an adapted specimen width b_{eff}, which is a function of the extent of the HAZ. Therefore, b_{eff} can be formulated as Equation (4):

$$b_{eff} = b_0 - 2 \cdot \beta_k \quad \text{with } k \in \{1, 2, 3\} \tag{4}$$

Using Equation (3) and (4), actual interlaminar shear strengths were calculated in consideration of β_k, which were derived from cross sections analogue to the approach presented in Figure 3 and for which the corresponding mean values are given in Figure 4. In Figure 8, the resulting curve progressions for τ_0 as well as for τ_{eff} for the areas β_1 and β_2 of the HAZ at varying laminate thickness are shown. In accordance with the prediction with respect to a reduced load bearing area as a consequence of laser impact, a significant increase of τ_{eff} especially for higher n, corresponding to a higher degree of material damage becomes apparent. In relation to the interlaminar shear strengths achieved for conventionally processed specimens (Figure 5), it can be stated that $\tau_{eff}(\beta_2)$ is found on a same level. Solely, for the n = 10 layer laminate, $\tau_{eff}(\beta_2)$ still declines

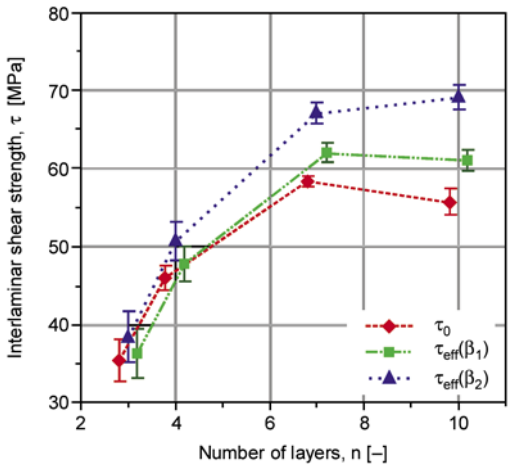

Figure 8. Progression of actual interlaminar shear strength for laser machined specimens as a function of laminate thickness

to values of approx. $\tau_{eff} = 70$ MPa, which is still lower than milled or water jet treated samples.

Since τ_{eff} (β_2) already reaches the range of achievable interlaminar shear strengths provided by conventional cutting processes, β_2 of the HAZ as crucial value determining the degree of decreased load bearing area is deduced. It can be stated that the area of re-solidified polymeric PPS matrix of the HAZ ($\Delta\beta_{32} = \beta_3 - \beta_2$) marginally influences the load transmission during the bending test. This is applicable for thin laminates, $n \leq 7$ layers, whereas for thicker composite structures, a trend towards a deeper interlaminar damage due to laser impact in conjunction with extensive heat conduction is found. However, even for $n = 10$, τ_{eff} (β_3) provides interlaminar shear strengths far above the curves of milling as well as abrasive water jet processed samples, for which reason the corresponding data for β_3 is excluded in Figure 8. Overall, the use of high power laser cutting technique is of special interest in case of thin composite laminates, for which this technique is most applicable.

4. Conslusions

Within this paper, investigations on whether thermal damage by high power laser processing reduces the interlaminar shear strength properties of endless carbon fibre reinforced thermoplastic composite materials are given. To achieve this, test specimens were cut from semicrystalline polyphenylene sulfide composite laminates based on HT fibres in harness satin carbon fabrics in $[0/90]_n$ fiber orientations with a thickness of 0.93 to 3.1 mm. The following conclusions can be drawn from the investigations:

1. For laser machined specimens, a heat affected zone (HAZ) starting at the cutting edge can clearly be detected. A quantitative analysis of the laser cut specimens revealed an increase of the HAZ with increasing material thickness at constant laser output power. The HAZ is classified into three areas, in which the material damage occurs in a different manner.
2. Interlaminar shear strength tests reveal a reduction of the maximum shear stresses for laser cut specimens compared to conventionally treated samples, provided by milling as well as abrasive water jet technique. Within the laser working range, an increase of the achievable shear strengths for a distinct material thickness with decreasing extent of the HAZ is found. Therefore, for comparably thin laminate arrangements, interlaminar shear strengths of laser machined specimens converge to those of conventionally treated TPC samples.
3. The corresponding bending strains reveal a comparatively constant behaviour for conventionally processed specimens, independent on the material thickness. In contrast, for laser cut CF PPS, the bending strain significantly increases with increasing material thickness and caused lower *E*-modulus. For specified loading conditions, e.g. about impacts, the laser processed specimens show higher bending elongations compared to conventionally treated samples.
4. Taking into account the different areas of the HAZ, actual interlaminar shear strengths for laser treated specimens have been calculated. A reduced load bearing area has been identified as main factor for the reduction of interlaminar shear strengths achieved.

Acknowledgements

The authors would like to thank the German Research Foundation (DFG) for their support within the project HA 1213/74 1. Furthermore, the authors would like to thank Dr. A. Schenk of the Water Jet Laboratory Hanover for kindly machining the reference specimens by abrasive water jet cutting. Finally the authors would like to express their gratitude to TenCate Advanced Composites bv, The Netherlands, for the supply of the consolidated Cetex® PPS composite laminates.

References

[1] Jaeschke P., Herzog D., Kern M., Erciyas A. S., Peters C., Purol H., Herrmann A. S.: Laser transmission welding of thermoplastic composites – Fundamental investigations into the influence of the carbon fibre reinforcement and orientation on the weld formation. Joining Plastics, **4**, 247–255 (2009).

[2] Jaeschke P., Herzog D., Hustedt M.: Thermography aids development of laser transmission welding. Plastics Engineering, **7**, 28–34 (2009).

[3] Offringa A.: Thermoplastics in aerospace, a stepping stone approach. in 'Proceedings of 1st Cetex Conference. Delft, Netherlands' 1–13 (2006).

[4] Kelly G.: Joining of carbon fibre reinforced plastics for automotive applications. PhD Thesis, Royal Institute of Technology, Stockholm, Sweden (2004).

[5] van Wijngaarden M. J.: Robotic induction welding of carbon fiber reinforced thermoplastics. In 'Proceedings of 1st Cetex Conference. Delft, The Netherlands' 149–160 (2006).

[6] Purol H., Peters C., Herrmann A. S.: Fast manufacturing of thermoplastic parts and challenges for a fully-automated process chain. in 'International Conference on Applied Production Technology. Bremen, Germany' 53–58 (2007).

[7] Peters C., Purol H., Herrmann A. S.: Integrated thermoforming process for CFRP-parts mass production. in 'Japan International SAMPE Technical Seminar. Kyoto, Japan' Paper No. 8 (2008).

[8] Herzog D., Jaeschke P., Meier O., Haferkamp H.: Investigations on the thermal effect caused by laser cutting with respect to static strength of CFRP. International Journal of Machine Tools and Manufacture, **48**, 1464–1473 (2008).
DOI: 10.1016/j.ijmachtools.2008.04.007

[9] Jaeschke P., Herzog D., Noelke C., Henning B., Haferkamp H.: Investigations into the sealing of heat damaged areas by applying polymer powders during laser cutting of carbon fiber reinforced composites. Advanced Engineering Materials, **12**, 587–590 (2009).
DOI: 10.1002/adem.200900310

[10] Jaeschke P., Hustedt M., Herzog D.: Ablation of cured prepreg laminates using laser pulsed water jets. in 'Proceedings of 15th International Conference on Composite Structures. Porto, Portugal' Paper No. 344 (2009).

[11] Koplev A., Lystrup A., Vorm T.: The cutting process, chips, and cutting forces in machining CFRP. Composites, **14**, 371–376 (1983).
DOI: 10.1016/0010-4361(83)90157-X

[12] Hu N. S., Zhang L. C.: Some observations in grinding unidirectional carbon fibre-reinforced plastics. Journal of Materials Processing Technology, **152**, 333–338 (2004).
DOI: 10.1016/j.jmatprotec.2004.04.374

[13] Davim J. P., Reis P.: Damage and dimensional precision on milling carbon fiber-reinforced plastics using design experiments. Journal of Materials Processing Technology, **160**, 160–167 (2005).
DOI: 10.1016/j.jmatprotec.2004.06.003

[14] Moeller R.: Machining of composites with abrasive waterjets. in 'Proceedings of CFK-Valley Stade Convention. Stade, Germany' 48–49 (2007).

[15] Davim J. P., Barricas N., Conceicao M., Oliveira C.: Some experimental studies on CO_2 laser cutting quality of polymeric materials. Journal of Materials Processing Technology, **198**, 99–104 (2008).
DOI: 10.1016/j.jmatprotec.2007.06.056

[16] Mathew J., Goswami G. L., Ramakrishnan N., Naik N. K.: Parametric studies on pulsed Nd:YAG laser cutting of carbon fibre reinforced plastic composites. Journal of Materials Processing Technology, **89**, 198–203 (1999).
DOI: 10.1016/S0924-0136(99)00011-4

[17] Goeke A., Emmelmann C.: Influence of laser cutting parameters on CFRP part quality. Physics Procedia, **5**, 253–258 (2010).
DOI: 10.1016/j.phpro.2010.08.051

eXPRESS Polymer Letters Vol.5, No.3 (2011) 246–253
Available online at www.expresspolymlett.com
DOI: 10.3144/expresspolymlett.2011.24

Fracture behaviour of a self-healing microcapsule-loaded epoxy system

J. Lee[1*], *D. Bhattacharyya*[1], *M. Q. Zhang*[2], *Y. C. Yuan*[2]

[1]Centre for Advanced Composite Materials, Department of Mechanical Engineering, The University of Auckland, Private Bag 92019, Auckland 1142, New Zealand
[2]Key Laboratory for Polymeric Composite and Functional Materials of Ministry of Education, Materials Science Institute, Zhongshan University, Guangzhou 510275, PR China

Received 21 July 2010; accepted in revised form 14 December 2010

Abstract. The effect of temperature on the fracture behaviour of a microcapsule-loaded epoxy matrix was investigated. Microencapsulated epoxy and mercaptan-derivative healing agents were incorporated into an epoxy matrix to produce a polymer composite capable of self-healing. Maximum fracture loads were measured using the double-torsion method. Thermal aging at 55 and 110°C for 17 hours [hrs] was applied to heal the pre-cracked samples. The addition of microcapsules appeared to increase significantly the load carrying capacity of the epoxy after healing. Once healed, the composites achieved as much as 93–171% of its virgin maximum fracture load at 18, 55 and 110°C. The fracture behavior of the microcapsule-loaded epoxy matrix was influenced by the healing temperature. The high self-healing efficiency may be attributed to the result of the subsurface micro-crack pinning or deviation, and to a stronger microencapsulated epoxy and mercaptan-derivative binder than that of the bulk epoxy. The results show that the healing temperature has a significant effect on recovery of load transferring capability after fracture.

Keywords: *fracture and fatigue, polymer composites, smart polymers, self-healing, microcapsules*

1. Introduction

Polymer materials often experience micro-cracks during their service. Self-healing polymeric materials have the built-in capability to substantially recover their load transferring ability after damage. This field of self-healing materials is a relatively new one, beginning in the early 1990s, with the majority of the research occurring in the past decade [1, 2]. The ring-opening metathesis polymerization of dicyclopentadiene (DCPD) [3, 4], addition and ionic polymerization of epoxy [5], condensation polymerization of polysiloxane [6], organic solvents [7] and isocyanates [8], have been reported for automatically repairing cracks in polymers at room temperature.

Several researchers [5, 9–11] have successfully measured fatigue-crack propagation in epoxy resins. Brown and coworkers [5, 9] investigated the effect of embedded urea-formaldehyde (UF) microcapsules on the monotonic fracture properties of a self-healing epoxy. In addition to providing an efficient mechanism for self-healing, the presence of liquid-filled microcapsules increased the virgin monotonic–fracture toughness of epoxy by up to 127%. The increased toughening was correlated with a change in the fracture plane morphology from mirror-like to hackle markings with subsurface microcracking. The addition of microcapsules to an epoxy matrix significantly increased the resistance to crack growth under dynamic loading conditions.

*Corresponding author, e-mail: jim.lee@auckland.ac.nz

Caruso *et al.* [7] reported for solvent-based self-healing of epoxy materials an autonomic system yielding complete recovery of fracture toughness after crack propagation. Kamphaus *et al.* [12] used WCl_6 as a catalyst precursor for the ring-opening metathesis polymerization of exo-dicyclopentadiene in self-healing epoxy applications. Li *et al.* [13] have reported that the diameter of the poly (melamine–formaldehyde) (PMF) microcapsules containing DCPD has a significant influence on the self-healing efficiency.

In this work, microencapsulated epoxy and mercaptan-derivative were incorporated into epoxy resins. The fracture behavior of microcapsules-loaded epoxy matrix was investigated for the effect of temperature. It is found that the suitable healing temperature has a significant effect on the healing of the microcapsule-loaded epoxy matrix, thereby influencing the fracture behavior.

2. Experimental

2.1 Materials and sample preparation

Two types of epoxy resin were employed. One was diglycidyl ether of bisphenol A (ECS epoxy and ECS winter hardener, Uroxsys Ltd., East Tamaki, New Zealand) acting as the matrix polymer, and the other was diglycidyl tetrahydro-o-phthalate (DTHP, Jindong Chemical Plant, Tianjin, China) with epoxide equivalence weight of 0.65 mol (100 g)$^{-1}$, density of 1.24 g·ml^{-1} at 20°C, and viscosity of 0.36 Pa·s at 25°C as the polymerizable component of the healing agent. Accordingly, two types of curing agent were used. They are diethylenetriamine (DETA) supplied by Shanghai Medical Group Reagent Co. (Shanghai, China) working for pentaerythritol tetrakis (3-mercaptopropionate) (PETMP) with a boiling point of 275°C at 1 mmHg, density of 1.28 g·ml^{-1} at 20°C, and hydrosulfide group content of 26.55%, purchased from Fluka Chemie AG (Buchs, Switzerland). The catalyst benzyl dimethylamine (BDMA) with boiling a point of 183.5°C was purchased from Shanghai Medical Group Reagent Co. (Shanghai, China).

DTHP (400.0 g) was added to a 2wt% aqueous solution of sodium styrene–maleate copolymer (1200 ml). The mixture was vigorously stirred for 5 min and then a few drops of 1-octanol were added to eliminate surface bubbles of the epoxy emulsion. The prepolymer of melamine (62.5 g) and 37% formaldehyde (135.5 g) was synthesized at 70°C for 30 min and pH value of the solution was kept at about 9–10 by adding triethanolamine. Subsequently, the prepolymer solution was added to the above epoxy emulsion at 50°C with continuous agitation for 1 hr while pH value of the system was kept at about 3 by adding citric acid. Eventually, the reaction mixture was cooled down to room temperature and the deposit of microcapsules was separated through a Buchner funnel, rinsed with deionized water and vacuum dried. The microcapsules containing the hardener were prepared in two steps. Firstly, mercaptan-derivative was microencapsulated in a similar way as that adopted in making epoxy-loaded microcapsules. Then, the microcapsules were uniformly dispersed into catalyst solution (BDMP) at 40°C for a certain time (0.5–24 hrs), filtrated, rinsed with ethyl ether and dried at room temperature.

The unfilled epoxy specimens were produced through mixing 4.55 parts Uroxsys ECS resin with 1 part hardener, while the self-healing epoxy composites were prepared by mixing 5% of the microcapsules containing epoxy and its hardener. Either the unfilled epoxy or the filled version was poured into a closed silicone rubber mold, degassed and cured for 24 hrs at room temperature.

2.2. Fracture test

All the tests were conducted in an Instron 1186 mechanical testing machine (Instron, Norwood, MA, USA) to determine extension and maximum load using the three-point bending configuration. Steel devices were fabricated to fix test specimens for the double-torsion test. Prior to testing, a notch was molded and then sharpened by tapping a fresh razor blade in to the material. 3–5 samples were tested for each condition. The samples were cut to 60 mm×100 mm size with 10 mm notch and side

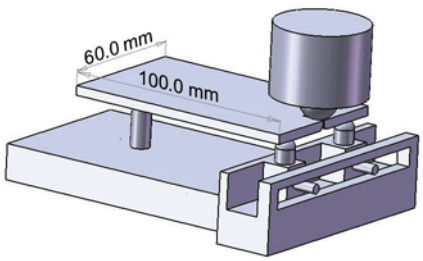

Figure 1. An illustration of the sample loading configuration

grooves along the centreline of the sample. Figure 1 illustrates the basic geometry of the experimental setup. For fracture tests a pin loading and constant displacement rate condition with 0.2 mm/min were used until the crack length was ~2 mm. The above samples were unloaded, healed and tested again after 17 hrs from initial fracture event at 18, 55 or 110ºC. Healing efficiencies were determined by comparing the healed peak loads to the virgin peak loads.

2.3. Characterization

2.3.1. Optical images and scanning electron microscope (SEM)

The appearance of the microcapsules was observed by optical microscope Leica IC3D (Leica Mikrosysteme Vertrieb GmbH, Wetzlar, Germany). The surface morphology of samples was examined by scanning electron microscopy (XL30 ESEM-FEG, Philips, FEI Company, Hillsboro, Oregon, USA). Microcapsules were mounted on a conductive stage. Samples were sputtered with a thin layer (10 nm) of gold−palladium to reduce charging.

2.3.2. Size

The particle size distribution was examined using a Malvern Mastersizer 2000 Ver. 5.54 (Malvern, UK). The particle refractive index parameter was 1.58. The technique is based around the principle that particles passing through a laser beam will scatter light at an angle that is directly related to their size.

2.3.3. DSC

Differential scanning calorimetry (DSC) analysis (TA Q1000 calorimeter, TA Instruments, New Castle, DE, USA) was used to investigate the reactivity of the prepared capsules. Small amounts of samples (5–10 mg) were heated from –20 to 140°C at a rate of 5°C/min in a N_2 environment.

2.3.4. FTIR

Fourier-transform infrared (FTIR) spectra were obtained by Atlas FTIR spectrometer to identify the chemical structure of the specimens, which were prepared by grinding the samples with potassium bromide (KBr) or by appending the samples to a diamond using an Attenuated Total Reflectance (ATR) method.

3. Results and discussion

3.1. Microstructure and particle size distribution of microcapsules

Figure 2 shows the SEM micrograph of microcapsules. The SEM image of Figure 2b was taken from the surface of a microcapsule-loaded epoxy. The surface of microcapsules is rough, and it may be composed of PMF nanoparticles protruding from the surface [15]. The protuberant nanoparticles can increase the surface area of microcapsules and enhance surface adhesion. Furthermore, the microcapsules can form hydrogen bonding with the matrix due to the presence of polar groups (amine and hydroxyl) on their melamine-formaldehyde

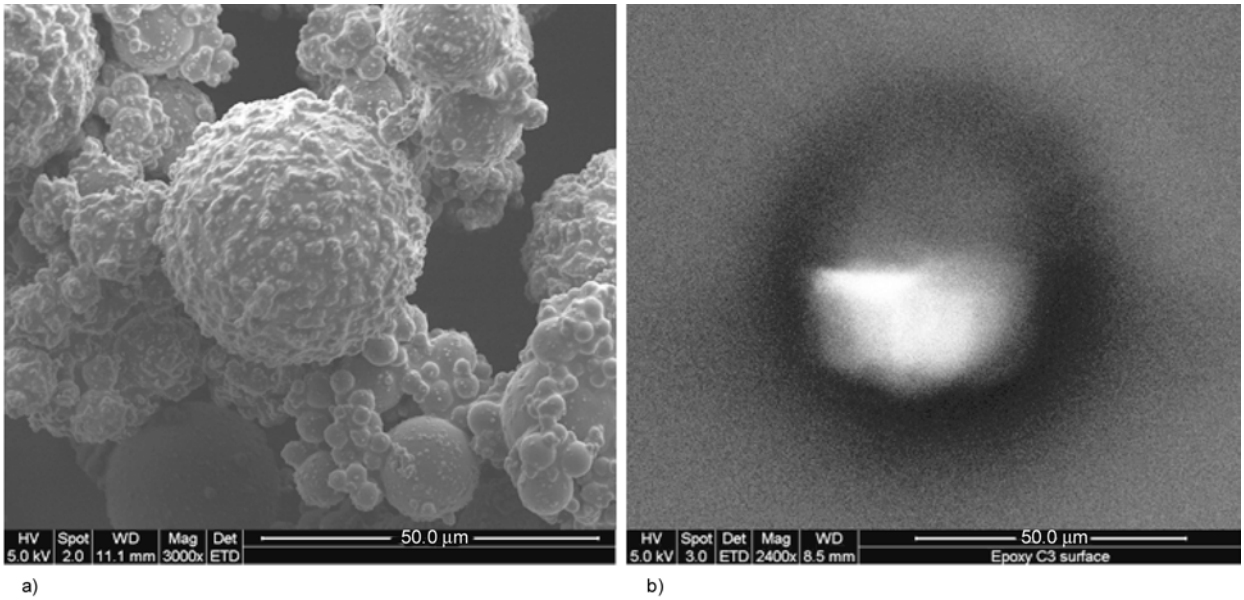

Figure 2. SEM micrographs of epoxy-loaded microcapsules a); the surface of a micro-capsule-loaded epoxy b)

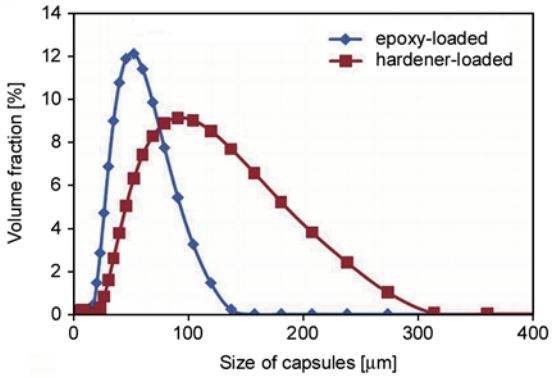

Figure 3. Size distribution of microcapsules: Epoxy- and Hardener-loaded

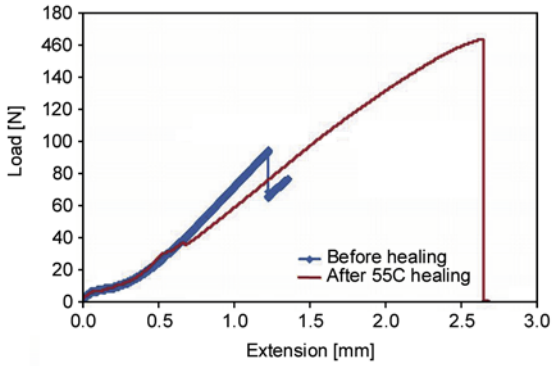

Figure 5. The load−extension curves before and after 55°C healing

shells. In Figure 2b it is evident that there is a healant inside the microcapsule. Figure 3 shows the size distribution of microcapsules with epoxy and hardener. The microcapsule size was in a wide range of 10–150 (A) and 20–300 (B) μm. The reason is that in the region of flow away from the propeller during the preparation of microcapsules, many larger microeddies exist, and in the vicinity of the propeller, many smaller microeddies exist, which result in a wider length scale [16]. In this study, the mean diameters of the prepared microcapsules were ~50 (A) and 100 (B) μm.

3.2. The effects of healing temperature on the fracture behaviour

The control experiments of epoxy without microcapsules show no healing effects, in agreement with our results reported by Yuan *et al.* [14]. Figure 4 shows curves of the fracture load with extension at the compressive direction for the samples under different healing temperatures at 18, 55 and 110°C lasting 17 hrs. They clearly show that the maximum fracture loads at 55 and 110°C are higher than at 18°C. At ~55°C it shows the highest fracture load.

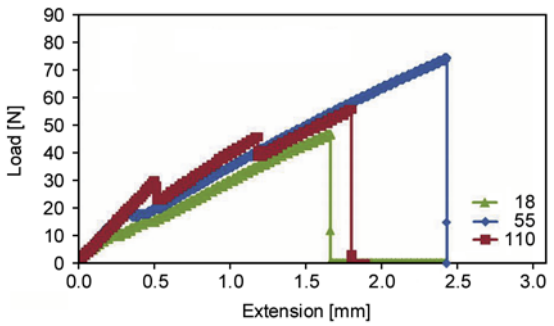

Figure 4. Load−extension curves of epoxy samples under different healing temperatures (*L* to *R*: 18, 110 and 55°C)

The load-extension curves show in a zigzag way, especially at a higher temperature 110°C, which may be explained by the difference of polymerization and heat stability of the self-healing crosslinkers. The rapid crack growth takes place after the maximum load. Figure 5 shows load−extension curves before and after 55°C healing. The maximum fracture loads increase significantly after 55°C healing. The virgin sample loads nonlinearly followed by a linear regime to 95 N. This is followed by a drop in load (virgin slope failed and crack initiated) and a second linear regime until the crack length (not extension) to ~2 mm length, which suggests that the crack has propagated in the material. The crack of virgin sample retains some load-bearing capability, however the load of crack initiation is higher than the load of propagation in the material. The healed sample loads non-linearly followed by a linear regime to around ~30 N followed by a minor zigzag regime without a clear crack initiation and loading until the sample would have a same crack length, however the rapid crack growth happens at a 165 N load (crack-length independent).

The healing efficiency values of the microcapsules-loaded epoxy samples healing lasting for 17 hrs at different temperatures are shown in Figure 6. The healing efficiency values are determined by comparing the healed peak loads to the virgin peak loads. The average self-healing efficiency at healing temperature 18, 55 and 110°C for 17 hrs is 93, 171 and 158%. The given values are mean values of three parallel tests. It is obvious that the self-healing efficiency of the microcapsule-loaded epoxy/ mercaptan-derivative samples is significantly higher under healing temperature at ~55°C. This result is

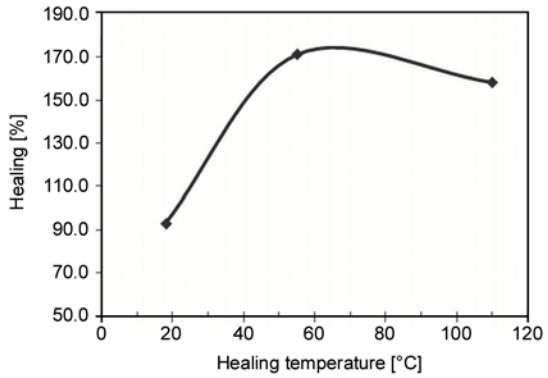

Figure 6. The self-healing efficiency of microcapsules-loaded epoxy samples with a healing temperature

in accordance with the DSC result which shows the healing peak temperature 56.53°C of microcapsules.

3.3. FTIR and DSC

The microcapsule-loaded epoxy samples under different healing temperatures at 18, 55 and 110°C were investigated by FTIR spectra. The absorption peaks at 2800–3200, 2300–2400 and 1500–1800 cm^{-1} are attributed to C–H, CO_2 and carbon double bond absorption bands respectively. Figure 7

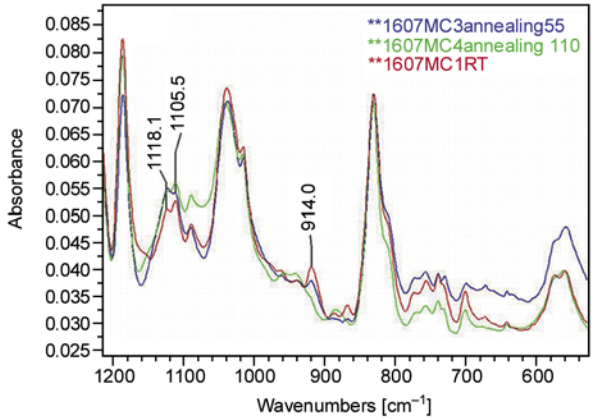

Figure 7. Expanded FTIR spectra between 1200 and 500 cm^{-1}

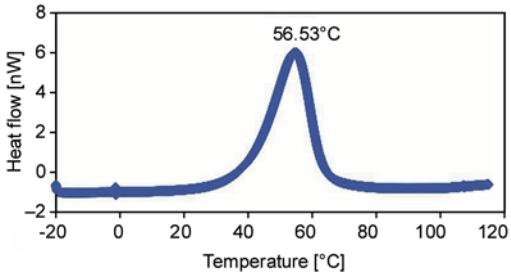

Figure 8. DSC curve of the epoxy and hardener-loaded microcapsules mixture

shows expanded FTIR spectra between 1200 and 500 cm^{-1}. The peaks at 1118 and 1105 cm^{-1} correspond to C–O stretch. The stretch mode of the oxirane ring of the epoxy group appears at 914 cm^{-1}. This disappears with increasing temperature probably due to the curing of epoxy at a higher temperature.

Figure 8 shows DSC curves of the epoxy and hardener-loaded microcapsules mixture. The exothermic reaction peak at 56.53°C with onset temperature 41.77°C is the curing temperatures of the epoxy and hardener-loaded microcapsules. It is in accordance with the results obtained by the above test results which show that the fracture load and healing efficiency values of the microcapsule-loaded epoxy/mercaptan-derivative samples are significantly higher under healing temperature at ~55°C.

3.4. Fracture morphology and photo elasticity

Using a polariscope, the specimens that were cracked (a) or healed (b) under stress are shown in Figure 9. Figure 9a shows the end of the crack in specimen with birefringence. Figure 9b shows the healed crack without birefringence.

The images in Figure 10 show a typical crack surface for a microcapsule specimen at 18 and 55°C. With regard to the microcapsule specimen, it is vis-

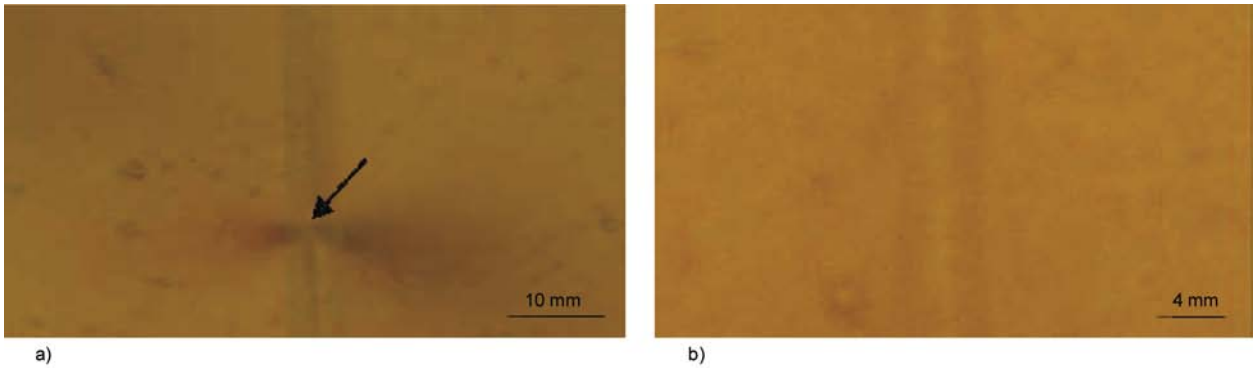

Figure 9. Photoelastic stress distribution of cracked a) and healed b) samples

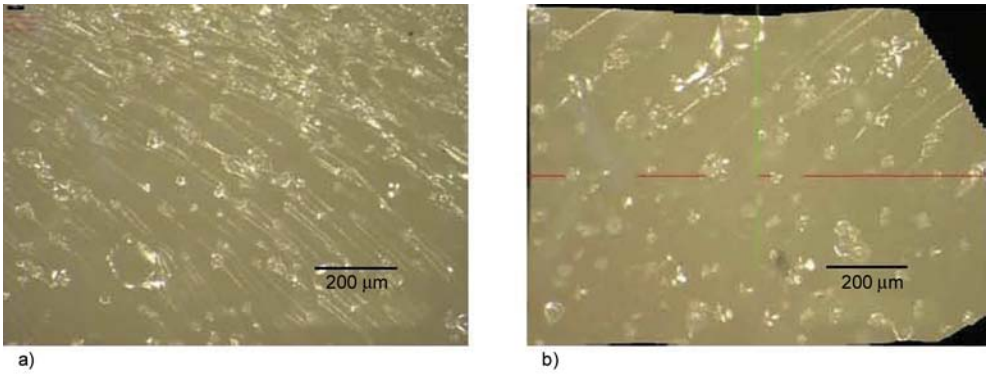

Figure 10. Optical images of fractured microcapsules-loaded epoxy cured at 18°C a) and 55°C b)

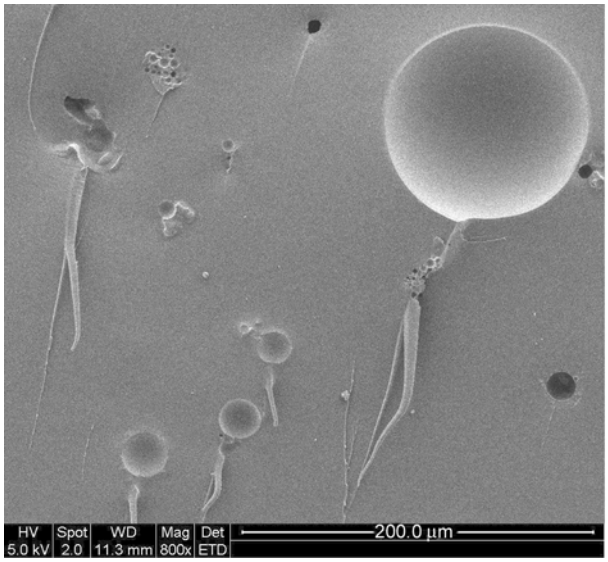

Figure 11. SEM micrograph of fractured microcapsules-loaded epoxy

ible that the healants of fractured microcapsules have flowed out to the fracture surface so that they can react and heal the cracks at a suitable temperature. The SEM image in Figure 11 also clearly shows the micro-cracking pinning from the fractured microcapsules. The subsurface micro-crack pinning on the fracture plane (Figure 11) may contribute to additional energy consumed in the course of fracture [14, 17].

3.5. Discussion

It has been reported that for PMF microcapsules containing DCPD applied to polymeric composites, the higher self-healing efficiency can be obtained by adding a lower content of microcapsules with larger diameter or by adding a higher content of microcapsules with smaller diameter, and increasing microcapsule diameter can improve the maximum self-healing efficiency [13]. Although microcapsules don't behave like hard solid particles, similar fracture behavior has been in rubber toughened epoxy [17]. The deformation and subsurface micro-cracking associated with rubber toughened epoxy are similar to the mechanisms identified for microcapsule toughened epoxy. Previous reports [14, 17, 18] which have achieved over 100% healing have suggested that such high efficiency healing is the results of crack deviation or pinning from the original damage line or healing of the material past the original pre-crack using the higher fracture toughness of repair binder than that of the bulk material.

The fracture behavior of microcapsules-loaded epoxy matrix was investigated using a double torsion test which is based on a Mode I (opening) loading. The typical virgin sample loads nonlinearly followed by a linear regime. This is followed by a drop in load (virgin slope failed and crack initiated) and a second linear regime with a crack development. The healed sample loads non-linearly followed by a linear regime, then zigzag regime without a clear crack initiation and loading linearly until the rapid crack growth happens. Clearly microencapsulated epoxy and mercaptan-derivative healing agents can have the capability to heal the cracks after damage, but also provides the damaged sites with a higher fracture load. Here a higher self-healing efficiency can be achieved by choosing a suitable curing temperature. The healing efficiency increases, then decreases with a healing temperature. The best healing temperature at about 55°C curing temperature of microencapsulated epoxy and mercaptan-derivative with healing efficiency 171% is determined by the fracture test and DSC measurement. The increased fracture load is correlated with a healant release and curing. The subsurface micro-crack pinning or deviation on the fracture

plane and a stronger microencapsulated epoxy and mercaptan-derivative binder than that of the bulk epoxy along the original pre-crack may contribute to additional energy consumed in the course of fracture, leading to a greater than 100% self-healing efficiency. The reduced performance after higher temperature annealing at 120°C may be mainly due to thermal degradation of additional self-healing microcapsules. Based on our previous test results, the Epoxy/Mercaptan-derivative microcapsules provide two independent effects: increase the load carrying capacity of the epoxy from general toughing after healing and the ability to self-heal the virgin fracture at room temperature.

4. Conclusions

The fracture behavior of microcapsule-loaded epoxy matrix is studied for the effects of temperature. The load-extension curves start non-linearly followed by a linear regime, then zigzag regime and a linear regime until fails. The microencapsulated epoxy and mercaptan-derivative healing agents have flowed out to the fracture surface of epoxy so that they can react and heal the cracks. The addition of microcapsules appears to significantly increase the load carrying capacity of the epoxy after healing. The healing efficiency increases, then decreases with the healing temperature. The best healing temperature is at the about 55°C curing temperature of microencapsulated epoxy and mercaptan-derivative with healing efficiency up to self-healing efficiency 171%. Heating the polymer samples after fracture will change the mechanical properties, resulting in changes in the fracture strength due to the self-healing microcapsules or thermal degradation on polymers. It shows that the suitable healing temperature has a great effect on healing, thereby influencing the fracture behavior. The subsurface micro-crack pinning or deviation on the fracture plane and a stronger microencapsulated epoxy and mercaptan-derivative binder than that of the bulk epoxy may lead to a greater than 100% self-healing efficiency. The Epoxy/Mercaptan-derivative microcapsules provide two independent effects: the capability to recover their load transferring ability after fracture and the ability to self-heal the virgin fracture at room temperature.

Acknowledgements

This work was supported by Foundation for Research, Science and Technology for New Zealand Science & Technology Post Doctoral Fellowship. Thanks also go to the lab staff at CACM, Associate Professor Allan Easteal and Ms Michel Nieuwoudt, Department of Chemistry, the University of Auckland, New Zealand.

References

[1] Murphy E. B., Wudl F.: The world of smart healable materials. Progress in Polymer Science, **35**, 223–251 (2010).
DOI: 10.1016/j.progpolymsci.2009.10.006

[2] Yuan Y. C., Yin T., Rong M. Z., Zhang M. Q.: Self healing in polymers and polymer composites. Concepts, realization and outlook: A review. Express Polymer Letters, **2**, 238–250 (2008).
DOI: 10.3144/expresspolymlett.2008.29

[3] White S. R., Sottos N. R., Geubelle P. H., Moore J. S., Kessler M. R., Sriram S. R., Brown E. N., Viswanathan S.: Autonomic healing of polymer composites. Nature, **409**, 794–797 (2001).
DOI: 10.1038/35057232

[4] Kessler M. R., Sottos N. R., White S. R.: Self-healing structural composite materials. Composites Part A: Applied Science and Manufacturing, **34**, 743–753 (2003).
DOI: 10.1016/S1359-835X(03)00138-6

[5] Brown E., Sottos N., White S.: Fracture testing of a self-healing polymer composite. Experimental Mechanics, **42**, 372–379 (2002).
DOI: 10.1007/BF02412141

[6] Cho S. H., Andersson H. M., White S. R., Sottos N. R., Braun P. V.: Polydimethylsiloxane-based self-healing materials. Advanced Materials, **18**, 997–1000 (2006).
DOI: 10.1002/adma.200501814

[7] Caruso M. M., Blaiszik B. J., White S. R., Sottos N. R., Moore J. S.: Full recovery of fracture toughness using a nontoxic solvent-based self-healing system. Advanced Functional Materials, **18**, 1898–1904 (2008).
DOI: 10.1002/adfm.200800300

[8] Jinglei Y., Keller M. W., Moore J. S., White S. R., Sottos N. R.: Microencapsulation of isocyanates for self-healing polymers. Macromolecules, **41**, 9650–9655 (2008).
DOI: 10.1021/ma801718v

[9] Brown E., White S., Sottos N.: Fatigue crack propagation in microcapsule-toughened epoxy. Journal of Materials Science, **41**, 6266–6273 (2006).
DOI: 10.1007/s10853-006-0512-y

[10] Karger-Kocsis J., Friedrich K.: Microstructure-related fracture toughness and fatigue crack growth behaviour in toughened, anhydride-cured epoxy resins. Composites Science and Technology, **48**, 263–272 (1993).
DOI: 10.1016/0266-3538(93)90143-5

[11] Nagasawa M., Kinuhata H., Koizuka H., Miyamoto K., Tanaka T., Kishimoto H., Koike T.: Mechanical fatigue of epoxy resin. Journal of Materials Science, **30**, 1266–1272 (1995).
DOI: 10.1007/BF00356129

[12] Kamphaus J. M., Rule J. D., Moore J. S., Sottos N. R., White S. R.: A new self-healing epoxy with tungsten (VI) chloride catalyst. Journal of the Royal Society: Interface, **5**, 95–103 (2008).
DOI: 10.1098/rsif.2007.1071

[13] Li Y., Liang G-Z., Xie J-Q., He S-B.: Synthesis and characterization of microencapsulated dicyclopentadiene with melamine–formaldehyde resins. Colloid and Polymer Science, **285**, 781–791 (2007).
DOI: 10.1007/s00396-006-1621-5

[14] Yuan Y. C., Rong M. Z., Zhang M. Q., Chen J., Yang G. C., Li X. M.: Self-healing polymeric materials using epoxy/mercaptan as the healant. Macromolecules, **41**, 5197–5202 (2008).
DOI: 10.1021/ma800028d

[15] Yuan L., Liang G., Xie J., Li L., Guo J.: Preparation and characterization of poly(urea-formaldehyde) microcapsules filled with epoxy resins. Polymer, **47**, 5338–5349 (2006).
DOI: 10.1016/j.polymer.2006.05.051

[16] Dobetti L., Pantaleo V.: Application of a hydrodynamic model to microencapsulation by coacervation. Journal of Microencapsulation, **19**, 139–151 (2002).
DOI: 10.1080/02652040110055199

[17] Brown E. N., White S. R., Sottos N. R.: Microcapsule induced toughening in a self-healing polymer composite. Journal of Materials Science, **39**, 1703–1710 (2004).
DOI: 10.1023/B:JMSC.0000016173.73733.dc

[18] Yin T., Rong M. Z., Zhang M. Q., Yang G. C.: Self-healing epoxy composites - Preparation and effect of the healant consisting of microencapsulated epoxy and latent curing agent. Composites Science and Technology, **67**, 201–212 (2007).
DOI: 10.1016/j.compscitech.2006.07.028

eXPRESS Polymer Letters Vol.5, No.3 (2011) 254–261
Available online at www.expresspolymlett.com
DOI: 10.3144/expresspolymlett.2011.25

Shape recovery in a thermoset shape memory polymer and its fabric-reinforced composites

J. Ivens[1, 2*], *M. Urbanus*[2], *C. De Smet*[3]

[1]Department of Applied Engineering, Lessius University College, Campus De Nayer, J. De Nayerlaan 5, B-2860 Sint-Katelijne Waver, Belgium
[2]Department of Metallurgy and Materials Engineering, Katholieke Universiteit Leuven, Kasteelpark Arenberg 44, B-3001 Leuven, Belgium
[3]Sint-Lucas Architectuur, Hogeschool voor Wetenschap en Kunst, Hoogstraat 22, B-9000 Gent, Belgium

Received 15 September 2010; accepted in revised form 4 January 2011

Abstract. A shape memory polymer (SMP) can be deformed from a permanent to a temporary shape above their transformation temperature. Upon reheating, the SMP spontaneously returns to the permanent shape. SMP's show high deformability, but the recovery stresses are very low, thus limiting the size of the components. This paper presents the first results of an ongoing research to develop large sized components based on SMP. To achieve higher recovery stresses, asymmetric fibre reinforced shape memory composites were produced (SMPC) using resin transfer moulding. The results show a 30-fold increase in recovery stress, compared to the neat SMP resin. The recovery stress is independent of the deformation temperature, but is strongly affected by the degree of deformation. At higher deformation levels, crazing occurs. Even though the visible effects of the crazing disappear during reheating, it does influence the recovery stress. This indicates that the ability to recover the permanent shape might change in cyclic loading. All composites tested show complete recovery upon reheating. The rate of shape recovery is higher when the fibre reinforcement is loaded in compression.

Keywords: *polymer composites, smart polymers, material testing*

1. Introduction

Most shape memory materials are defined by one permanent and one temporary shape (one-way transformation) or two permanent shapes (two-way transformation). A trigger – usually heat – can induce the change from one (temporary or permanent) shape to another (permanent) shape. The shape transformation and the work done during the transformation are determined by the release of the energy, stored inside the material. Shape memory effects are found in metals, ceramics and polymers, of which the metallic shape memory alloys (SMA) like Nitinol are the most widely used, as they combine a high level of recovery stress with a reasonable deformation [1].

Shape memory polymers can be a thermoplastic, a thermoset or an elastomeric material; they exhibit much higher levels of deformation than SMA. The transformation temperature of an SMP can be the melting temperature or the glass transition temperature of a 'soft' phase [2].

For a thermoset SMP, the transformation temperature is the glass transition temperature T_g. One type of SMP is a single phase material, consisting of polymer chains with a certain (limited) number of cross-links [2–5]. The cross-links are net points, where the memory of the permanent shape is stored, while the free polymer chains between the cross-links are switching segments that obtain increased mobility above T_g. Upon deformation, the mobile

*Corresponding author, e-mail: jan.ivens@mtm.kuleuven.be

polymer chain segments are stretched in the loading direction, resulting in a decreased entropy; at the same time, the net points elastically deform; the overall result is an increase in enthalpy of the SMP. When the material is allowed to cool down in deformed state, the loss of mobility of the polymer chain segments in the switching segments stabilizes the temporary shape.

A second type of SMP is a two phase material that both form an interconnected 3-dimensional network [6, 7]. The elastic energy is stored in the hard phase, and is responsible for the recovery of the permanent shape, while the soft phase, upon heating above its transformation temperature (often its melting temperature), enables the deformation to a temporary shape.

The major drawback of shape memory polymers is the low recovery stress (Figure 1), limiting the size of commercial components to a few centimetres: the recovery stress of larger components is insufficient to counter the components weight. The solution consists of reinforcing the SMP with particles or fibres. The addition of carbon nanotubes results in a 50 to 100% increase of the recovery stress and improved conductivity but the expense of a reduced shape recovery effect [8–10]. Alternative particle reinforcements like SiC [11] and carbon black [12] are less effective.

Some research on fibre reinforced SMP laminates has been reported. The fibre reinforcement dramatically increases the recovery stress [13]. Gall *et al.* [14] found only a limited effect of the fibre reinforcement on the recovery ratio, however the elastic spring back increased significantly. These results indicate that the stored elastic energy is an important factor in the shape memory effect. The same authors also showed that microbuckling is important in the high temperature deformation; their observations seem to indicate that the microbuckling is reversible [14]. Zhang *et al.* [15] evaluated asymmetric SMPC in bending and observed that SMPC with the fibre reinforcement under compression exhibited a faster recovery, a higher recovery ratio and a higher recovery stress. Continuous fibre reinforcement strongly affects the deformation limits of the SMP: under tension in the fibre direction, the shape memory effect is totally lost. Although some small size applications have been developed [13, 16], there is a need for more research on continuous fibre reinforced polymer composites to develop functioning large SMPC objects.

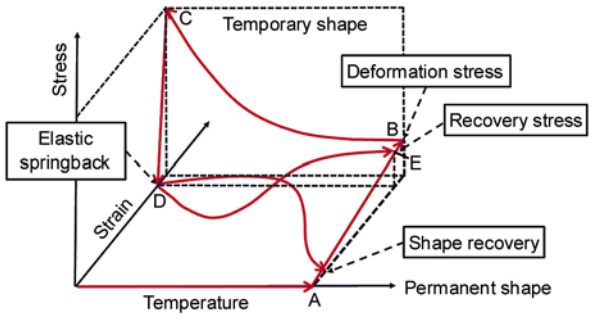

Figure 1. The thermomechanical cycle, describing the behaviour of an SMP. After heating to temperature T_h (A), the material is deformed (B) and subsequently cooled (C). Elastic springback results in a change in strain (D). Upon unconstrained reheating to T_h, the material returns to (A). If the temporary shape is constrained, heating results in a stress build up (E), the recovery stress.

2. Materials and test methods

2.1. Materials

The material used in this research is Veriflex VF62 of CRG Industries (Dayton, OH). This thermoset styrene-based resin, is cured with benzoyl peroxide in a 24:1 ratio. Neat resin plates were produced by casting the reactive resin in a 4 mm thick mould cavity. The resin was cured according to the following cure cycle:

– Heat to 75°C with a heating rate of 1°C/min.
– Maintain 75°C during 3 hours.
– Heat to 90° with a heating rate of 5°C/hour.
– Heat to 110°C with a heating rate of 10°C/hour.

The properties of the neat Veriflex VF62 resin are presented in Table 1. The transformation temperature was determined by the glass transition temperature of the cured resin using Dynamic Mechanical Thermal Analysis (TA Instruments Q800). An oscillation of 1 Hz with a strain amplitude of 0.05% strain was imposed in a three-point bending set-up, using a span length of 34 mm, while the temperature is increased to 95° with a heating rate of 2°C/min.

Table 1. Properties of Veriflex CF62

Tensile strength	23.00 MPa
Compression strength	32.40 MPa
E-modulus	1.24 GPa
Strain to failure	3.90%
T_g: loss modulus tanδ	62°C 75°C

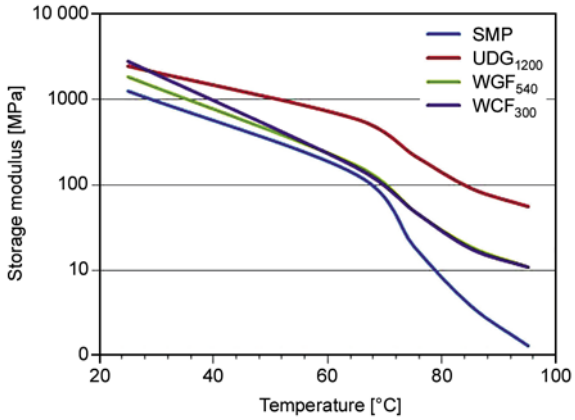

Figure 2. Storage modulus as a function of temperature, determined by dynamic mechanical analysis

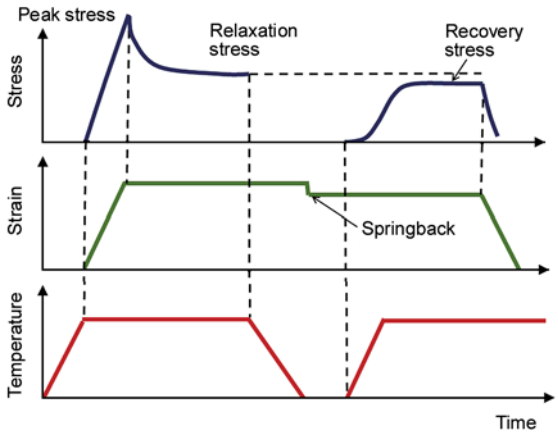

Figure 3. Temperature-strain cycle of the TMA experiments: the specimen is heated at 3°C/min to the deformation temperature. The specimen is deformed (3%/min) to a set maximum strain and held for 30 minutes to allow stress relaxation. The specimen is cooled down in deformed state. The residual stress is removed and the elastic spring back is recorded. The restrained specimen is reheated (3°C/min) to 75°C, while the recovery stress is measured. Finally, the specimen is returned to the permanent shape.

Three types of fibre reinforcements were selected: a quasi-unidirectional non-crimp E-glass fabric (UDG1200; areal weight 1200 g/m^2, supplier: Saertex, Germany), an E-glass plain woven fabric (WGF540; areal weight 540 g/m^2 supplier: Saint-Gobain Technical Fabrics, Belgium) and a T300 carbon fibre twill-weave (TWC300; areal weight 300 g/m^2, supplier Hexcel Reinforcements, France). Composite plates were produced using resin transfer moulding in a heated aluminium mould, containing a single layer of reinforcement. The resulting plate thickness of 3.2 mm resulted in fibre volume fractions of 16.5% (UDG1200), 7.7% (WGF540) and 5% (TWC300) respectively. Because the fabric thickness is lower than the plate thickness, the fabric was held against the mold surface to avoid 'swimming'. Consequently, the resulting composite is asymmetric. Figure 2 shows the evolution of the storage modulus as a function of temperature. The storage modulus at room temperature is low, because of the low fibre volume fraction of the specimens, and because the modulus was determined in a short span three-point bending test, where shear deformations cannot be neglected. Moreover, the storage modulus is an apparent modulus: since the laminates are asymmetric, engineering constants are undefined.

2.2. Test methods

The deformation-cooling-reheating cycle of SMP and SMPC samples was determined in a single cantilever beam test on small samples using the same TA Instruments Q800 equipment, in static mode (TMA). The temperature-strain cycle and the resultant stress are shown in Figure 3. UDG1200 SMPC and pure SMP specimens – 17 mm×10 mm×3 mm – were deformed to a strain of 10% at 75°C. Additional tests up to 20% deformation at 75°C and 10% deformation at 65°C and 85°C were performed on UDG1200 SMPC (§ 3.1).

Due to the small specimen size for TMA testing, the shape memory cycle was repeated on larger (80 mm× 20 mm×3 mm) UDG1200 SMPC specimens, loaded in three point bending with a span length of 50 mm. Specimens were heated using silicone oil, while they were cooled in air. Different maximum strain levels were used, and specimens were subjected to multiple cycles to evaluate the repeatability of shape recovery and the effect of local damage on the recovery stress (§ 3.2).

The recovery rate and ratio were measured using a similar set-up as Gall *et al.* [14], shown in Figure 4 (§ 3.3). A flat specimen is heated and subsequently deformed on a tubular surface, where it is allowed to cool down. During reheating, the shape recovery (via the angle between the two specimen ends) is measured as a function of the recovery time. The SMP and the three SMPC materials were tested at 75°C with 33% flexural strain. Two deformation levels and two deformation temperatures were used for UDG1200. Tests were performed with the fabric

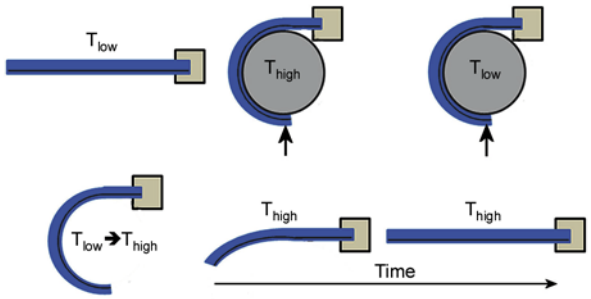

Figure 4. A specimen is deformed to a preset radius at high temperature and constrained during deformation. The specimen is reheated, and it gradually returns to its permanent flat shape. The recovery rate and ratio are measured. The position of the fabric is indicated by the grey line in the specimen: in this picture, the fabric is on the compressive side of the laminate.

at the compressive side (as shown in Figure 4) and on the tensile side of the specimen.

3. Results and discussion

3.1. Deformation and recovery stress

Figure 5, obtained from the TMA-experiments, shows the variation of the stress during the deformation phase and the reheating phase of UDG1200 SMPC. During the deformation, the stress builds

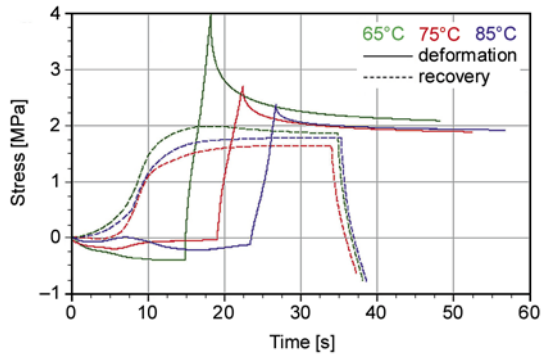

Figure 5. Stress as a function of time during the deformation phase (solid lines) and the recovery phase (dashed lines) of UDG1200 SMPC, for different deformation temperatures

rapidly, reaching a peak stress, followed by stress relaxation, evolving to a plateau value. During the reheating to 75°, the specimen builds up recovery stresses. Table 2 shows the numerical data, extracted from the curves, for neat SMP and for the different SMPC. UDG1200 SMPC was tested at different deformation temperatures and deformation levels. The characteristics are defined in Figure 3. The UDG1200 specimens were submitted to a second deformation reheating cycle, as indicated by (2).

The results of the experiments on UDG1200 show a decrease of the peak stress as the deformation temperature increases. The peak stress is caused by the resistance to deformation in the cross-linked net points and in the (linear) switching segments of the material. At 65°C – below the transformation temperature – the switching segments still have some stiffness. The peak stress drops significantly when the T_g is exceeded. All specimens exhibit stress relaxation. The viscous nature of the switching segments is responsible for the relaxation, but the stress does not decay to zero: a plateau value is reached; it is related to the built-up internal stresses by the rigid net points of the polymer and its level is indicative of the stored energy. The plateau stress is independent of the deformation temperature. For 10% deformation, the relaxation stress is 1.75 MPa. During reheating of the constrained specimen, recovery stresses are built up. The effect of the deformation temperature on the recovery stress is insignificant. The recovery stress level is 1.65 MPa for 10% deformation, i.e. 94% of the plateau stress level during the deformation stage. Compared with the neat resin, the relaxation and recovery stresses are increased 30-fold by the addition of the 13% glass fibre reinforcement!

The stress levels in the other composites are significantly lower. This is mainly caused by the difference in fibre volume fraction, as shown in Figure 6.

Table 2. Numerical data, obtained from the TMA experiments. 75°(2) indicates a second deformation – reheating cycle

	TMA results		Peak stress [MPa]	Relaxation stress [MPa]	Spring back [%]	Recovery stress [MPa]
	Strain [%]	Temperature [°C]				
SMP	10%	75°C	0.085±0.005	0.05±0.01	0.025±0.005	0.05±0.01
TWC300	10%	75°C	0.5	0.3	0.07	0.3
WGF540	10%	75°C	1.0±0.1	0.62±0.05	0.16±0.03	0.55±0.03
UDG1200	10%	65°C	3.65±0.45	1.95±0.15	0.45±0.35	1.65±0.3
		75°C	2.4±0.2	1.75±0.12	0.25±0.10	1.60±0.06
		85°C	2.2±0.2	1.75±0.15	0.15±0.05	1.65±0.12
	20%	75°C	5.9±1.3	3.9±0.5	2±1	3±1
	20%	75°C (2)	4.5±0.7	3.4±0.4	1.5±1.5	2.5 ±0.7

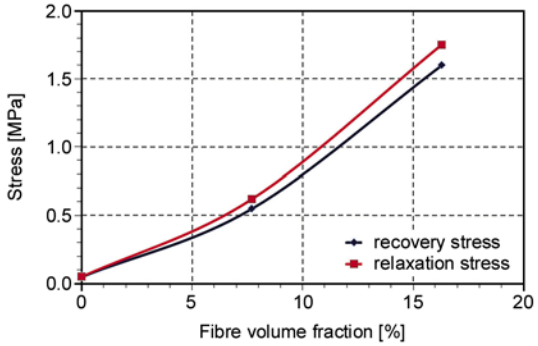

Figure 6. Recovery and relaxation stress as a function of the fibre volume fraction for the different glass fibre reinforced composite materials

It must be pointed out that more experiments are needed to discriminate between glass and carbon composites.

3.2. Repeatability and effect of damage

Table 2 shows that the recovery ratio decreases with increasing deformation strain. This is due to the increased elastic spring back and due to damage: the TMA specimens deformed up to 20% strain showed stress whitening after cooling and unloading. Stress whitening was also observed during the larger scale three point bending tests. These experiments focused on repeated deformation-reheating cycles. For each cycle, the maximum flexural strain was increased. The flexural stress during deformation is presented in for 4 consecutive cycles. Stress whitening was observed at a much lower strain level (3.6%) in comparison with the small TMA-samples.

Stress whitening is caused by crazing in the switching segments of the SMP. Kasajima *et al.* [17] have observed that stress whitening created at low strain levels disappears upon unloading. Higher strain levels result in residual stress whitening, but Kasajima *et al.* showed that stress whitening can be removed by heating. This was corroborated by the authors observations on the SMPC specimens: the stress whitening in the 4% strained specimens disappeared after recovery heating, while for the 7.5 and 11% deformation levels, prolonged heating was needed to remove the stress whitening (Figure 7).

Although these observations seem to suggest that the effects of stress whitening are recoverable, this is not correct. Kasajima observed a decrease in yield strength after deformation and subsequent reheating to remove the stress whitening. Similar results were obtained in three point bending (Figure 8): a clear drop in yield stress is observed between the first and the second cycle, yet the additional drop from the second to the third cycle is much smaller. Repeating the same deformation in the fourth cycle gave the same stress strain curve. It can therefore not be excluded that the effects of the

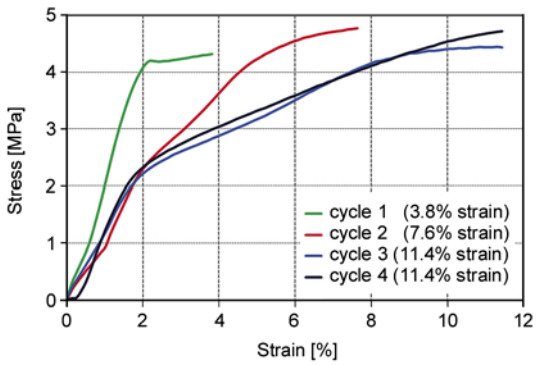

Figure 8. Flexural stress-strain curves at the transformation temperature for UDG1200 SMPC. The same sample was loaded in a cyclic manner. Each curve present the loading curve of a cycle.

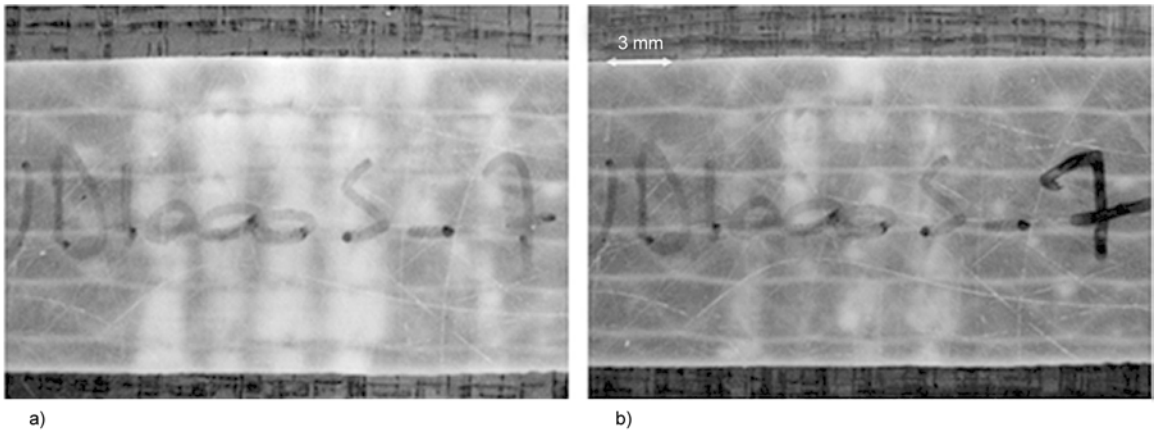

Figure 7. Stress whitening in the UDG1200 specimens, loaded in three-point bending. More stress whitening is visible directly after recovery (a). Most stress whitening disappears after 30 minutes at elevated temperature (b).

stress whitening are not fully reversed, and this could also be responsible for the lower recovery stress to relaxation stress ratio (Table 2). An additional reduction in recovery stress during a second load cycle was found, similar to Kasjima's observations. Further research is necessary to establish the effect of repeated deformation and shape recovery on the recovery stress and the recovery rate.

3.3. Recovery ratio and rate

The recovery ratio and rate were measured using the set-up shown in Figure 4. Figure 9 and 10 shows the recovery angle as a function of time for for the different materials tested. All composite specimens exhibit full recovery, while the neat SMP is unable to recover the permanent shape. The overall recovery rates are low, compared to what is found in shape memory metal alloys. A higher stiffness results in a faster shape change. Figure 10 shows the effect of temperature and deformation level on the recovery rate. A higher temperature and a higher deformation strain result in slower recovery; the effect of strain is small.

Figure 11 shows the effect of the asymmetry on the shape recovery of the carbon fabric TWC300 SMPC. A much higher recovery rate is found if the fabric is located in the compressive side on the test

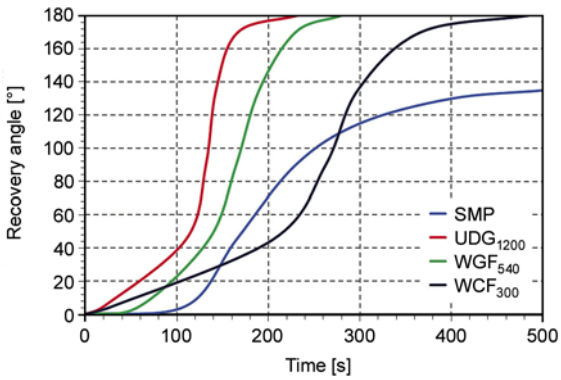

Figure 9. Recovery angle as a function of time for the neat SMP and for the fabric reinforced composites, measured using the set-up shown in Figure 4. All composites show complete shape recovery, while the neat SMP is unable to counteract gravity.

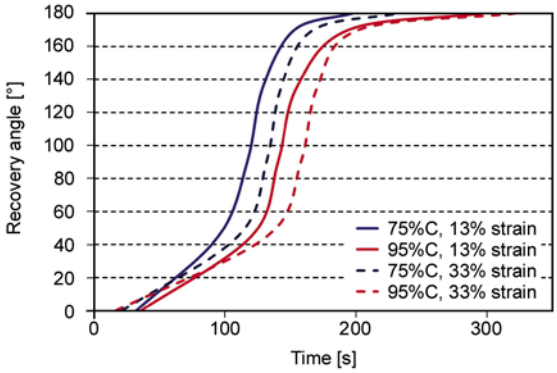

Figure 10. Recovery angle as a function of time for the UDG1200 SMPC. Different flexural strains and temperatures were used.

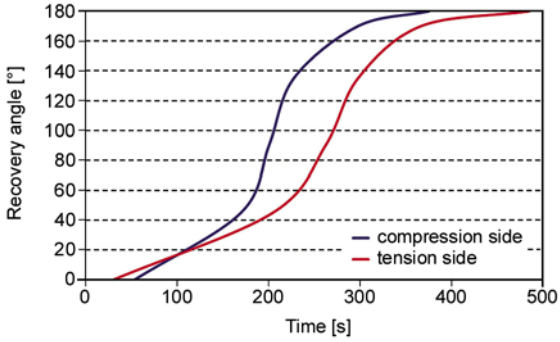

Figure 11. Recovery angle as a function of time for the TWC300 SMPC, with the reinforcement layer in the compressive side and in the tensile side of the specimen (temperature 75°C)

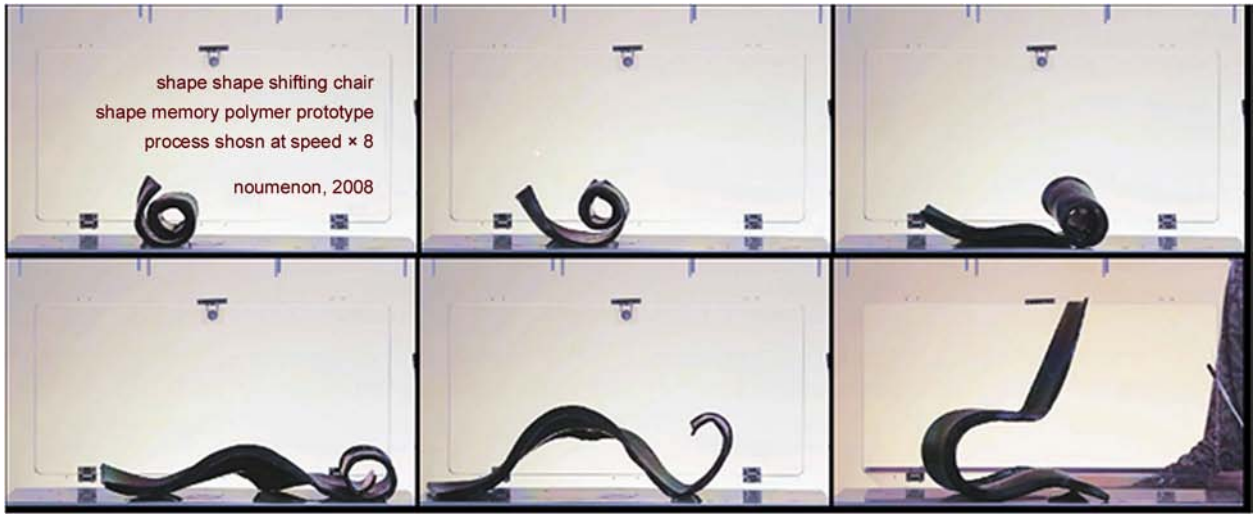

Figure 12. Shape recovery of a model chair (height 250 mm), made of UDG1200-Veriflex VF62

specimen. Similar observations were made by Zhang *et al.* [15]. An explanation for this difference has not been found. Moreover, the recovery stress is lower when the fabric is in the compressive side of the specimen.

The much higher recovery stress of SMPC has enabled the authors to produce a 250 mm high 'chair'. A single layer of UDG1200 was placed in an aluminium mould and the composite was manufactured using vacuum assisted transfer moulding. The permanent shape can be deformed to any temporary shape. Reheating using hot air results in shape recovery, as shown in Figure 12 (movie available in www.youtube.com/watch?v=GTLwExvDVVw). The recovery rate is very low, the full shape recovery takes almost 10 minutes. To obtain functional components, the recovery rate must be improved, by increasing the thermal or electrical conductivity.

4. Conclusions

This paper presented the first results of ongoing experimental work to determine the effect of fibre reinforcement on the transformation of a thermoset shape memory polymers. The following conclusions can be drawn:

- The recovery stress of the SMPC with unidirectional glass fibre reinforcement, loaded in bending, is 30 higher than for the neat SMP resin.
- The recovery stress is independent of the deformation temperature.
- The recovery stress is strongly affected by the degree of deformation.
- High deformation levels result in crazing (stress whitening). Even though the stress whitening disappears after reheating, it does influence the recovery stress.
- All composites tested show complete shape recovery. The SMP material is unable to recover the permanent shape against the forces of gravity.
- The rate of shape recovery is higher when the fibre reinforcement is loaded in compression.
- A model sized SMPC chair was successfully produced and the shape recovery was proved, although the recovery time was long.

References

[1] Van Humbeeck J.: Non-medical applications of shape memory alloys. Materials Science and Engineering A, **273–275** 134–148 (1989). DOI: 10.1016/S0921-5093(99)00293-2

[2] Ratna D., Karger-Kocsis J.: Recent advances in shape memory polymers and composites: A review. Journal of Materials Science, **43**, 254–269 (2008). DOI: 10.1007/s10853-007-2176-7

[3] Rousseau I.: Challenges of shape memory polymers: A review of the progress toward overcoming SMP's limitations. Polymer Engineering and Science, **48**, 2075–2089 (2008). DOI: 10.1002/pen.21213

[4] Takei S.: What is shape-memory polymer (in Japanese). in 'Development and application of shape memory polymers' (ed.: Irie M.) CMC, Tokyo, 10–88 (1989).

[5] Liu Y., Gall K., Dunn M., Greenberg A., Diani J.: Thermomechanics of shape memory polymers: Uniaxial experiments and constitutive modeling. International Journal of Plasticity, **22**, 279–313 (2006). DOI: 10.1016/j.ijplas.2005.03.004

[6] Zhang H., Wang H., Zhong W., Du Q.: A novel type of shape memory polymer blend and the shape memory mechanism. Polymer, **50**, 1596–1601 (2009). DOI: 10.1016/j.polymer.2009.01.011

[7] D'Hollander S., Van Assche G., Van Mele B., Du Prez F.: Novel synthetic strategy toward shape memory polyurethanes with a well-defined switching temperature. Polymer, **50**, 4447–4454 (2009). DOI: 10.1016/j.polymer.2009.07.021

[8] Meng Q., Hu J.: A review of shape memory polymer composites and blends. Composites Part A: Applied Science and Manufacturing, **40**, 1661–1672 (2009). DOI: 10.1016/j.compositesa.2009.08.011

[9] Koerner H., Price G., Pearce N. A., Alexander M., Vaia R. A.: Remotely actuatedpolymer nanocomposites-stress-recovery of carbon-nanotube-filled thermalplastic elastomers. Nature Materials, **3**, 115–120 (2004). DOI: 10.1038/nmat1059

[10] Ni Q-Q., Zhang C. S., Fu Y. Q., Dai G. Z., Kimura T.: Shape memory effect and mechanical properties of carbon nanotube/shape memory polymer nanocomposites. Composite Structures, **81**, 176–184 (2007). DOI: 10.1016/j.compstruct.2006.08.017

[11] Gall K., Dunn M., Finch D., Lake M., Munshi N.: Shape memory polymer nanocomposites. Acta Materialia, **50**, 5115–5126 (2002). DOI: 10.1016/S1359-6454(02)00368-3

[12] Gunes I., Cao F., Jana S.: Evaluation of nanoparticulate fillers for development of shape memory polyurethane nanocomposites. Polymer, **49**, 2223–2234 (2008). DOI: 10.1016/j.polymer.2008.03.021

[13] Lan X., Liu Y., Lv H., Wang X., Leng J., Du S.: Fiber reinforced shape-memory polymer composite and its application in a deployable hinge. Smart Material Structures, **18**, 024002/1–024002/6 (2009).
DOI: 10.1088/0964-1726/18/2/024002

[14] Gall K., Mikulas M., Munshi N., Beavers F., Tuppers M.: Carbon fiber reinforced shape memory polymer composites. Journal of Intelligent Material Systems and Structures, **11**, 877–887 (2000).
DOI: 10.1106/EJGR-EWNM-6CLX-3X2M

[15] Zhang C-S., Ni Q-Q.: Bending behaviour of shape memory polymer based laminates. Composite Structures, **78**, 153–161 (2007).
DOI: 10.1016/j.compstruct.2005.08.029

[16] Barrett R., Taylor R., Keller P., Codell D., Adams L.: Deployable reflectors for small satellites. in '21st Annual Conference on Small Satellites AIAA, Logan, USA' 1–9 (2007).

[17] Kasajima M., Ito K., Tsutsui M.: Stress-whitening phenomenon and relaxation behavior therefore (in Japanese). Bulletin of the Technical College of Hosei University, **18**, 33–48 (1982).

eXPRESS Polymer Letters Vol.5, No.3 (2011) 262–272
Available online at www.expresspolymlett.com
DOI: 10.3144/expresspolymlett.2011.26

High velocity impact and armour design

L. Iannucci[1], *D. Pope*[2]

[1]Imperial College, Department of Aeronautic, South Kensington, SW7 2AZ, London, UK.
[2]Defence Science and Technology Laboratory, Physical Sciences Department, Porton Down, Salisbury, Wiltshire, SP4 0JQ, UK.

Received 17 September 2010; accepted in revised form 16 January 2011

Abstract. Improving combat survivability is the most important aspect of military technology. Hence the development of new lightweight armour systems is a key requirement. A large number of new high performance polymer fibres have been developed in recent years, which include Aramid fibres, polyethylene fibres and polypropylene fibres, amongst others, and have been applied to soft armour systems.
To gain a fundamental understanding of which fibre type is the best for a specific application requires the development of techniques which can span all length scales. It has been widely recognised that multiscale modelling, which encompasses the full range of length and time scales, will be an important factor in the future design and testing of novel materials, and their application to armour design.
In the present paper a new material damage model suitable for the simulation of impact on thin laminated panels fabricated from high performance fibres is implemented into the commercial ls-dyna® finite element code. The new material model links the mesoscale behaviour of the individual fibres to the macroscale behaviour within a conventional shell finite element. The implemented model is used in a parametric high velocity study to illustrate the applicability of the model to the design of thin armour panels.

Keywords: *modeling and simulation, armour design, finite elements*

1. Introduction

A continued need exists for high performance, lightweight and cost effective protection for personnel and vehicles to improve survivability and reduce injury when subject to a range of potential threats e.g. blast and ballistic impacts. Protection or armour systems can be broadly divided into hard ceramic based systems, with high performance fibres within a composite backing; these are used for both personnel and vehicle armour, since they can be very effective at stopping ballistic projectiles by breaking and eroding them, and soft armour which use high performance composites to primarily prevent fragmentation incursion [1]. The advantages being these systems are very light, e.g. high performance polyethylene has a density less than water.

During the last 15 years a large number of new high performance polymer fibres with aligned carbon chains have been developed, which include Aramid fibres (Kevlar®, Twaron®), polyethylene fibres (Dyneema®, Spectre®) and polypropylene fibres (Curv®, Tegris®). Hence a reliable technique is a requirement to enable ranking of potential solutions and to determine the most effective combination of fibres for specific threats.

The classic understanding of how soft ballistic armour functions assumes that the impact energy can be dissipated by waves propagating along the fibres and hence the controlling materials properties

*Corresponding author, e-mail: l.iannucci@imperial.ac.uk

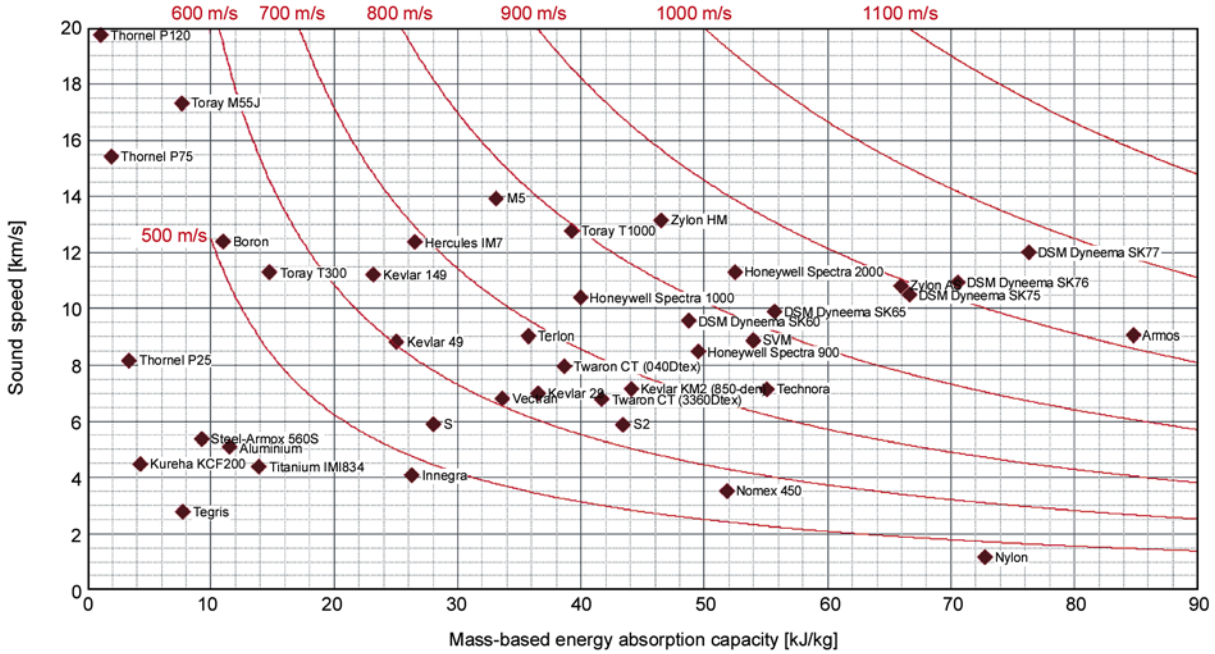

Figure 1. Sound speed vs. mass-based energy absorption capacity for a number of high-performance fibres [2] superimposed with Cunniff's *U** velocity [3]

are the tentsile wave velocity in the fibres and the specific energy absorbed at failure, this makes high performance fibres particularly attractive in impact protection systems and containment devices, this is schematically shown with the most common high performance fibres in Figure 1.

The modelling of ballistic impact onto panels composed of high performance fibres can be divided into semi-analytical and numerical based techniques. The most common analytical based technique, which is often used to scale impact and hence determine the ballistic performance of different panel thicknesses was developed by Cunniff [3]. Figure 1 is often used to determine the 'best' fibre for a soft armour system in Cunniff's approach (e.g. the highest dimensionless velocity), however, in this selection the assumption is implicit that the fibres are uniformly loaded; the failure response is linear from the ultimate strength of the fibre to rupture of the fibre with no plasticity assumptions, associated with the low compressive strength and unloading prior to complete failure. The non-linear shear response is also not considered. Despite these drawbacks the approach has found success. However, some exemptions have been noted, for example brittle systems based on carbon and Tegris. The inclusion of rate effects and phase change in the material is also a conceptually a difficult task to incorporate into such an approach. An alternative methodology is to use hydrocodes, e.g. ls-dyna® or abaqus® which includes the full constitutive relationship. An excellent review of numerical approaches is discussed in Grujicic *et al.* [4] and includes a multi-scale strategy based on Dyneema UD®. However, the non-linear shear response is also not considered. The importance of this behaviour is further discussed in section 3.0.

It has been widely recognised that the advent of multiscale modelling, which encompasses the full range of length and time scales, will be an important factor in the future design and testing of novel materials [4]. In the present approach the methodology adopted by Cunniff is incorporated within a numerical finite element framework with enhancements associated with the physical behaviour of the material, specifically the non-linear shear and compressive behaviour.

2. Laboratory tests

A series of laboratory tests were performed on Dyneema UD composites fabricated from Dyneema UD tape, which has a lamination of 0/90/0/90 and a typically thickness of the order of ~270 μm. The Dyneema UD composite fabricated from the tape usually has a very low shear and compressive strengths, while the tensile strength and strain to failure are excellent for a polymer. However, the measured composite laminate properties are not

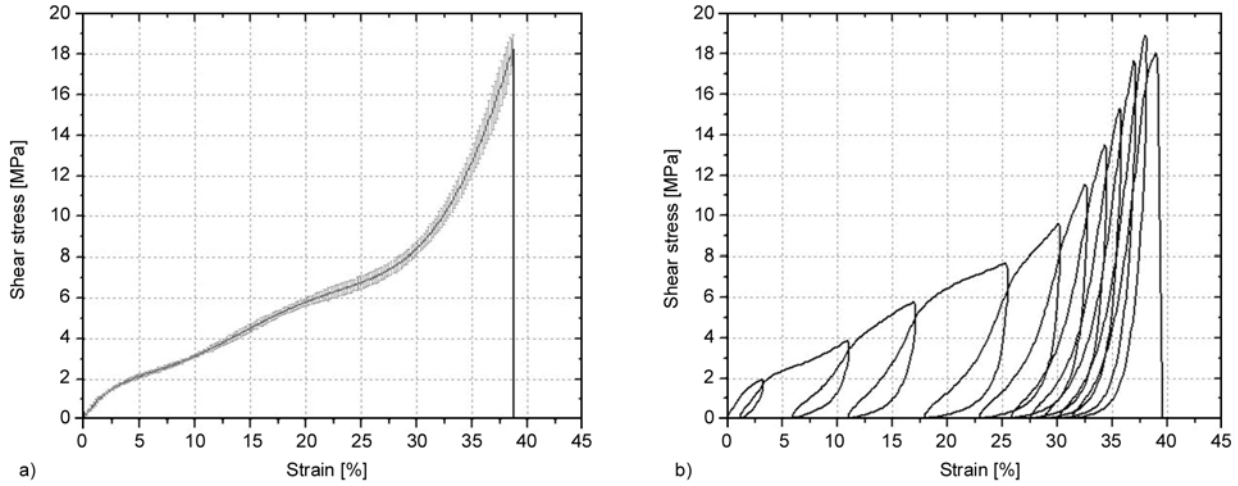

Figure 2. Tension-shear stress strain curve for Dyneema UD composite [5]: a) Increasing load until failure; b) Cyclic load/unload until failure

used in the following model, only tensile fibre stiffness and strength available in the open literature. To investigate the non-linear shear response a series of tests [5] were performed in a standard tension-shear configuration to investigate the behaviour in pure in-plane shear. This is a necessary parameter for the proposed model. These tests were carried out following the BS EN ISO 14129:1998 standard. All tests were performed on specimens with a width of 25 mm, a thickness of 5 mm and a length of 250 mm (150 mm gauge length) with a lamination of ±45° as stated in the standard. A specimen width to thickness ratio (w/t) of 2.5 was selected to ensure that the edge effect was minimal.

Figure 2a illustrates the non-linear shear with the error bars associated with the scatter in three tests. Figure 2b illustrates the cyclic unloading behaviour. A highly non-linear behaviour during unloading is observed this is potentially due to matrix damage, viscoplastic effects and the friction between the failed surfaces. This is clearly evident in Figure 3.

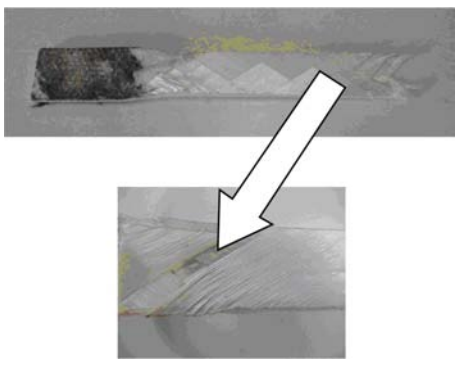

Figure 3. Failed tension-shear specimens (most layers have delaminated as can be seen from the lower figure)

As the fibres re-orient towards the end of the loading regime the stiffening response of the specimen is potentially associated with fibre reorientation.

Failure appeared to initiate from the grips, generating a series of fracture (delaminations and matrix cracking) surfaces along the specimen in a cone shaped pattern. A final series of static tests were performed to investigate the compressive behaviour [5]. In the present study the BS EN ISO 14126:1999 was used for the compressive test. The stress strain relationship is shown in Figure 4. The compressive behaviour is dominated by microscale kinking of the fibres. The initial peak is probably associated with their formation, followed by a plateau regime in which the kinks slide as more or less constant stress. Thus in the following modelling section it is proposed to model the compressive behaviour as an elastic-plastic material along fibre directions only with a typical strength of 8 MPa.

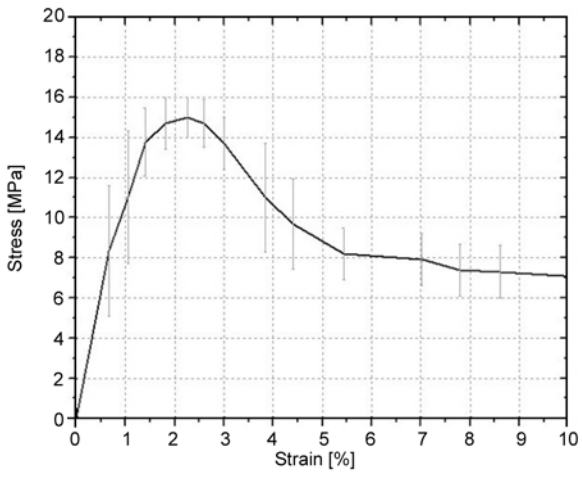

Figure 4. Compression test: stress versus strain relationship

Table 1. Summary of experimental results from high velocity gas gun testing

Testing regimes	Projectile used	Mass of projectile [g]	Velocity range [m/s]	Areal density [kg/m^2]	Ballistic limit [m/s]
0.8 mm Dyneema UD panels (100 mm×100 mm)	6 mm Mild Steel ball	0.8677	305–388	5.7	305

Figure 5. Ballistic impact on Dyneema UD crossply laminate near the ballistic limit: a) Side view of specimen; b) Rear view of specimen

A series of impacts were also performed on Dyneema UD crossply laminates [5] to determine the ballistic limit and to use the results to validate the proposed constitutive model, Table 1. The Dyneema samples were mounted on a frame, with lightly clamped edges, which allowed the material to draw, i.e. no bolts or rigid clamps were used. Figures 5a and 5b show the panel near the ballistic limit. The excessive displacements and drawing of the laminate is clearly evident. The deformation pattern would indicate a very low shear and compressive strengths. This has been confirmed from the static test conducted.

3. Model development

An elegant analytically based procedure was developed by Cunniff [3] to determine the V_{50} of an armour system. The key properties proposed by Cunniff for an armour system were;

the presented area and mass for the projectile;
the fibre sonic wave speed;
the fibre fracture toughness for the fibre.

The dimensionless ratios for the system and defined by Cunniff were:

σ – Fibre ultimate axial tensile strength
ε – Fibre ultimate tensile strain
ρ – Fibre density
E – Fibre modulus (assumed linearly elastic)
A_p – Projectile presented area
A_d – System areal density
m_p – Projectile mass
V_{50} – V_{50} ballistic limit (the velocity at which impacting projectiles are expected to defeat a system 50% of the time)
U^* – The product of fibre specific toughness and fibre strain wave velocity.

This leads to the Equations (1) and (2), which can be used to determine the V_{50} of an armour system, if the fibre type is known.

$$\Phi = \left(\frac{V_{50}}{(U^*)^{1/3}} \middle| \frac{A_d A_p}{m_p} \right) \tag{1}$$

where

$$U^* = \left(\frac{\sigma \varepsilon}{2\rho} \right) \sqrt{\frac{E}{\rho}} \tag{2}$$

the product of the fibre specific toughness and fibre strain wave velocity.

Cunniff developed the so called 'U^*' parameter to predict ballistic impact resistance in fibres. The model has been generally successful in predicting performance for a wide range of fibre/textile materials.

This paper describes the use of an existing model developed for low velocity impacts, which was implemented into the explicit FE code LS-DYNA, however, a number of key modification were necessary to allow for a realistic behaviour [6]. The formulation is concerned primarily with in-plane failure of thin high performance laminated UD composites. In the present paper it is compared with experimental results for a thin Dyneema UD com-

posite, however, it can be used for any high performance system. The inherent assumption follows the bilinear assumption in Cunniff paper, but includes plasticity and a non-linear shear response, which are both important. In the present formulation two damage variables are introduced to model the observed fibre damage. Compression failure is model with two plastic strain measures. The shear response follows a non-linear behaviour. Unloading always follows the elastic unloading slope before damage commences, but unloads with the damaged modulus when damage has initiated. Again, this is a convenient assumption, which captures the non-linear elastic and permanent strain behaviour. The fracture process is implicit within the stress-strain relationship for the composite material. The damage mechanics methodology must hence be based on a Unit Cell (UC), unlike classical fracture mechanics.

3.1. Stiffness degradation

Each Unit Cell (UC) consists of a 0 and 90 UD high performance ply; basically a cross-ply. Using a simple mosaic modelling approach it is possible to derive the cross-ply stiffness in each local direction within the unit cell, i.e. 0 and 90 layer.

Figure 6 illustrate a typical Dyneema cross-ply layer with the 0 degree layer removed. The ridges relate to the resin tracks. Note the low apparent resin; this is typical for a composite system in which the volume fracture of resin may be ~15%. Hence for the local x and y-fibre directions and assuming the fibre stiffness dominates the ply stiffness: The modulus and its degradation can be expressed by Equations (3) and (4):

$$E_{11} = 0.5(V_f E_f)(1 - d_1) \tag{3}$$

$$E_{22} = 0.5(V_f E_f)(1 - d_2) \tag{4}$$

with the following definitions;

d_1 = tensile failure in x direction fibre,

d_2 = tensile failure in y direction fibre,

E_f = Young's Modulus of fibre,

V_f = Volume fracture of fibre.

The damage parameters relate to the degradation of the fibres in the 0 and 90 layers within the unit cell in tension only. The fibre modulus is assumed constant and has been taken from the open literature [8]. The introduction of rate and temperature effects

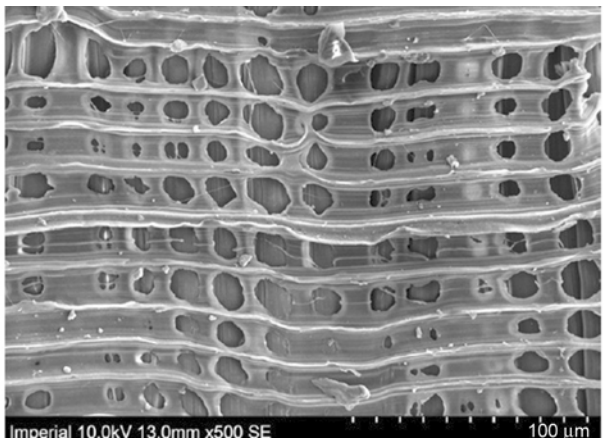

Figure 6. Interlaminar voids in Dyneema UD composites [7]

[11–13] into the model can also be achieved, however, a relationship between rate and temperature needs to be developed as does a technique to determine adiabatic heating effects, and the corresponding change in stiffness, strength and fracture energy.

A simple non-linear shear stress-strain behaviour is assumed for the in-plane shear response. The shear stress-strain response is defined by Equation (5):

$$\tau = A\gamma^3 + B\gamma^2 + C\gamma + D \tag{5}$$

where D = 0.0, C = 109.61, B = –580.424, A = 1120.77 in units of MPa for the curve shown in Figure 2a. A simple least square fit was used to derive the constants from the experimental curve. The instantaneous shear modulus can be trivially derived using the above equation. Since the modelling approach uses shell element only, with no delamination between plies. The non-shear shear response must include all possible shear failure modes; hence degradation associated with delaminations must be included implicitly within the response. These delaminations can be clearly seen in Figure 3, which results in the curve shown in Figure 2a, and the progression of damage in Figure 2b.

3.2. Fibre fracture evolution

Failure in both the 0 and 90 directions is formulated in a similar manner. No cross coupling between 0 and 90 failure is included within the constitutive model. Once the initiation (failure) stress is reached damage initiates and stress is gradually reset to zero in either the 0 or 90 direction as damage reaches a value of one. Therefore element deletion could be used to represent a physical tear in the laminate, if

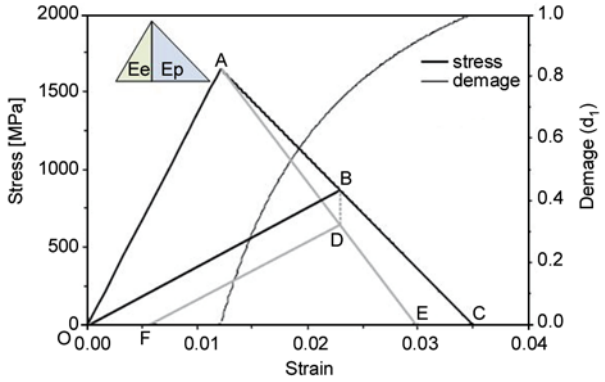

Figure 7. Assume stress-strain response for high performance fibre. OAE relates to a response with permanent strain, unloading would then follow OADF [6]

damage reaches one in either the 0 or 90 directions for all integration points within the element (i.e. all laminae layers have failed). For the 0 and 90 fibre fracture case (i = 1, 2), the damage evolution equation is defined as, OAC in Figure 7, when no permanent strain is present, and unloading between BO for any damage d (Equation (6)):

$$d_{\mathrm{i}} = \frac{\varepsilon_{\max,\mathrm{i}}}{(\varepsilon_{\max,\mathrm{i}} - \varepsilon_{0,\mathrm{i}})}\left[1 - \frac{\varepsilon_{0,\mathrm{i}}}{\varepsilon_{\mathrm{ii}}}\right] \tag{6}$$

where $\varepsilon_{\max,\mathrm{i}}$ is the strain at zero stress and damage = 1, and ε_0 is the strain at maximum stress (failure stress) and damage = 0. The only parameters required for this evolution model are these two strain constants, which define the total energy dissipated, i.e. the area under the stress-strain curve. Equation (5) can be converted into an incremental form, which has been implemented into the LS-DYNA code and is stated by Equation (7):

$$\Delta d_{\mathrm{i}} = \frac{\varepsilon_{\max,\mathrm{i}}}{(\varepsilon_{\max,\mathrm{i}} - \varepsilon_{0,\mathrm{i}})}\left[\frac{\varepsilon_{0,\mathrm{i}}}{\varepsilon_{\mathrm{ii}}^2}\right]\Delta\varepsilon_{\mathrm{ii}} \tag{7}$$

The constants, $\varepsilon_{\max,\mathrm{i}}$ and $\varepsilon_{0,\mathrm{i}}$ must be chosen to prevent a mesh dependent solution by maintaining constant energy dissipation independent of volume, which corresponds to a physical element size, i.e. $\varepsilon_{\max,\mathrm{i}}$ must be altered at an element level. This is easily input as a parameter at an element level, or calculated within the element subroutine based on the element volume. The damage evolution can then be trivially stated as Equation (8):

$$d_{\mathrm{i}}^{\mathrm{n}+1} = d_{\mathrm{i}}^{\mathrm{n}} + \Delta d_{\mathrm{i}}^{\mathrm{n}+1} \tag{8}$$

where 'n' represents the n^{th} timestep or load increment.

Examination of Figure 7 reveals that the basic shape follows the assumptions in Cunniff's model. Clearly to include plasticity it is necessary to offset the unloading curve by an appropriate amount so that it unloads prior to the origin, i.e. DF. The offset BD relates to an irreversible damage constant which is described in the next section.

3.3. General plane stress stress-strain-damage relationship

The general plane stress stress-strain relationship for the damage model can be derived directly from Hooke's law. A general form could be described by Equation (9) and can be expanded into incremental form to include a permanent or damage strain component. The magnitude of the permanent damage strain can be determined via the material constant β.

$$\dot{\boldsymbol{\sigma}} = C\dot{\boldsymbol{\varepsilon}} + \beta\dot{C}\boldsymbol{\varepsilon} \tag{9}$$

The permanent damage strain would result in a permanent fix if unloading occurs prior to failure. Hence to determine the β constants it is necessary to perform such tests, unfortunately such dynamic tests would be very difficult to achieve and static unloading may be the only appropriate test.

Cross-coupling and interaction terms are not considered in the present formulation [6]. The stress-strain-damage relationship is hence defined by Equations (10) and (11):

$$\dot{\boldsymbol{\sigma}} = C\dot{\boldsymbol{\varepsilon}} + \dot{\boldsymbol{\sigma}}_{\mathrm{ir}} \tag{10}$$

where

$$\dot{\boldsymbol{\sigma}}_{\mathrm{ir}} = \begin{pmatrix} -\beta_1\sigma_{11}\dfrac{\dot{d}_1}{(1-d_1)} \\ -\beta_2\sigma_{22}\dfrac{\dot{d}_2}{(1-d_2)} \\ 0 \end{pmatrix} \tag{11}$$

The β_{i} terms in the above equation control the amount of residual permanent strain (plastic strain). Consider the unloading point B in Figure 7; with β_{i} = 1.0 the unloading path is directly to the origin with no residual plastic strain, while a value of $\beta_{\mathrm{i}} > 1.0$ result in a positive residual plastic strain, i.e. path BDF, as the strain softening line AC has now moved to a position AE to accommodate the additional stress reduction. A value of $\beta_{\mathrm{i}} < 1.0$ is not permitted, as this would indicate an unrealistic neg-

ative permanent strain. In the present formulation for the irreversible stress, $\dot{\sigma}_{ir}$, second order terms are neglected.

3.4. Work dissipated

Work dissipation is included in the implementation for information only and is not directly used within the stress update procedure. The work dissipated $\dot{W}_i$ for a damage rate $\dot{d}_i$ is given by Equation (12) [6]:

$$\dot{W}_i^n = \frac{(2\beta_i - 1)}{2} \frac{\sigma_{ii}^2}{E_{ii}^0(1 - d_i)^2} \dot{d}_i^n \tag{12}$$

where 'n' denotes the n^{th} time step or load increment, and E_{ii}^0 relates to the undamaged modulus.
Clearly the total energy dissipated can be predicted for a specific volume of material. This can be used to understand which regions are dissipating the most energy, or power. Hence different fibres could be used in different layers depending on the energy dissipated.

3.5. Permanent plastic strain

The total strain is the sum of permanent (plastic) and elastic strain. From the stress-strain curve, it can be shown that the plastic strain (OF) in the tensile case, Figure 7, is given by Equation (13) [6]:

$$\dot{\varepsilon}_{pl,i} = (\beta_i - 1) \frac{\sigma_{ii}}{E_{ii}^0(1 - d_i)^2} \dot{d}_i \tag{13}$$

the cumulative permanent strain is trivially defined by Equation (14):

$$\varepsilon_{pl,i}^{n+1} = \varepsilon_{pl,i}^{n} + \Delta\varepsilon_{pl,i}^{n+1} \tag{14}$$

where 'n' represents the n^{th} timestep or load increment. Figure 7 illustrates the bilinear constitutive model where AC relates to $\beta_i = 1$ and AE when $\beta_i > 1$. The greater the value of β_i, the greater the magnitude of the irreversible stress BD, and hence the permanent strain OF. The 'plastic strain' that is defined in this paper results from incomplete closure of cracks and potential fibre damage formed during damage evolution. It is clear that the β_i constants can be derived from experimental cyclic permanent strain versus damage plots.

3.6. Damage evolution for compressive direct stresses

In the present formulation, compression failure is modelled in a simple elastic perfectly plastic manner. The local x and y fibres have their own plastic strain component and are completely uncoupled. Figure 6 would indicate that this type of modelling approach seems appropriate due to the lack of resin. The fibres would tend to kink, but not fail. The relevant equations for compression for the local x and y fibre directions are given in Equations (15) and (16). No failure strain is applied.

$$d\varepsilon_i = d\varepsilon_i^e + d\varepsilon_i^p, \quad f = \sigma_i - \sigma_y \tag{15}$$

$$d\varepsilon_i^p = d\lambda \frac{\partial f}{\partial \sigma_i} \tag{16}$$

where $d\lambda$ is a proportional constant to maintain stresses on the compressive yield surface.

3.7. Smearing methodology

The modelling of tearing and fracturing in brittle materials is an inherently mesh dependent problem and was initially encountered, and solutions proposed in the Civil Engineering community [6].
The formulations described in the previous sections relate the energy dissipated within a unit volume to the fracture energy. Hence, it is necessary to relate this energy to the energy required to increase the fracture area or cracked surface. Since Finite Elements are volume based, it is convenient to link damage mechanics and fracture mechanics. Consider the bilinear implementation shown in Figure 7 (insert). The specific energy dissipated E_f can be subdivided into the elastic energy E_e and the propagation energy E_p. This leads to the following Equation (17):

$$E_f = E_e + E_p \tag{17}$$

The energy dissipated should be independent of mesh (finite element) size. If the specific internal energy is constant, the adjusted value of E_p can be determined for different mesh densities (finite element mesh size). For a bi-linear stress-strain-damage curve the specific energy can be defined by Equation (18):

$$E_f = \frac{1}{2} \sigma_0 \varepsilon_{max} \tag{18}$$

and for the individual energies within the bi-linear stress-strain relationship, Equation (19):

$$E_p = \frac{1}{2} \sigma_0 (\varepsilon_{max} - \varepsilon_0) \text{ and } E_e = \frac{1}{2} \sigma_0 \varepsilon_0 \tag{19}$$

This intralaminar fracture energy, which is a fracture mechanics based quantity, can be related to the energy dissipated within the finite element volume by linked damage and fracture mechanics. Equation (19) illustrates the energy dissipated for a particular damage mode, Π, and the coupling between damage and fracture mechanics leads to Equation (20):

$$\prod = (E_e + E_p)Al_x = G_f A \text{ and } l_x = \frac{A_e}{l} \quad (20)$$

where

A_e = shell area (mesh parameter),
A = fracture area (mesh parameter),
G_f = intralaminar fracture energy (material property),
l = longest length (mesh parameter),
l_x = characteristic length (mesh parameter).

No minimum element size restriction applies when using Equation (20), except it is desirable that the element size should be equal or greater than the process zone in a particular damage mode, however, a restriction does exist for the maximum element size used in the mesh. Re-arranging Equation (20) and using Equation (19) yields the following inequality, defined by Equation (21):

$$l_x < \frac{2G_f}{\sigma_0 \varepsilon_0} \quad (21)$$

This inequality prevents a snap through stress-strain behaviour, i.e. a negative E_p. The issues associated with the determination of the failure strain ε_{max} are discussed in a later section.

4. High velocity impact model

The Unit Cell (UC) represents the behaviour of a cross ply composite. Hence its implementation into a shell element required each integration point to be associated with the UC. For example, if 100 0/90 cross ply are used in the laminate, then 100 integration point should be used to model the macroscale behaviour from the UC mesoscale model. In the present example the experimental results presented in Table 1 are simulated. However, to understand the behaviour of the model for different materials a parameter study is performed with the properties in Table 2. The fracture toughness per unit mass was assumed the same for all high performance fibres listed. The strain at fracture is assumed for Kevlar and Nylon to make the fracture toughness the same for all composites. This is a simple assumption to illustrate the applicability of the model. The non-linear shear and compressive behaviour are assumed the same and only the initial stiffness and UTS are altered. This assumption assumes the resin properties and failure would control the shear and compressive response. For a very low resin system this would probably be the case.

Table 2. High Performance fibre properties used in study

Fibre type	Density [g/cm^3]	UTS [GPa]	Strain at fracture [%]	E [GPa]
Nylon	1.12	0.90	14.6	9.6
Kevlar	1.44	2.50	6.8	71.0
Dyneema	0.97	3.00	3.8	116.0

4.1. High velocity impacts on Dyneema UD

The laboratory impacts described in Section 2. are modelled using the techniques described in section 3. The projectile is modelled with an elastic plastic material model and the specimen modelled with the new material model. Contact logic is applied at all interfaces between the test rig and the composite and the projectile and the composite. The predicted deformed pattern exhibits the key feature, such as the excessive drawing of the material and the very large displacement prior to perforation.

Figure 8 indicates the behaviour well above the ballistic limit. Element deletion occurs when either the 0 and 90 laminae within the UC has failed. Clearly modelling the tensile, compressive and shear behaviour was key in simulating the correct response. If the impact velocity is reduced towards the ballistic limit the behaviour follows Figure 9. This clearly appears to give the same drawing pattern as the test. The ballistic limit was also approximately the same.

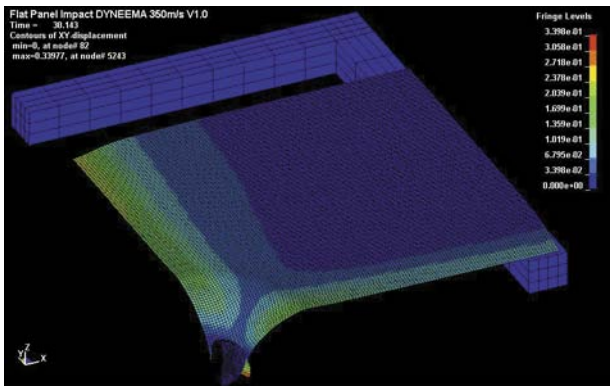

Figure 8. Ballistic impact (350 m/s above ballistic limit) using Dyneema laminate. XY displacement plot.

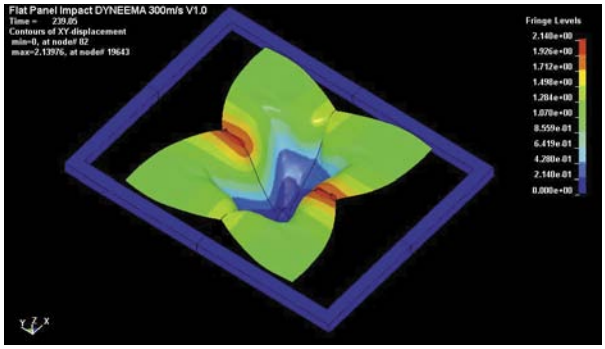

Figure 9. Ballistic impact (300 m/s at ballistic limit) using Dyneema laminate. XY displacement plot.

However, the stiffness and strength are based on the fibre values only!

4.2. High velocity impacts on other high performance UD materials

The model is applied to a hypothetical Kevlar material with realistic fibre stiffness and strength. The procedure used for the Dyneema is repeated and the ballistic limit determined. The velocity at 350 m/s is shown in Figure 10. The final ballistic limit was found to be between 200–250 m/s, considerably lower than the Dyneema.

To confirm the behaviour was realistic the analyses was repeated for Nylon. The behaviour is shown in Figure 11. Clearly the drawing behaviour is different; however, the same energy and shear behaviour were used. This would indicate that the fibre stiffness and strength are the important parameters and confirms Cunniff original assumptions. The ballistic limit was again considerably below that of Dyneema.

High performance fibre test results are generally available in the open literature, for example in [8, 9]. These tests are normally conducted on fibres

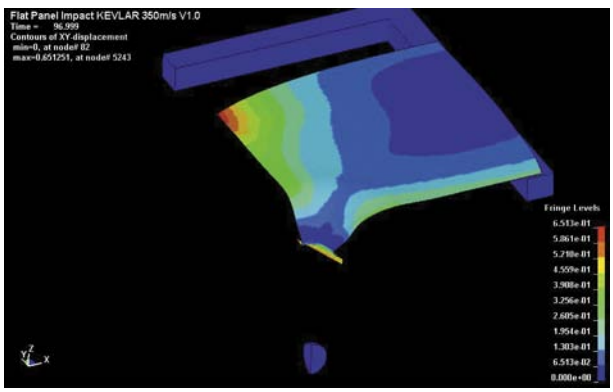

Figure 10. Ballistic impact (350 m/s above ballistic limit) using Kevlar laminate. XY displacement plot.

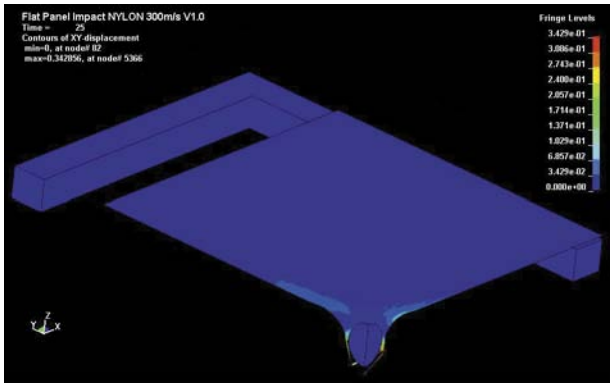

Figure 11. Ballistic impact (300 m/s above ballistic limit) using Nylon laminate. XY displacement plot.

with yarns, typically 300 fibres or greater, hence the stress in calculated based on the number and cross-section area of these fibres. The strain is usually determined via a contactless video device between two known gauge points, perhaps several centimetres apart, while for the dynamic tests several millimetres, a requirement for the dynamic tests to achieve equilibrium. Examination of the failure mechanisms clearly indicates a weakest link type failure with individual fibres failing within the gauge length, thus generating a fluffy appearance. Thus no clear fracture surface is evident, which is what would normally be expected for carbon and glass based systems using a brittle matrix. Thus, how is the strain at fracture, which could be between A and E in Figure 7, determined for these materials? For brittle composite systems it can be relatively easily determined by performing additional fracture mechanics type tests [10] to determine the fracture energy, and if the strength is known the ultimate fracture strain can be determined for the material model. For fibre tests, a variation in the failure stress is observed and is generally a function of the number fibres in the yarn, and the gauge length [9]. This is usually modelled via a Weibull type approach on the strength, however, details on the variation of the failure strain and hence total fracture energy absorbed is not available in the open literature. This does pose the problem whether a probabilistic type approach should be adopted since each Finite Element has a finite volume, hence with the use of a Weibull distribution and Monte-Carlo type simulations such an approach could be adopted. This poses the question on which representative volume should be used for such an analysis. Returning to the original question

on how to select the appropriate failure strain this should be taken from Hopkinson bar tests for the anticipated strain rates. The static test results cannot generally be used for reasons associated with strain-rate, visco-elastic effects, etc. but more importantly since the tests are conducted at static strain rates once localisation and failure occurs in individual fibres, elastic strain energy stored in the remaining broken fibres elastically unload almost immediately causing an abrupt unloading on the measured gauge displacement. This unloading process is restricted in the dynamics test, since at the higher strain rates the unloading wave take a finite time to relaxes the fibre, thus measuring the familiar triangular or half sine wave shaped stress-strain curve as the force is recovered from the bars, not directly at the specimen. This is well illustrated in [9].

5. Conclusions

The modelling approach appears to confirm the originally assumptions developed by Cunniff in his paper. The advantage of using numerical techniques is that it allows the contact logic inherent within most Finite Element codes to model different projectiles and their behaviour. Thus projectile area and shape are modelled explicitly.

The approach can also be used to understand the observed deviations of polypropylene performance from the established correlations to Cunniff original formulations. However, a robust methodology needs to be developed to determine the final failure strain to be input into the material model. Similarly to determine the residual plastic strain cyclic unloading tests would be required. Furthermore, the approach can be applied to the development of hybrid layers within an armour system. This could follow the natural process often found in nature, e.g. spider silks [14].

To model the actual hydrodynamic event at the point of impact the EOS must be included within the modelling approach [15]. As the model is presented it is most suitable for the rear part of a soft armour system were hydrodynamic effects are substantial smaller. Modelling the complete penetration including all damage mechanisms remains conceptually a difficult task with normal 3D Finite Element [16].

Acknowledgements

The support from the Dstl SAMPLE programme gratefully acknowledged.

References

[1] Jacobs M. J. N., Van Dingenen J. L. J.: Ballistic protection mechanisms in personal armour. Journal of Materials Science, **36**, 3137–3142 (2001). DOI: 10.1023/A:1017922000090

[2] Cwik T.: Survivability of structures to impact and blast loadings. Dstl/EPSRC progress report 1. Imperial Aeronautics Report E1 (2009).

[3] Cunniff P. M.: Dimensionless parameters for optimization of textile-based body armor systems. in '18th International Symposium on Ballistics Conference, San Antonio, USA' 1303–1310 (1999).

[4] Grujicic M., Arakere G., He T., Bell W. C., Glomski P. S., Cheeseman B. A.: Multi-scale ballistic material modeling of cross-plied compliant composites. Composites Part B: Engineering, **40**, 468–482 (2009). DOI: 10.1016/j.compositesb.2009.02.002

[5] Iannucci L., Pope D., Dalzell M.: A constitutive model for Dyneema UD. in '17th International Conference on Composite Materials, Edinburgh, United Kingdom' p.10 (2009).

[6] Iannucci L., Willows M.: An energy based damage mechanics approach to modelling impact onto woven composite materials – Part I: Numerical models. Composites Part A: Applied Science and Manufacturing, **37**, 2041–2056 (2006). DOI: 10.1016/j.compositesa.2005.12.013

[7] Greenhalgh E. S, Bloodworth V.: Fractographic assessment of dyneema composites under ballistic impact. Imperial Aeronautics Report, TR09/22/Cv1, (2009).

[8] Huang C., Chen S., Duan Z.: Experimental study on dynamic properties of high strength fiber clusters. Materials Science Forum, **475–479**, 1045–1050 (2005). DOI: 10.4028/www.scientific.net/MSF.475-479.1045

[9] Farsi B., Dooraki J. A., Nemes M., Bolduc M.: Study of parameters affecting the strength of yarns. Journal de Physique IV: Proceedings, **134**, 1183–1188 (2006). DOI: 10.1051/jp4:2006134180

[10] Laffan M. J., Pinho S. T., Robinson P., Iannucci L.: Measurement of the in situ ply fracture toughness associated with mode I fibre tensile failure in FRP. Part I: Data reduction. Composites Science and Technology, **70**, 606–613 (2010). DOI: 10.1016/j.compscitech.2009.12.016

[11] Peus T., Smets E. A. M., Govaert L. E.: Strain rate and temperature effects on energy absorption of polyethylene fibres and composites. Applied Composite Materials, **1**, 35–54 (1994). DOI: 10.1007/BF00567210

[12] Brooks N. W. J., Duckett R. A., Ward I. M.: Temperature and strain-rate dependence of yield stress of polyethylene. Journal of Polymer Science Part B: Polymer Physics, **36**, 2177–2189 (1998).
DOI: 10.1002/(SICI)1099-0488(19980915)36:12<2177::AID-POLB15>3.0.CO;2-X

[13] Govaert L. E., Peijs T.: Tensile strength and work of fracture of oriented polyethylene fibre. Polymer, **36**, 4425–4431 (1995).
DOI: 10.1016/0032-3861(95)96848-3

[14] Hinman M. B., Jones J. A., Lewis R. V.: Synthetic spider silk: A modular fiber. Trends in Biotechnology, **18**, 374–379 (2000).
DOI: 10.1016/S0167-7799(00)01481-5

[15] Anderson C. E., Cox P. A., Johnson G. R., Maudlin P. J.: A constitutive formulation for anisotropic materials suitable for wave propagation computer programs – II. Computational Mechanics, **15**, 201–203 (1994).
DOI: 10.1007/BF00375030

[16] Raimondo L., Iannucci L., Robinson P., Pinho S. T.: A numerical material model for predicting the high velocity impact behaviour of polymer composites. Computational Methods in Applied Sciences, **10**, 161–177 (2008).
DOI: 10.1007/978-1-4020-8584-0_8

eXPRESS Polymer Letters Vol.5, No.3 (2011) 273–282
Available online at www.expresspolymlett.com
DOI: 10.3144/expresspolymlett.2011.27

Structure, thermal and fracture mechanical properties of benzoxazine-modified amine-cured DGEBA epoxy resins

S. Grishchuk[1], *Z. Mbhele*[2], *S. Schmitt*[1], *J. Karger-Kocsis*[2,3*]

[1]Institut für Verbundwerkstoffe GmbH (Institute for Composite Materials), Kaiserslautern University of Technology, D-67663 Kaiserslautern, Germany
[2]Polymer Technology, Faculty of Engineering and the Built Environment, Tshwane University of Technology, Pretoria 0001, Republic of South Africa
[3]Department of Polymer Engineering, Faculty of Mechanical Engineering, Budapest University of Technology and Economics, H-1111 Budapest, Hungary

Received 18 November 2010; accepted in revised form 20 January 2011

Abstract. First, traditional diamine hardeners of epoxy resins (EP) were checked as potential accelerators for the benzoxazine (BOX) homopolymerization. It was established that the acceleration effect depends on both the type and amount of the diamine compounds. In the follow-up work amine-curable diglycidyl ether bisphenol A (DGEBA) type EP was modified with BOX keeping the EP/BOX ratio constant (75/25 wt.%). The amine hardeners, added in the EP in stoichiometric amounts, were of aliphatic and aromatic nature, viz. diethylenetriamine (DETA), 4,4′-diaminodiphenyl methane (DDM), and their 1/1 mixture. The thermal, viscoelastic, flexural and fracture mechanical properties of the EP/BOX hybrids were determined and compared to those of the reference EPs. Based on dynamic-mechanical thermal analysis and atomic force microscopy the formation of co-network between EP and BOX was concluded. Homopolymerized BOX was built in the network in nanoscaled inclusions and it was associated with internal antiplasticization. Incorporation of BOX improved the charring, enhanced the flexural modulus and strength, and reduced the glass transition of the parent EP. The fracture toughness and energy were not improved by hybridization with BOX.

Keywords: *thermosetting resins, benzoxazine, epoxy resin, fracture mechanics, morphology*

1. Introduction

Polybenzoxazines represent a rather new class of thermosets formed by ring-opening polymerization (ROP) of the benzoxazine (BOX), usually 1,3-benzoxazine precursors. Nowadays they are considered as most promising matrix materials for composites in future aerospace applications. This expectation is based on their excellent thermal properties (high glass transition temperature, T_g), low flammability (high char yield), high stiffness, low water uptake, and practically no shrinkage upon curing (e.g. [1–3]). As the curing of BOX occurs via ROP no volatile by-products appear which supports the production of void-free composites. A further benefit in linked with the easy synthesis of BOX, the monomers of which may be very versatile. Versatility is given by the fact that beside the necessary formaldehyde various phenol and amine compounds may be selected for the synthesis of BOX. On the other hand, the thermally-induced polymerization of BOX takes place at rather high temperature ($T > 200$°C) which is hardly acceptable by the praxis. A further problem, early recognized [4], is that the crosslink density of polybenzoxazine is surprisingly low considering its high stiffness and T_g when comparing with other thermosets of similar

*Corresponding author, e-mail: karger@pt.bme.hu

properties. This was explained by massive H-bonding occurring between the phenolic –OH and tertiary amines of the Mannich linkage formed via ROP in BOX ([1–3,5 and references therein]). Though the development of BOXs followed different directions in the past two decades [2–3, 5–6], the reduction of the temperature of polymerization (curing) and the increase of the crosslink density remained always top priority issues.

The ROP of BOX can be catalyzed by both basic and acidic compounds. In the open literature lots of different compounds have been checked in respect to their potential catalytic activity, whereby emphasis was put mostly on acidic compounds [1, 7]. Markedly less works were devoted to the potential acceleration effect of basic compounds, and especially those of amine-group containing ones, on the BOX polymerization. The latter is, however, of paramount importance when the increase of the crosslink density of polybenzoxazines is targeted by coreactions (copolymerization, co-crosslinking) with epoxy resins (EPs). Recall that amines are the usual hardeners of low temperature curable EPs.

To increase the crosslink density of BOXs by co-crosslinking with EPs was always a favored research direction. In their pioneering work Ishida and Allen [4] prepared BOX/EP 'copolymers' by exploiting the reaction between the phenolic groups (–OH) of the ring-opened BOX and epoxy (oxirane) groups of the EP. Accordingly, no external EP curing agent (hardener) has been used to prepare the EP/BOX hybrids. The corresponding hybrids showed enhanced T_g, high crosslink density and ductility over the BOX homopolymers. The above reaction pathway, i.e. BOX as hardener for EP, was addressed by other researchers studying the related mechanisms [8–9] and the effects of the chemical build-up of the components [8]. Amine compounds may have an acceleration effect (thermal kick-off) on the BOX polymerization as demonstrated by Kimura *et al.* [10]. Recently, amine curable EP resins were also modified with BOX. Rao and Pathak [11] used phenalkamine as EP curing agent and concluded that the reactions between EP and BOX occur in two-steps. At low temperature the EP reacts with the amine, whereas at high temperature the ROP of BOX is immediately followed by co-crosslinking reactions occurring between the phenolic –OH (BOX) and epoxy groups (EP). A two-step reaction was proposed also for a special BOX end capped EP cured by aromatic diamine (diamino diphenyl sulphone) [12]. In a very recent paper Agag *et al.* [13] reported on the preparation of primary amine-functionalized BOXs and their curing. The differential scanning calorimetric (DSC) thermogram of the primary amine-functionalized BOX showed multiple exotherms above the melting and below the polymerization temperature of the corresponding BOX compound, which can only be assigned to reactions between the oxazine and primary amine ($–NH_2$) groups.

Considering the fact that primary diamines are the usual hardeners for low temperature curable EPs, it is straightforward to check their effects on the BOX polymerization. This has been done in the present work by selecting some amine hardeners with aliphatic, cycloaliphatic and aromatic backbones. A further aim of this work was to prepare BOX modified amine cured EPs and to study their structure-property relationships.

2. Experimental

2.1. Materials

As potential accelerators for the BOX homopolymerization the following diamines have been selected: diethylenetriamine (DETA), 4,4′-diamino-3,3′-dimethyl-dicyclohexylmethane (Aradur® 2954 of Huntsman Advanced Materials, Basel, Switzerland), and 4,4′-diaminodiphenyl methane (DDM). DETA (melting and boiling temperatures –39 and 207°C, respectively) and DDM (melting temperature: 92°C) were procured from Sigma-Aldrich Chemie GmbH (Taufkirchen, Germany). Note that all of them are widely used EP hardeners. Moreover, due to their structure (aliphatic, cycloaliphatic and aromatic) the primary amines have different basic characters.

As bifunctional, diglycidyl ether bisphenol A based EP resin D.E.R. 331 (Dow Deutschland Anlagengesellschaft mbH, Schwalbach, Germany) was selected. This EP has the following characteristics: epoxy equivalent weight: 182–192 g/eq., viscosity and density at T = 25°C 11–14 Pa·s and 1.16 g/ml, respectively. The BOX used was an N-phenyl bisphenol A based 1,3-benzoxazine (Araldite MT 35600 CH of Huntsman Advanced Materials). This

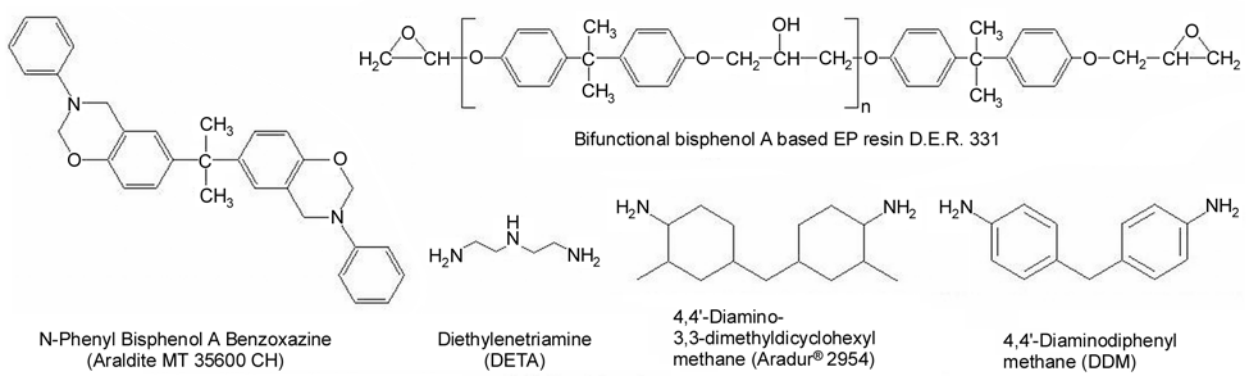

Figure 1. The chemical structures of the materials used

BOX with a density of 1.18 g/ml at *RT* has a melting range of 80–85°C, and a viscosity range between 80 and 180 mPa·s at $T = 125$°C.
The chemical structures of the materials used are depicted in Figure 1.

2.2. Sample/specimen preparation

To check the potential acceleration effect of the amines they were added in 10 and 20 wt.%, respectively, to the powdered BOX followed by mixing in a mortar. The BOX/amine mixes were left for 24 h prior to their DSC testing. As demonstrated later by showing the related dynamic DSC scans the amine affected the homopolymerization of BOX differently. Based on the results two amines, viz. DETA and DDM along with their 1/1 mixture (molar ratio) were selected for the EP hardening. As the reactivities of DETA and DDM are very different both towards EP and BOX, our interest was to check their combination for which the DETA/DDM = 1/1 has been selected. The EP/amine ratio was stoichiometric in all recipes. Though the BOX reacts with both the amine compounds (see later) and EP (as disclosed above), it was considered as an inert material. The EP(including hardener)/BOX ratio was fixed at 75/25 wt.%.
The samples were prepared as described below. First, the EP was warmed to 70°C and kept for 30 min in order to melt the eventually crystalline fraction. Next, the powdered BOX was added to the warm EP and mixed thoroughly (1900 revolutions per minute, rpm) for 5 min. The mix was placed in a thermostatic oven and stored at $T = 110$°C for 40 min to dissolve the BOX. Afterwards the amine was introduced by mixing (160 rpm) for 4 min. Finally, the mixture was deareated *in vacuo* and poured in open molds manufactured from polytetrafluoro ethylene (PTFE). The PTFE molds contained the cavities of the rectangular bars and compact tension (CT) specimens used for testing (see later). The cure cycle (temperature vs. time) of the samples is depicted in Figure 2. Curing of the resins according to Figure 2 occurred in a programmable thermostatic oven of Kendro Laboratory Products (Langenselbold, Germany).

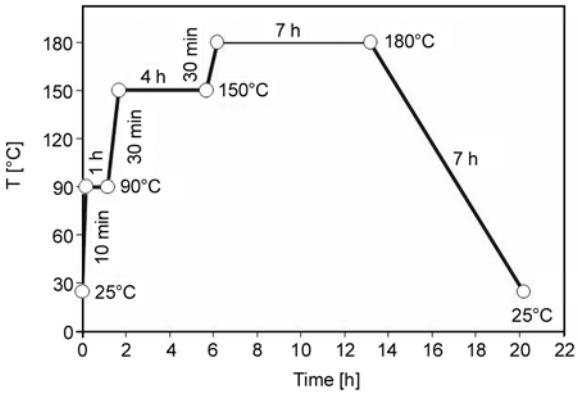

Figure 2. Cure cycle of the EP and EP/BOX hybrids

Thermal and viscoelastic properties

A DSC 821e (Mettler Toledo, Giessen, Germany) thermal analyzer was used to investigate the BOX homopolymerization in presence and absence of the various diamines listed before, and to detect the T_g of the EP/BOX hybrids prepared. DSC thermograms were registered in the temperature range from $T = 0$ to 300°C at a heating rate of 10°C/min under N_2 flushing (30 ml/min). The sample weight varied between 10 and 20 mg.
Dynamic mechanical thermal analysis (DMTA) was taken on rectangular specimens (60 × 8 × 4 mm^3; length × width × thickness) in three point bending configuration (span length: 50 mm) at 1 Hz using a DMA Q800 of TA Instruments (New Castle, DE, USA). Tests were performed at a constant

amplitude (50 μm) using sinusoidal oscillation and under dynamic conditions in the interval T = –100…300°C at a heating rate of 1°C/min.

The hybrid resins were subjected to thermogravimetric analysis (TGA) in a DTG-60 device of Shimadzu (Columbia, MD, USA). The TGA experiments were conducted under nitrogen atmosphere (30 ml/min) in the temperature range T = 25… 600°C with heating rate 10°C/min.

2.3. Flexural and fracture mechanical behavior

The flexural properties, namely, modulus and strength of the hybrid resins, were determined on rectangular specimens (60 × 8 × 4 mm^3; length × width × thickness) in three point bending at room temperature according to EN63. The span length of the specimens was 50 mm and their loading on a Zwick 1474 (Zwick GmbH, Ulm, Germany) universal testing machine occurred with deformation rate v = 1 mm/min.

The fracture toughness (K_c) and fracture energy (G_c) were measured according to ISO 13586-1 standard. The tests were done on the Zwick 1445 machine at room temperature (*RT*) with a crosshead speed of v = 1 mm/min. The CT specimens (dimension: 35 × 35 × 3 mm^3; length × width × thickness) were notched before loading by sawing. The sawn notch of the CT specimens was sharpened by a razor blade. The razor blade, fixed in a rig, was positioned in the notch root before hitting the fixing rig with a hammer. This 'taping' yielded the desired sharp crack.

2.4. Morphology inspection

To get an insight in the morphology of the hybrid systems the techniques scanning electron and atomic force microscopy (SEM and AFM, respectively) were adapted. The fracture surface of CT specimens has been investigated in SEM using a JSM 540 device of Jeol (Tokyo, Japan). The surface was coated with an Au/Pd alloy prior to SEM inspection using a Balzers SCD 050 (Balzers, Lichtenstein) sputtering apparatus.

AFM scans were taken on polished samples by an AFM device (Veeco/Digital Instruments GmbH, Mannheim, Germany) in tapping mode, and the related height- and phase-contrast images captured. Commercial silicon cantilever (Pointprobe®NCH of Nanosensors, Neuchatel, Switzerland) with a nominal tip radius of less than 10 nm (120 μm cantilever length, 4 μm thickness, 30 μm width and spring constant at 42 Nm^{-1}, Nanosensors, Neuchatel, Switzerland) was employed under its fundamental resonance frequency of about 330 kHz. The scan rates were set at 0.5 Hz for all images.

3. Results and discussion

3.1. Effects of diamines on the BOX polymerization

Figure 3 displays the DSC thermograms of BOX with and without the diamines selected.

It is clearly seen that all amines exhibited the supposed acceleration effect as the peak linked with the polymerization of BOX (T = 253°C) was shifted toward lower temperatures. This is the right place to mention that we do not use the term 'catalytic effect' because the amount of amines is much too high for catalysts. In contrast to the aromatic diamine, in the traces of BOX with DETA and the cycloaliphatic diamine two exothermic peaks could be resolved. The high temperature peak should be assigned to the BOX homopolymerization. The low temperature peak, on the other hand, obviously reflects the reaction between BOX and amine. This finding is in line with that of Agag *et al.* [13]. On the other hand, neither the amine consumption nor the related reaction were studied in detail. It is noteworthy that the low temperature exotherm peaks at lower tempera-

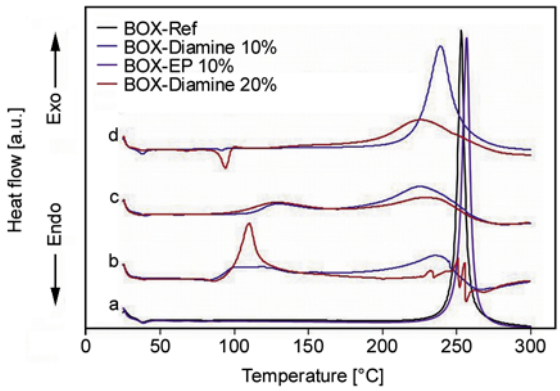

Figure 3. DSC traces showing the thermally-induced polymerization of BOX with and without 10 wt.% EP (a), as well as the effects of aliphatic (b), cycloaliphatic (c) and aromatic diamines (d), added in 10 and 20 wt.%, respectively. Notes: scatter in the DSC traces of BOX/DETA at T > 220°C is due to the decomposition of DETA. BOX combined with EP (without amine hardener) does not affect much the curing

ture for the DETA than for the cycloaliphatic diamine. This suggests differences in the basic character of the diamines which follows the ranking: aromatic < cycloaliphatic < aliphatic. It is also well resolved that with increasing amine content the intensity of the low temperature exotherm increases, whereas the high temperature one decreases. The thermal behavior of the BOX/DDM system differs markedly from BOX/DETA and BOX/cycloaliphatic diamine. In BOX/DDM only one exothermic peak appears. Accordingly, the BOX homopolymerization is superimposed to the oxazine/amine reaction. With increasing DDM content the exothermic peak is shifted toward lower temperatures whereby its intensity is highly reduced. Parallel to that the onset of this peak (i.e. where deviation starts from the base line) was markedly reduced. To sum up the above results one can establish that diamines are suitable accelerators of the BOX polymerization and the acceleration effect strongly depends on both their chemical structure and amount. The DSC traces in Figure 3 substantiate that the starting temperature for BOX curing (second exothermic peak) lies at $T \approx 180$°C. That was the reason to select this temperature along with a long holding time for the final step of the cure cycle given in Figure 2. The large difference in the acceleration of BOX polymerization between DETA and DDM prompted us to select them, and consider their 1/1 mixture, as well, as EP hardeners.

3.2. Thermal and viscoelastic properties of EP/BOX hybrids

Figure 4 shows the DSC traces of the amine-cured EP and EP/BOX hybrids. The T_g steps are well resolved for all systems. As expected, crosslinking

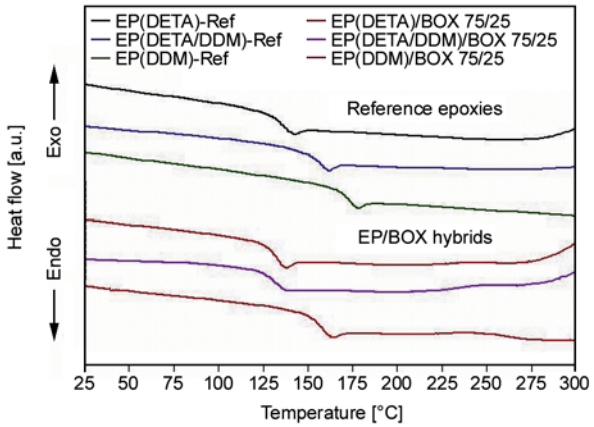

Figure 4. DSC thermograms for the amine-cured EP and EP/BOX hybrids

with DDM yielded the highest, with DETA the lowest T_g, and the T_g of the EP cured with mixed DETA/DDM (1/1) is in between. The EP/DETA starts to decompose at $T > 270$°C based on the exothermic flank in the corresponding curve. Effects of the diamines on the T_g of the EP/BOX (75/25 wt.%) differ from those noticed for the EP reference samples. Though DDM gives the highest T_g, the T_g data are similar for DETA- and DETA/DDM-cured EP/BOX. The presence of BOX did not enhance the T_g, just the opposite tendency happened. This suggests that the EP/diamine ratio was no more stoichiometric due to the reaction between the oxazine and primary amine groups. The shallow exothermic peak at $T \approx 240$°C may hint that the BOX was not fully (co)cured in the related sample. The rise of the DSC trace in exothermic direction at $T > 275$°C reflects the onset of degradation.

Figure 5 compares the DMTA spectra of the amine-cured EP and EP/BOX (75/25 wt.%) hybrids.

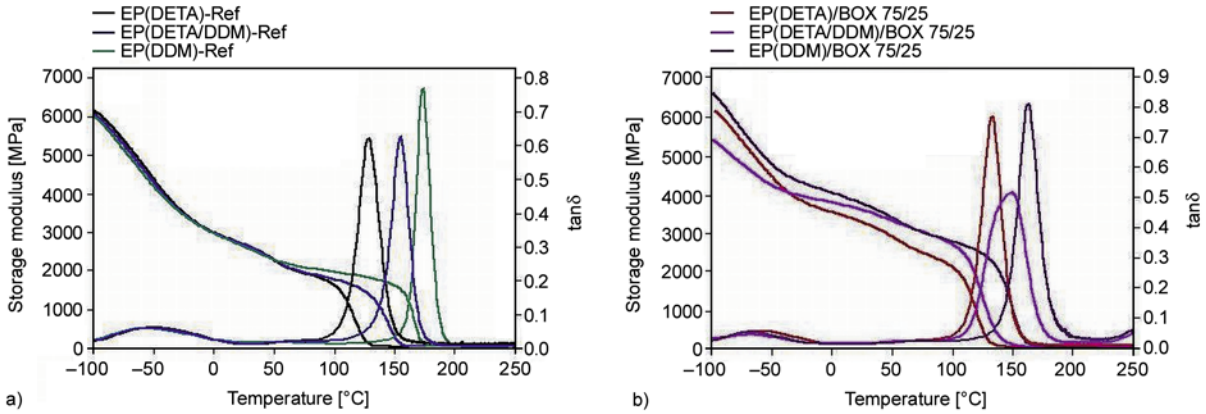

Figure 5. Storage modulus (E') and mechanical loss factor (tanδ) in function of temperature for the amine-cured EPs (a) and EP/BOX hybrids (b)

The E' vs. T traces of the amine-cured EPs split from each other only at $T > 50$°C. As expected, the highest stiffness and T_g were delivered by DDM, followed by DMM/DETA and the lowest one presented the DETA-cured EP. Based on the tanδ vs. T traces the type of the amine did not influence the beta-relaxation ($T \approx -50$°C) by contrast to the alpha-relaxation (T_g). T_g values, read at the peak temperature of the alpha-relaxation, followed the ranking: DETA < DETA/DDM < DDM in concert with the DSC results. The T_g values are summarized in Table 1.

The course of the E' vs. T traces of EP/BOX is not as smooth as found for the reference EPs. On the other hand, comparing the corresponding E' vs. T traces for EP and EP/BOX (75/25 wt.%) in Figure 5a and 5b, respectively, one can recognize that modification with BOX improved the stiffness of the EP. Comparing the tanδ vs. T traces of the EP and EP/BOX (75/25 wt.%) containing the same diamine, two striking features can be observed: i) T_g was reduced by the incorporation of BOX (which is in line with the DSC results (cf. Figure 4 and Table 1), and ii) the tanδ peak of EP/BOX cured with the mixed amines (DETA/DDM) became broader than in the corresponding EP. Stiffness increase parallel with T_g decrease are usually caused by antiplasticizers, which is a known phenomenon also for EPs (e.g. [14–15]). The so-called internal antiplasticization caused by a change of the network structure. This is observed for non-stoichiometric or partially reacted epoxy-amine systems or when using a monoamine as a chain extender [14]. The two former features are present in our case due to the incorporation of BOX: BOX reacts namely with both amine and EP, but was considered as non-reactive additive in our formulations. It was also demonstrated that that antiplasticization affects the beta-relaxation similarly as the reduction of crosslink density, i.e. shifts the related peak toward lower temperature [15]. This can be observed also in our case – cf. beta peak at $T \approx -75$°C in Figure 5b.

The co-curing of EP with BOX is well reflected by the data of the rubber plateau modulus (E'_R). E'_R data were read at $T_g + 30$°C for the EP and EP/BOX hybrids studied and are also listed in Table 1. The E'_R data can be used to estimate the crosslink density according the theory of rubber elasticity (Equation (1)):

$$\nu_c = \frac{E'_R}{3RT} \tag{1}$$

where υ_c is the crosslink density, R is the gas constant, and T is the absolute temperature (i.e. at $T_g + 30$°C).

The crosslink densities are also included in Table 1. The broadening of the tanδ peak for the EP/BOX (75/25 wt.%) can be explained by the difference in the reactivity between the related amines and the oxazine. The amine/oxazine reaction affects later on the EP curing and EP/BOX co-curing, as well.

The DMTA analysis revealed that the modification with BOX enhanced the stiffness (E-modulus), decreased the crosslink density and reduced the T_g. The decreasing crosslink density of the hybrids can be traced to the low crosslinking density of the homopolymerized BOX. Ranking of the neat EPs in respect to the crosslink density (EP(DDM)-Ref > EP(DETA/DDM)-Ref > EP(DETA)-Ref) differs from that of the EP/BOX series (EP(DDM)/BOX ≥ EP(DETA)/BOX > EP(DETA/DDM)/BOX). This is due to the formation of an EP/BOX co-network, which is influenced by chemical reactions among the EP, amine hardener and BOX. This affects the distribution of the possible intra- and intermolecular hydrogen bonds, as well. According to our opinion the structure development in EP/BOX hybrids is mostly controlled by differences in the chemical structure and reactivity of the diamines (DETA, DDM).

Table 1. Thermal and viscoelastic parameters of the resins prepared

System	T_g [°C]		E' [MPa]		ν_c	$T_{2\%}$	Char yield
	DSC	DMTA	RT	$T_g + 30$°C	[mol/dm^3]	[°C]	[wt.%]
EP(DETA)-Ref	135	130	2690	33	3.06	327	9.0
EP(DETA/DDM)-Ref	155	155	2690	41	3.59	338	14.0
EP(DDM)-Ref	173	174	2630	43	3.61	362	17.5
EP(DETA)/BOX (75/25)	132	134	3245	28	2.57	317	14.0
EP(DETA/DDM)/BOX (75/25)	133	151	3560	23	2.03	309	25.0
EP(DDM)/BOX (75/25)	158	164	3720	30	2.58	335	22.3

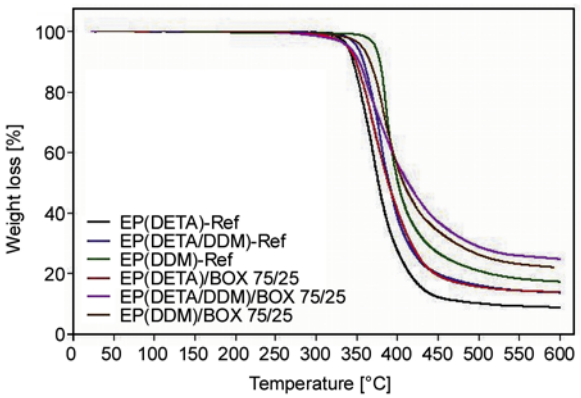

Figure 6. TGA traces registered for the EP and EP/BOX (75/25 wt.%) hybrids

It remains, however, an open issue how the BOX units are incorporated into the EP network, and whether or not BOX is completely cured.

The TGA curves, registered on the EP and EP/BOX systems confirm that BOX incorporation improved the charring, in fact – cf. Figure 6. The temperature values linked with 2 wt.% loss and the char yield at $T = 600°C$ are listed in Table 1, too. TGA traces in Figure 6 demonstrate that curing with DDM results in more temperature resistant EP-based systems than with DETA. A further finding is that the degradation onset was reduced by the BOX present, albeit the amount of the final residue (char) was enhanced. This suggests that the products of the reaction between oxazine and amine are less temperature resistant than those formed via epoxy/amine and epoxy/benzoxazine reactions.

3.3. Static flexural and fracture mechanical properties

The static flexural properties, i.e. *E*-modulus (E_f), strength (σ_f) and displacement at maximum load ($\varepsilon_{f,m}$) are listed in Table 2. One can establish that the *E*-modulus and flexural strength increased, whereas the displacement at maximum load decreased with BOX incorporation. Accordingly, BOX acted as reinforcement in the related EP/BOX hybrids. On the other hand, no clear tendency could be detected for the flexural properties in function of the type of the diamine compounds. The highest E_f and σ_f were found for the mixed amine-cured EP/BOX.

The fracture mechanical data, also listed in Table 2, yielded unexpected results. Modification with BOX slightly reduced both the fracture toughness (K_c) and fracture energy (G_c) compared to those of the reference resins. Moreover, the fracture mechanical

Table 2. Flexural and fracture mechanical data for the EP and EP/BOX hybrids (75/25 wt.%).

Material	Properties				
	Flexure			Fracture mechanics	
	E_f [MPa]	σ_f [MPa]	$\varepsilon_{f,m}$ [%]	K_c [MPa·m$^{1/2}$]	G_c [J·m^2]
EP(DETA)-Ref	2829±73	111.0±9.6	6.85±1.10	0.78±0.03	333±24
EP(DETA/DDM)-Ref	2644±119	98.1±5.7	8.02±2.48	0.74±0.03	308±39
EP(DDM)-Ref	2424±257	121.8±9.2	8.41±0.82	0.80±0.07	362±54
EP(DETA)/BOX (75/25)	3117±228	116.7±25.8	4.39±1.71	0.68±0.07	235±56
EP(DETA/DDM)/BOX (75/25)	3785±473	167.4±26.5	5.88±1.21	0.74±0.10	215±48
EP(DDM)/BOX (75/25)	3250±221	147.6±15.2	6.41±0.38	0.64±0.08	214±42

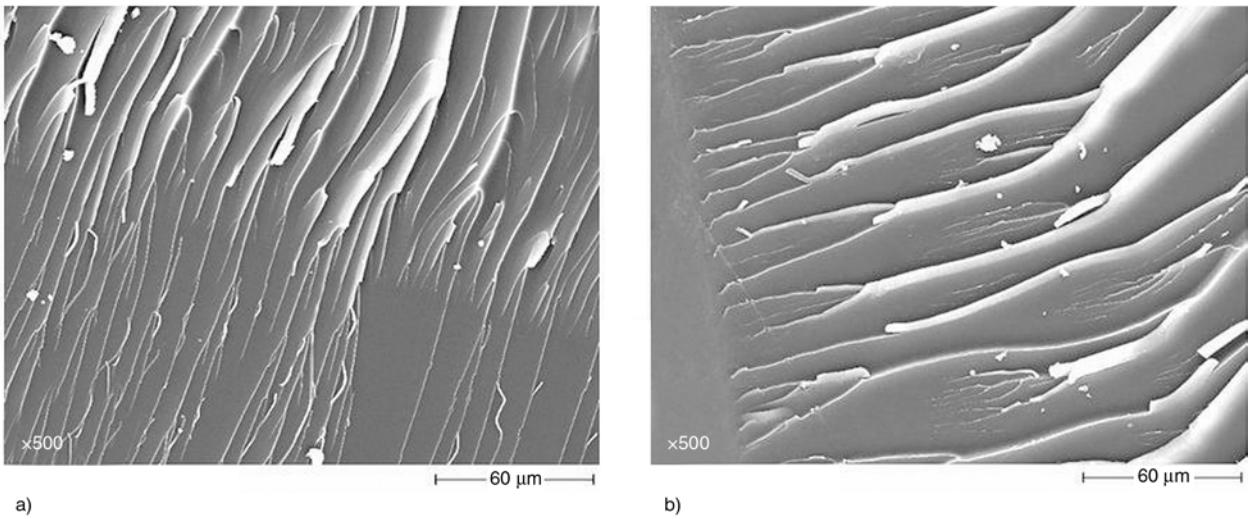

Figure 7. SEM pictures taken of the fracture surface of EP(DETA/DDM) (a) and EP(DETA/DDM)/BOX (75/25 wt.%) (b)

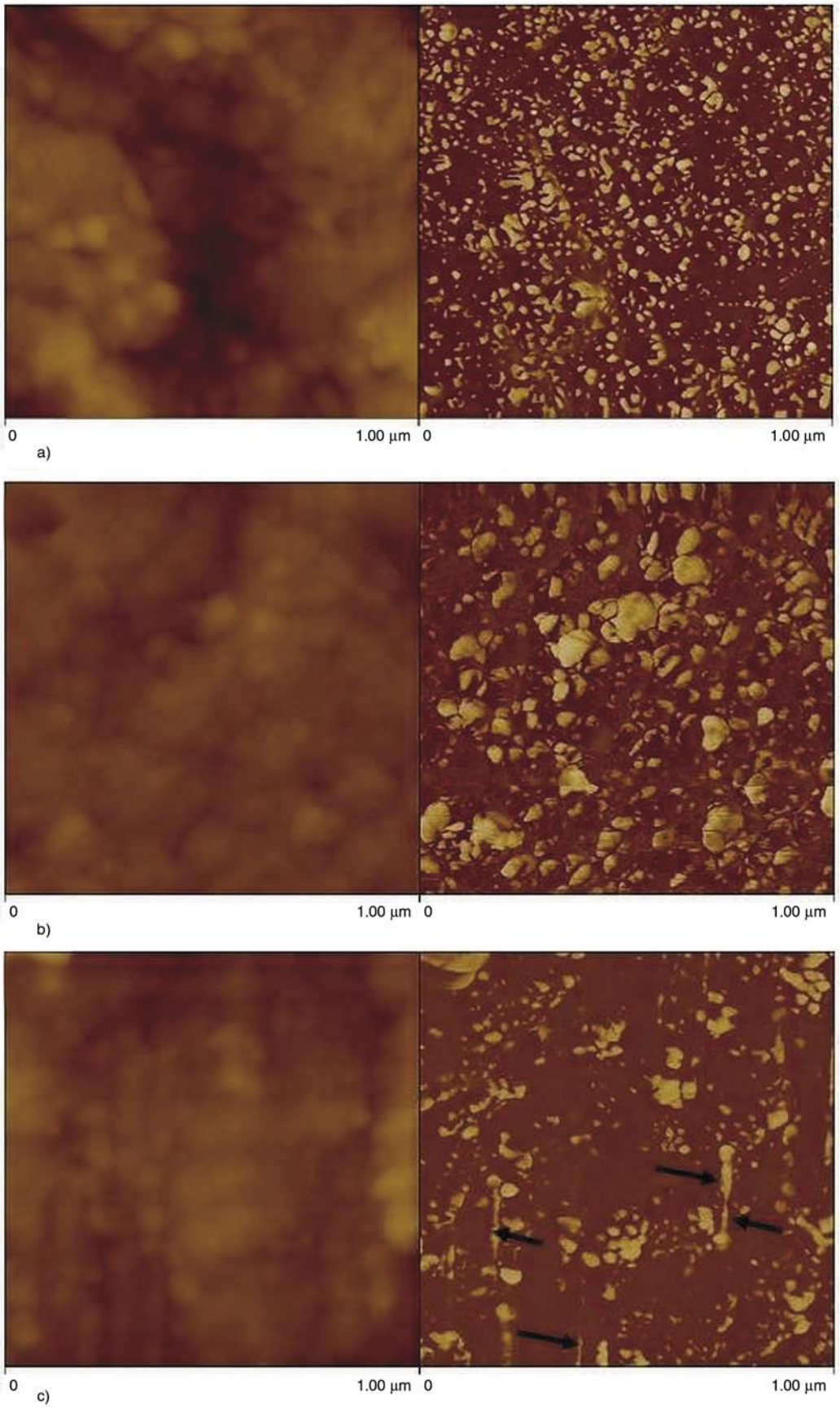

Figure 8. AFM height (left) and phase images (right) on the systems EP(DDM)/BOX = 75/25 wt.% (a), EP(DETA)/BOX = 75/25 wt.% (b) and EP(DETA/DDM)/BOX = 75/25 wt.% (c). Note: some vertically aligned 'tails' in the phase image picture c are related to experimentally-induced artefacts (indicated by arrows).-

response of the systems was practically not influenced by the amine used. Based on the fact that the *E*-modulus and strength of the EP increased by BOX hybridization, one expected an increment in K_c and a reduction in G_c compared to the reference EP resins. This was not the case that should rely on the morphology of the hybrid resins. Nevertheless, the K_c and G_c data of the EP/BOX hybrids are superior to the polymerized neat BOX.

3.4. Morphology

The fracture surfaces of the amine-cured EP and EP/BOX hybrids are very similar to each other. This, suggesting that the fracture mechanical parameters should be similar, as well (which is the case, in fact, as shown by the data in Table 2), is demonstrated on the example of EP(DETA/DDM) and EP(DETA/DDM)/BOX (75/25 wt.%) in Figure 7. The appearance of the fracture surface suggests that BOX is well incorporated in the EP network, and its domain size (in case of eventual phase separation) should lie in submicron range. The AFM work supported this suggestion (see below).

The AFM height and phase images, taken from the polished surfaces of the EP/BOX system hardened by different amines are depicted in Figure 8. The white spots in the AFM phase images represent the homopolymerized BOX. In case of DDM hardener, the thermally homopolymerized BOX is finely and uniformly dispersed in the EP matrix. The size of the polymerized BOX inclusions is in the range of 5–100 nm (main fraction is in the range of 7.5–45 nm). By contrast, the dispersion of the homopolymerized BOX in the DETA-hardened EP is coarse and broad (particle size of 15–150 nm). The change in the BOX dispersion is linked with the phase segregation between EP and BOX, governed by the gelling/crosslinking of EP. The latter is much faster and occurs at lower temperatures with DETA than with DDM hardener. This results in a fine distribution of homolymerized BOX in the EP matrix with DDM and a coarse one with DETA hardening. As, expected, the polymerized BOX appears in a bimodal-like distribution of 7–120 nm particles in the EP(DETA/DDM)/BOX system (cf. Figure 8c).

4. Conclusions

It was established that amine hardeners accelerated the homopolymerization of benzoxazine (BOX). Based on this knowledge an amine-curable bifunctional epoxy resin was modified with BOX at a fix ratio (EP/BOX = 75/25 wt.%) and the basic thermal and mechanical properties of the corresponding hybrid determined. As amine hardeners an aliphatic, an aromatic diamine, and their 1/1 mixture were selected. The properties were collated with those measured on the reference EP. The outcome of this research work can be summarized as follows:

Network structure and morphology

– The amine-hardened EP formed a co-network with the BOX. This contained nanoscaled inclusions of the homopolymerized BOX. The dispersion characteristics of the hompolymerized BOX depended on the amine type. The finest dispersion was found for DDM, whereas a coarse one for DETA hardener. This was traced to the phase segregation process governed by the gelling and crosslinking of the EP with the given diamine.

Thermal properties

– The T_g of the hybrid was lower than the reference EP that was traced to off-stoichiometry caused by the amine/oxazine reaction. The observed internal antiplasticizing effect of BOX in EP/BOX hybrids was traced also to off-stoichiometry, affected by the reaction between BOX and EP, as well. Although the thermal degradation of the hybrid preceded that of the reference EP, incorporation of BOX was associated with a pronounced increase in the char yield.

Mechanical properties

– BOX incorporation enhanced the stiffness (*E*-modulus) and strength based on DMA and flexural tests. This was explained by the nanoscaled homopolymerized BOX, well connected to the EP network. On the other hand, none of the fracture mechanical parameters could be improved by adding BOX.

Acknowledgements

This work was done in the framework of a collaboration project between Germany and South Africa, sponsored by BMBF and NRF, respectively. It was also supported by the Advanced Manufacturing Technology Strategy program of DST (South Africa) and Hungarian Scientific Research Fund OTKA. The authors thank to Dr. P. Tsotra (Huntsman Advanced Materials, Basel, Switzerland) for the BOX delivery.

References

[1] Reghunadhan Nair C. P.: Advances in addition-cure phenolic resins. Progress in Polymer Science, **29**, 401–498 (2004).
DOI: 10.1016/j.progpolymsci.2004.01.004

[2] Yagci Y., Kiskan B., Ghosh N. N.: Recent advancement on polybenzoxazine – A newly developed high performance thermoset. Journal of Polymer Science Part A: Polymer Chemistry, **47**, 5565–5576 (2009).
DOI: 10.1002/pola.23597

[3] Santhosh Kumar K. S., Reghunadhan Nair C. P.: Rapra, Shawbury (2010).

[4] Ishida H., Allen D. J.: Mechanical characterization of copolymers based on benzoxazine and epoxy. Polymer, **37**, 4487–4495 (1996).
DOI: 10.1016/0032-3861(96)00303-5

[5] Endo T., Sudo A.: Development and application of novel ring-opening polymerizations to functional networked polymers. Journal of Polymer Science Part A: Polymer Chemistry, **47**, 4847–4858 (2009).
DOI: 10.1002/pola.23531

[6] Takeichi T., Agag T.: High performance polybenzoxazines as novel thermosets. High Performance Polymers, **18**, 777–797 (2006).
DOI: 10.1177/0954008306068254

[7] Ishida H., Rodriguez Y.: Catalyzing the curing reaction of a new benzoxazine-based phenolic resin. Journal of Applied Polymer Science, **58**, 1751–1760 (1995).
DOI: 10.1002/app.1995.070581013

[8] Rao B. S., Reddy K. R., Pathak S. K., Pasala A. R.: Benzoxazine–epoxy copolymers: Effect of molecular weight and crosslinking on thermal and viscoelastic properties. Polymer International, **54**, 1371–1376 (2005).
DOI: 10.1002/pi.1853

[9] Kimura H., Matsumoto A., Hasegawa K., Ohtsuka K., Fukuda A.: Epoxy resin cured by bisphenol A based benzoxazine. Journal of Applied Polymer Science, **68**, 1903–1910 (1998).
DOI: 10.1002/(SICI)1097-4628(19980620)68:12<1903::AID-APP2>3.0.CO;2-P

[10] Kimura H., Matsumoto A., Ohtsuka K.: New type of phenolic resin: Curing reaction of phenol-novolac based benzoxazine with bisoxazoline or epoxy resin using latent curing agent and the properties of the cured resin. Journal of Applied Polymer Science, **112**, 1762–1770 (2009).
DOI: 10.1002/app.29301

[11] Rao B. S., Pathak S. K.: Thermal and viscoelastic properties of sequentially polymerized networks composed of benzoxazine, epoxy, and phenalkamine curing agents. Journal of Applied Polymer Science, **100**, 3956–3965 (2006).
DOI: 10.1002/app.23008

[12] Lin H. T., Lin C. H., Hu Y. M., Su W. C.: An approach to develop high-T_g epoxy resins for halogen-free copper clad laminates. Polymer, **50**, 5685–5692 (2009).
DOI: 10.1016/j.polymer.2009.09.075

[13] Agag T., Arza C. R., Maurer F. H. J., Ishida H.: Primary amine-functionalized benzoxazine monomers and their use for amide-containing monomeric benzoxazines. Macromolecules, **43**, 2748–2758 (2010).
DOI: 10.1021/ma902556k

[14] Pascault J-P., Sautereau H., Verdu J., Williams R. J. J.: Thermosetting polymers. Marcel Dekker, New York (2002).

[15] Bershtein V. A., Peschanskaya N. N., Halary J. L., Monnerie L.: The sub-T_g relaxations in pure and antiplasticized model epoxy networks as studied by high resolution creep rate spectroscopy. Polymer, **40**, 6687–6698 (1999).
DOI: 10.1016/S0032-3861(98)00873-8